Active Control of Rotating Stall with Inlet Distortion

by

Christiaan Mauritz Van Schalkwyk

BIng (Elektron), Universiteit van Pretoria (1980)
MIng (Elektron), Universiteit van Pretoria (1987)
SM Aeronautics and Astronautics, Massachusetts Institute of Technology 1991

Submitted to the Department of Aeronautics and Astronautics
in partial fulfillment of the requirements for the degree of
Doctor of Philosophy at the
Massachusetts Institute of Technology
June 1996

Signature of Author: _____

Department of Aeronautics and Astronautics, May 15, 1996

Certified by: _____

Professor James D. Paduano, Thesis Supervisor
Department of Aeronautics and Astronautics

Certified by:

Professor Wallace E. Vander Velde
Department of Aeronautics and Astronautics

Certified by: _____

Professor Steven R. Hall
Department of Aeronautics and Astronautics

Certified by: _____

Professor Alan H. Epstein
Department of Aeronautics and Astronautics

Accepted by: _____

Professor Harold Y. Wachman
Chairman, Department Graduate Committee

Active Control of Rotating Stall with Inlet Distortion

by

Christiaan Mauritz Van Schalkwyk

Submitted to the Department of Aeronautics and Astronautics
in partial fulfillment of the requirements for the degree of
Doctor of Philosophy in Aeronautics and Astronautics at the
Massachusetts Institute of Technology

Abstract

This thesis describes the first use of active control to extend the stable operating range of a multi-stage axial compressor in the presence of circumferential inlet total pressure distortion. Three control strategies at different levels of sophistication were examined:

(i) Constant gain control laws, experimentally optimized to obtain the lowest stalling flow coefficients for circumferentially uniform flow, were found to be effective in the presence of distortion. Taking into account the coupling between harmonics (which occurs as a result of distortion) further increased the stable operating range. The range extension was 3% for a 0.8 dynamic head distortion. (ii) A new constant gain control law with a single spatial phase shift was also examined. This stabilized the compression system at lower flow coefficients for distorted flow, increasing the operating range by 3.7%. (iii) A theoretical model of the unsteady flow response of an axial compressor to inlet distortion, developed by Hynes and Greitzer, was used to design linear quadratic Gaussian controllers. These model based controllers achieved range extensions of 1.5% and 1.1% for inlet circumferential distortions of 0.8 and 1.9 dynamic head respectively.

System identification procedures were used to examine the dynamic behavior of the disturbance modes in the compressor. The dynamics of small velocity perturbations, measured here for the first time in nonuniform flow, were accurately predicted by the model, extended to include unsteady viscous effects. Experimentally measured multi-input multi-output transfer functions confirmed the strong coupling between harmonics of small velocity perturbations, also as predicted by the model.

Advisor: Prof. James D. Paduano

Title: Associate Professor of Aeronautics and Astronautics
Massachusetts Institute of Technology

Acknowledgements

Sincere thanks to Johann Ahlers who made all of this possible.

I would like to thank my advisor, Prof. James D. Paduano, for his guidance and many interesting discussions during this work. Professor E.M. Greitzer's interest and discussions were also valuable and helped guiding the research. I would also like to thank Prof. A.H. Epstein for financial support.

Bill Ames, Victor Dubrowski, and Jimmy Letendre did all the modifications on the rig for the distortion generator and made sure that the compressor was always running smoothly. Their assistance and friendliness are appreciated.

The squash players at MIT, Sanjeev Agrawal, Alex Elvin, James Habyarimana, Nergis Mavalvala, Ali Merchant, Jim Taylor, and many others, deserve special thanks for all the fun on the court. In particular, Sanjeev and Alex worked hard at keeping the ball away from me.

The biggest part of the thesis was typed by Loekie Pretorius, with help from Stephan Pretorius. Their support has been invaluable.

Thanks to my Mother and sisters for their continued support.

Many others deserve credit for making life fun at MIT. Sanjeev Agrawal & Bhanu Narasimhan, Roland & Frankie Berndt, Riaan Coetsee, Rich Hanna, Kari Hyytinen & Anne Heiermann, Igo Krebs, Calie Pistorius, Stephan & Loekie Pretorius, Fred & Melanie Rindel, Paul Van Deventer, Marius & Marian Van Der Riet, Marinda Viljoen, Kyle Yang. Their friendship has been invaluable and is appreciated.

Financial support from the U.S. Air Force Office of Scientific Research and U.S. Navy Office of Naval Research is acknowledged.

Contents

List of Figures

List of Tables

Notation

Overbars and Tildes

Overbars denote averaged quantities, spatial or temporal. Tildes are used to indicate the (real or complex) spatial Fourier coefficients of the corresponding variable; see Equation (3.1) p.49.

Subscripts

1	upstream
4	downstream
a	AGV
c	compressor
cn	nth cosine Fourier coefficicient, $n = 1, 2, \ldots$
i	inlet, isentropic, imaginary
m	axial measurement location
n	harmonic number
r	rotor, real
s	stator, sound
s	steady
sn	nth sine Fourier coefficicient, $n = 1, 2, \ldots$
t	total or throttle
w	wheel

Superscripts

$(\cdot)^*$	complex conjugate
$(\cdot)^T$	transpose
$(\cdot)^H$	complex conjugate transpose
1	far upstream (see Figure 3.1 p.51 for station numbers)
2	AGV inlet
3	AGV exit = compressor inlet
4	compressor exit
5	plenum
6	throttle exit

Vector notation

Vectors will be written as a column and will be denoted by bold lowercase characters. The $n \times 1$ vector is thus written as

$$\boldsymbol{x} = \begin{bmatrix} x_1 \\ \vdots \\ x_n \end{bmatrix} \tag{0.1}$$

$$= [x_1, \ldots, x_n]^T. \tag{0.2}$$

Matrix notation

Uppercase letters will be used to denote matrices, the corresponding lowercase letters with subscripts ij will be used to denote the (i, j) entry, so the $m \times n$ matrix is written as

$$A = \begin{bmatrix} a_{11} & \cdots & a_{1n} \\ \vdots & & \vdots \\ a_{m1} & \cdots & a_{mn} \end{bmatrix}. \tag{0.3}$$

Columns of the matrix will be denoted by the vectors $\boldsymbol{a}_1, \ldots, \boldsymbol{a}_n$. The transpose of the matrix will be written as A^T and the complex conjugate (or Hermitian) transpose as A^H.

Diagonal and block-diagonal matrices will be indicated by

$$A = \text{diag}[A_1, A_2, \ldots, A_n] \tag{0.4}$$

where A_i is the ith element on the diagonal.

Symbols

Following is a list of symbols used in the main text. Symbols that are local to the appendices are not listed.

A_{21}	Equation (3.25) p.55
A_{54}	Equation (3.33) p.57
$A_{5\phi}$	Equation (3.39) p.57
$A_{\phi 5}$	Equation (3.44) p.58
b	chord
b_{G}	Equation (3.37) p.57
D_θ	Fourier spatial derivative matrix, Equation (3.6) p.50
$E^{x_{\mathrm{m}}}$	Equation (3.45) p.59
f_ϕ, f_γ	AGV flow coefficient relations, Equation (3.10) p.54
F_ϕ, F_γ	Equations (3.19) and (3.20) p.55
$F(\cdot)$	Fourier convolution matrix, Equation (3.3) p.49 and Appendix A
$G(i\omega)$	compression system transfer function
i	$\sqrt{-1}$
k	controller gain for distributed feedback controller
k_n, k_{nn}	controller gain for nth harmonic
k_{t}	throttle constant
$K(i\omega)$	controller transfer function
l_1, l_4	upstream and downstream duct lengths p.51
$l_{\mathrm{r}}, l_{\mathrm{s}}$	rotor and stator total pressure losses p.63
l_{t}	effective compressor length, Equation (3.36) p.57
p	pressure

Table continues on next page.

$p_{\dot{\phi}}, p_{\dot{\gamma}}$ AGV pressure relations, Equation (3.12) p.54

$P_{\dot{\phi}}, P_{\dot{\gamma}}$ Equations (3.21) and (3.22) p.55

r reaction

$\bar{r}$ mean rotor radius

t time

u velocity

$\boldsymbol{v}_1, \boldsymbol{v}_2, \ldots$ eigenvectors of A corresponding to eigenvalues $\lambda_1, \lambda_2, \ldots$.

V matrix of eigenvectors, Equation (4.4)

x nondimensional axial location

x_{m} nondimensional upstream sensor location (m=measure)

$\delta \boldsymbol{x}$ state vector, Equation (3.42) p.58 and Equation (3.68) p.65

β spatial phase shift of distributed controller

β_n, β_{nn} spatial phase shift for nth harmonic

δ perturbation

γ AGV deflection

$\lambda_1, \lambda_2, \ldots$ eigenvalues of A corresponding to eigenvectors $\boldsymbol{v}_1, \boldsymbol{v}_2, \ldots$.

Λ matrix of eigenvalues, Equation (4.5)

μ fluid inertia, see p.17 for meaning of subscripts

ϕ flow coefficient

ψ compressor inlet-total to exit-static pressure rise

ρ density of air

θ angle around annulus

τ nondimensionalized time

τ_{f} constant, Equation (3.59) p.63

$\tau_{\mathrm{r}}, \tau_{\mathrm{s}}$ time constants for loss dynamics, Equations (3.61) and (3.62) p.63

ω nondimensionalized frequency

ω_{c} cross-over frequency

ω_{r} rotor frequency

Abbreviations

AGV	actuator guide vanes
DF	distributed feedback
DFT	discrete Fourier transform
FIR	finite impulse response
HF	harmonic feedback
HFC	harmonic feedback with cross coupling
IMS	integrated mean slope
CIMS	corrected integrated mean slope
LQG	linear quadratic Gaussian
MIMO	multi-input multi-output
MIT	Massachusetts Institute of Technology
PSD	power density spectrum
SISO	single-input single-output
SM	surge margin
SNR	signal to noise ratio
STD	standard deviation
XHG	extended Hynes-Greitzer model
XHG-Euler	XHG with nonlinear description for upstream flow field

1 Introduction

Compression systems are subject to instabilities that limit the range over which safe operation is possible. As the mass flow through the compressor is decreased, the peak pressure rise across the compressor increases until a point is reached where the flow through the compressor becomes unstable. Loss of stability is undesirable, as the amplitudes of the unstable oscillations are often very large and can cause damage to the engine. In addition, the loss of stability is accompanied by a significant loss in pressure rise.

Two types of instabilities are commonly observed in compression systems. The first, called surge, is a system-type instability that is mainly axisymmetric. Sometimes the surge oscillations are so severe that flow through the compressor reverses. The second, called rotating stall, has the form of a stall cell that rotates around the annulus at a fraction of the rotor speed. Often rotating stall starts out as a small perturbation wave travelling around the annulus, which grows in amplitude, and finally develops into a large amplitude limit cycle, called rotating stall. Due to hysteresis the only way to stop this limit cycle oscillation is to increase the mass flow significantly beyond the point where stall occurred. Whether the compressor surges or stalls depends on the specific system configuration and is determined by the ratio of the plenum compliance to duct inertia as shown by Greitzer [17]. A review of axial compressor stall phenomena is given by Greitzer [16].

Because of these aerodynamic instabilities operation near the unstable region must be avoided. However, this margin of safety forces operation at mass flows that deliver lower than the maximum peak pressure rise. The surge margin (SM) adopted by Aerospace

Recommended Practice committee [42] is defined by

$$\mathrm{SM} = (R_s - R_0)/R_0 \tag{1.1}$$

where R_s is the surge pressure ratio and R_0 is the operating pressure ratio. A typical value of SM is in the range 10 – 20%, and 30 – 50% of this number is accounted for by nonuniform inlet conditions [50] which we discuss next.

If the flow through the compressor is nonuniform the pressure rise across the compressor decreases. In addition, the compression system goes unstable at higher mass flows. This nonuniform flow is also called distortion.

There are several causes of distortion. During takeoff the flow enters the inlet at an angle, resulting in nonuniform total pressure around the annulus. If an aircraft is flying at high angles-of-attack the flow can separate from the inlet lip and this, too, will create nonuniform flow through the compressor. Nonuniform temperature profiles can exist in the inlet ducts in very short takeoff and landing aircraft when hot exhaust gases are ingested. Whatever the cause, distortion adversely affects compressor operation.

The distorted flow can be circumferentially or radially nonuniform. Reid [41] found that circumferentially nonuniform flow is more severe so we will concentrate on it. Reid found that if the angular width of low inlet total pressure is increased from zero there is an initial steep drop in the exit static pressure of the compressor until an angle is reached beyond which there is little change in the exit static pressure. This angle is called the critical sector angle and is shown in the graph at the top of Figure 1.1, taken from Reid [41]. Reid also found that if the distorted region is split into several smaller regions distributed around the annulus but the cumulative width is kept constant, the biggest loss in pressure rise occurs when there is only one continuous distorted region. This is shown in the graph at the bottom of Figure 1.1.

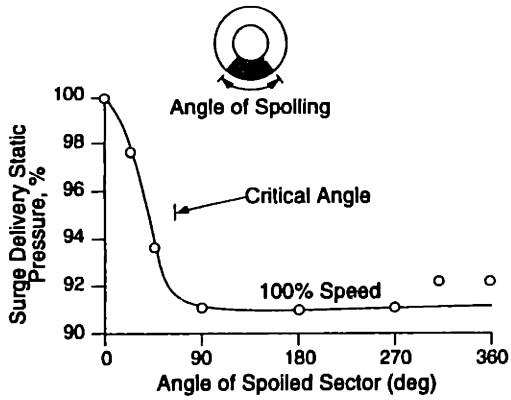

(a) Effect of Spoiled Sector Width

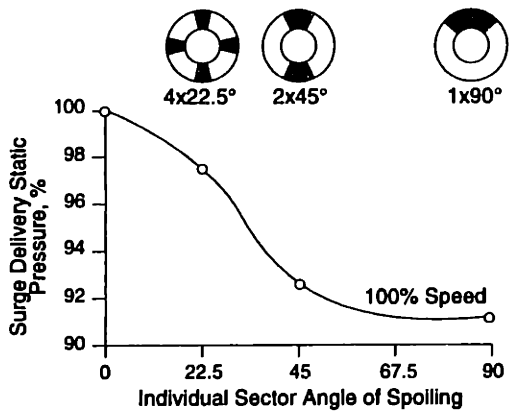

(b) Contiguous Spoiled Sector Width is Important

Figure 1.1: Effect of distortion on exit static pressure. Taken from Reid [41].

The loss in pressure rise can be explained by a very simple model. Assume that two halves of the compressor annulus are operating at two different pressures as shown in Figure 1.2. In this figure we see that the mean peak total to static pressure rise ψ_{TS} is lower than that of the compressor operating at the same mean mass flow. This model, proposed by Mazzawy [32], is often called the parallel compressor model. Although the parallel compressor model explains the loss in peak pressure rise it does not capture all the dynamics in a compression system. Hynes and Greitzer [22] realized that to take distortion into account the nonuniformity must enter the dynamics in a nonlinear way and developed a

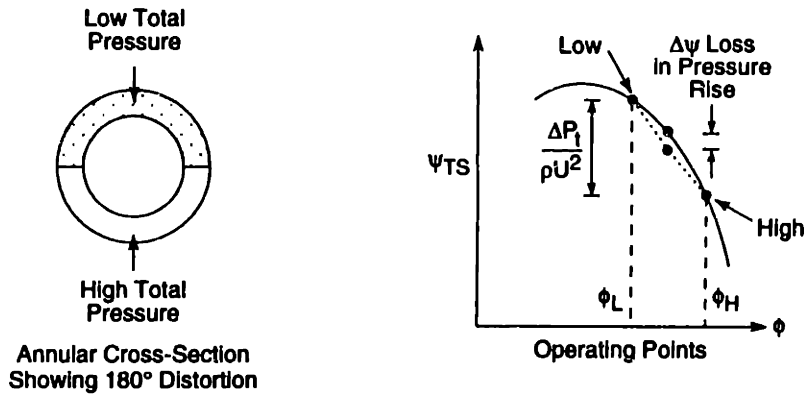

Figure 1.2: Parallel Compressor Model. Taken from [29].

model to account for distorted flow. Studies by Hynes and Greitzer [22] found that the model correctly predicts the trends that were observed by Reid [41]. Hynes and Greitzer [22] and Chue et al. [5] also found that the mass flow at which the circumferentially integrated mean slope (IMS) of the compressor characteristic is equal to zero approximately corresponds to the point where the compression system looses stability. The model by Hynes and Greitzer is an extension to the distorted flow case of an earlier model by Moore and Greitzer [34]. A review of different models for the analysis of compression system instabilities is given by Longley [28].

The model by Moore and Greitzer [34] predicts that a small amplitude perturbation should propagate around the annulus prior to stall. McDougall [33] observed these waves in a low speed single-stage axial compressor, and Garnier [12] identified them in both a single- and a three-stage compressor. Experiments by Day [7] showed that some compressors do not exhibit travelling waves prior to stall; instead a short length scale perturbation rotated around the annulus at approximately 70% of the rotor speed. The reason for this behavior is not known and is currently being researched. Day and Freeman [8] and Tryfonidis et al. [46] observed that travelling waves are also present in high speed compressor prior to stall. These are encouraging results as it allows experiments to be conducted on low speed

compressors.

The Hynes-Greitzer model predicts that, in the presence of distortion, small amplitude waves will travel around the annulus. But, unlike uniform flow, the waves are not purely sinusoidal but change shape as they propagate around the annulus. Longley [25] performed distorted flow experiments and observed the predicted circumferential variation in magnitude of the propagating disturbances. He also derived an improved stability criterion, called the corrected integrated mean slope (CIMS) criterion, and showed that the ratio of the plenum compliance to duct inertia derived by Greitzer [17] determines the applicability of the CIMS. Longley also found that the pressure rise predicted by the model is lower than the experimentally observed pressure rise, and attributed the discrepancy to the large inter-blade row gaps and sensitivity to inlet swirl of the experimental compressor. A method to determine the rotor fluid inertia, an important parameter in the model, from steady state velocity profiles was also given by Longley [25].

To reduce the detrimental effect of distortion Schulmeyer [43] conducted distorted flow experiments on a low speed single stage compressor and showed that through static restaggering of inlet guide vanes the nonuniformity in the velocity could be decreased by 50% and the compressor pressure rise could be increased by 5.3%. However, the stalling mass flow remained unchanged.

Epstein et al. [10] suggested that active control could be used to increase the stable operating range of compression systems. Shortly after this researchers gave experimental evidence that proved the viability of the idea by applying active control to surge. We refer to the survey paper by Greitzer et al. [18] for a discussion of various experiments and concentrate here only on the control of rotating stall. Working on a low speed multi-stage compressor Day [6] showed that control scheduling could be used to increase the stable operating range. By sensing velocity perturbations with an array of hot-wires, jets were

turned on to blow in the tip region for a predetermined time once a stall cell was detected, lowering the stall point by 6%.

The first active control of rotating stall was done by Paduano [37] and Paduano et al. [38] on a low speed single stage axial compressor. By taking into account that different modes of a compression system go unstable independently and one after the other as mass flow decreases, controllers were found, one at a time, to stabilize the modes as they went unstable. With this approach the stable operating range was increased by 21%. The same approach was used by Haynes [20] and Haynes et al. [21] on a low-speed three-stage axial compressor and increased the stable operating range by 7.8%. In addition, Haynes [21] showed that unsteady viscous effects could be modelled with a simple first order lag model and identified the associated time constant from experimental data. In both cases flow perturbations were sensed with a set of hot-wires and movable inlet guide vanes were used for actuation.

By using aeromechanical feedback Gysling [19] showed that is was possible to lower the stalling flow coefficient of a single stage low speed axial compressor by 10%. Gysling also observed acoustic modes in the compression system and showed that these modes can lead to instability.

All the control experiments discussed above were done for circumferentially uniform flow. The work presented here extends active control of rotating stall for the first time to the nonuniform flow case. In addition, the dynamics of small perturbations in the presence of large distortions have never been measured before and the predictive capabilities of the Hynes-Greitzer model have not been established. Thus, the objective of this research is to show that active control can be used to increase the stable operating range in the presence of large distortions. In addition, we would like to determine the predictive capability of the model and analyze the effects of distortion on the stability of an experimental compression

system. We would like to give answers to the following research questions. Does the linearized model predict the dynamics of small perturbations? Is the model accurate enough for the design of modern controllers? Are controllers designed for circumferentially uniform flow effective in the presence of distortion? If not, can we find other controllers that will stabilize the system?

The thesis is structured as follows. In Chapter 2 we discuss the MIT three-stage compressor and experimental procedures. The modelling assumptions are stated in Chapter 3, and the basic Hynes-Greitzer model is presented in a state-space description. The model is then extended to include the effects of unsteady viscous effects. Open loop experimental results are presented in Chapter 4. Active control of rotating stall is discussed in Chapter 5. A summary and suggestions for future research are given in Chapter 6.

---

2 Experimental Compression System

All the experiments were conducted on a low speed three-stage compressor. In this chapter we describe the compressor, distortion generator, instrumentation, and experimental procedures.

2.1 The MIT Three-Stage Compressor

The experiments were conducted on a low-speed three-stage research compressor originally designed by Pratt and Whitney. The compressor has been used in the past for various studies by Garnier who studied the behavior of small perturbations during stall inception, and Haynes, who modified the compressor for active control by including actuator guide vanes (AGVs) directly upstream of the compressor. Haynes gives a detailed description of the design of the AGVs and instrumentation.

To study the effects of inlet total pressure distortion the rig was modified by increasing the inlet duct length so that a distortion generating screen could be installed far enough upstream of the compressor to decouple the two components. Flow field perturbations induced by the compressor decay exponentially as $e^{-n|x|}$. The upstream ducts were thus lengthened to 2.5 mean radii to decrease the interaction between the distortion screen and compressor. This suggestion is due to Longley [27]. Separating the screen and compressor by a large distance is not a limitation of the theory but did simplify the experimental procedure because the stagnation pressure distortion, which is the input to the flow field computation, does not depend on compressor behavior. Section 2.2.

To facilitate steady state measurements around the annulus the distortion screen was

Table 2.1: MIT Three-Stage Axial Compressor Design Parameters

Tip Diameter (mm.)	610.0
Hub-to-Tip Ratio	0.88
Design Average Reaction	0.75
Design Flow Coefficient	0.59
Pressure Rise Coefficient (design)	2.03
Efficiency (design)	84.3%
Stalling Flow Coefficient	0.460

mounted on a rotating ring driven by a stepper motor. This allows generation of measurements around the annulus at any number of points using fixed instrumentation by rotating the screen to the desired location. The maximum speed at which the screen can be rotated is 20 rpm. A mounting arrangement was also provided to include a second stationary screen directly upstream of the first screen (see Figure 2.2). With the rotating and stationary screen it is possible to create distortions of varying length. A schematic layout of the complete system is shown in Figure 2.1, and Figure 2.2 shows a part of the upstream duct and distortion generator. Tables 2.1 and 2.2 list the compressor design and geometric parameters. See also Table 3.2 on page 66.

Table 2.2: MIT Three-Stage Axial Compressor Parameters.

	No. of Blades	Chord (mm)	Camber (degrees)	Stagger (degrees)	Tip Clearance (mm)	Leading Edge Blade Angle (degrees)	Trailing Edge Blade Angle (degrees)
IGV	125	20.1	11.0	8.1		0.0	10.0
IGV-AGV Gap		6.0					
AGVs	12	81.2	0.0	8.1		8.1	8.1
AGV-R1 Gap		13.0					
Rotor 1	54	45.2	17.0	42.8	0.97	50.0	41.0
R1-S1 Gap		20.0					
Stator 1	85	31.4	27.0	11.0	0.81	18.0	-1.0
S1-R2 Gap		20.0					
Rotor 2	55	44.8	18.0	43.5	0.94	54.5	36.5
R2-S2 Gap		20.0					
Stator 2	88	31.3	25.0	12.0	0.94	27.5	2.5
S2-R3 Gap		20.0					
Rotor 3	49	50.7	20.0	44.6	0.89	58.0	38.0
R3-S3 Gap		18.0					
Stator 3	90	31.4	53.0	5.5	0.86	36.5	-17.0

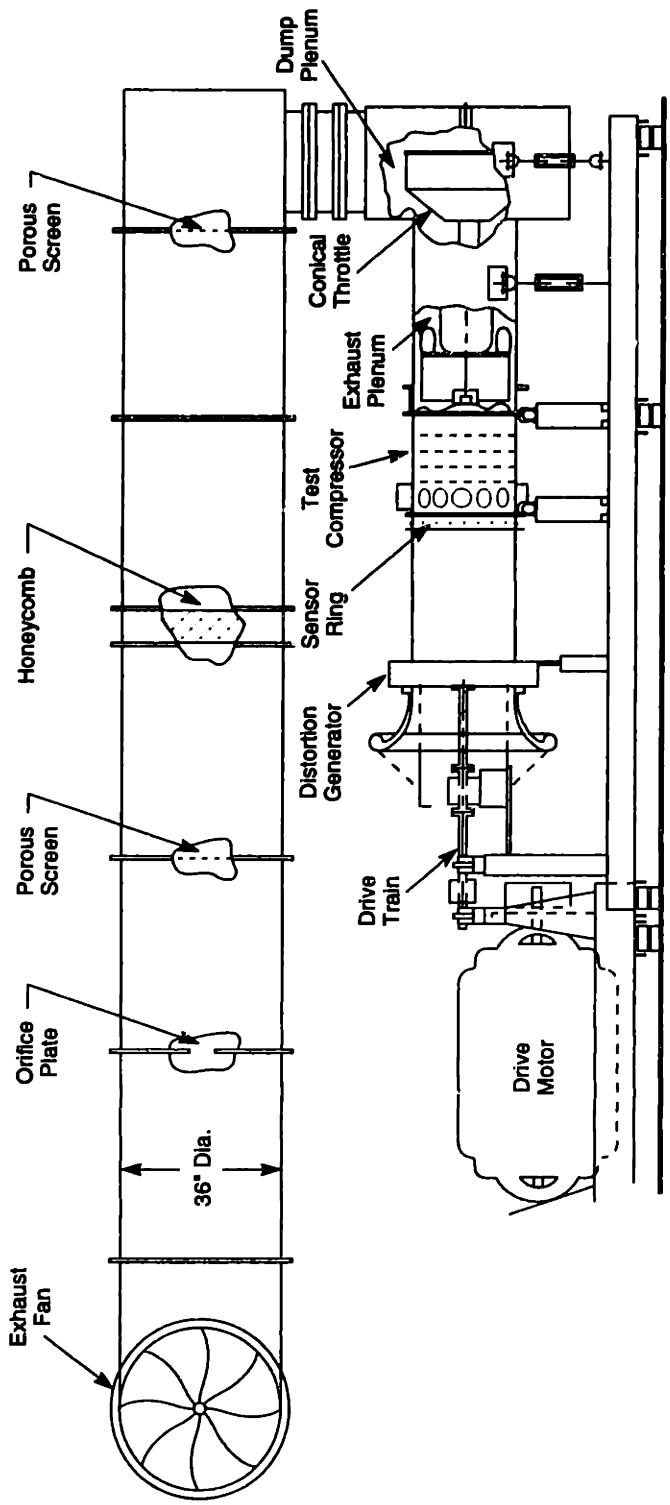

Figure 2.1: Schematic of Three Stage Compressor.

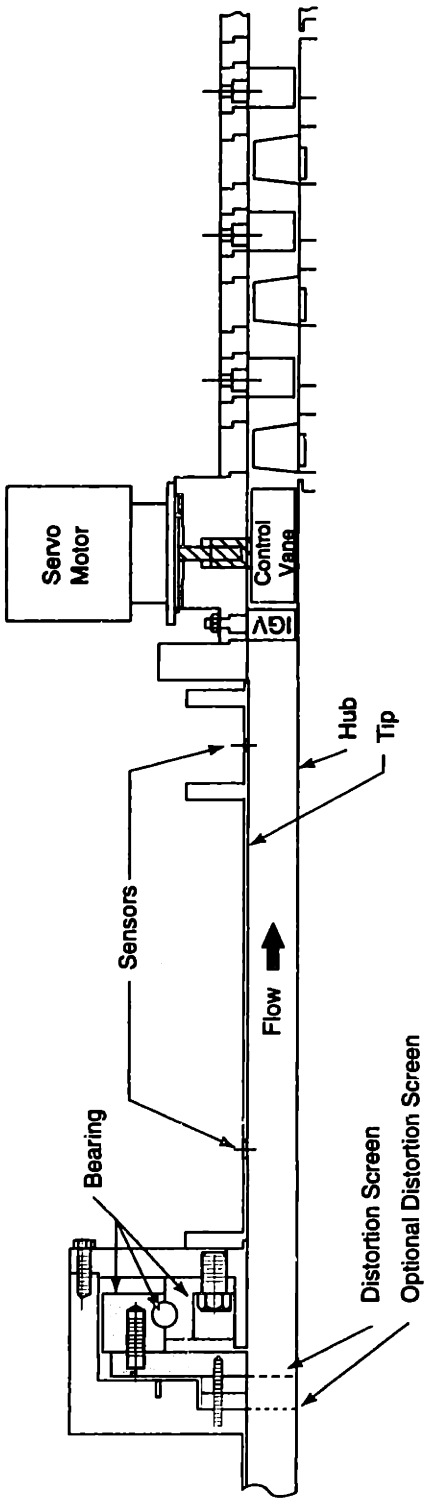

Figure 2.2: Distortion Generator. The shaded parts and distortion screen can be rotated.

2.2 Distortion Generator

Two factors determined the choice of the distortion screens used in the experiments. First, the magnitude of the distortion had to be large enough to introduce strong coupling between different spatial harmonics of perturbations, so that the dynamic behavior with distortion differed significantly from the undistorted case. The basic Hynes-Greitzer model (discussed in Section 3.3) was used to determine the transfer functions between the different harmonics, and distortion magnitudes were chosen so that the magnitudes of the coupling transfer functions between the first and second harmonics were the same order as that of the first harmonic transfer function. (In the absence of distortion the coupling between the first and second harmonic is zero.)

Modal analysis of the linearized dynamics showed that a distortion extent (the part of the annulus that is blocked by the screen, see Figure 2.3) of 120 - 240° has strong first, second and third harmonics, satisfying the coupling requirement. It will be shown that an extent of approximately 120° is a worst case distortion (defined in Section 3.7). Examples of the harmonic content is given in Section 3.6. Distortion magnitude and extent are defined in Figure 2.3.

Second, the distortion should be large enough to give measurable changes in the stalling flow coefficient and peak pressure rise. The measured change in stalling flow coefficient turned out to be small for distortions up to about one dynamic head, (defined below) even though there is strong coupling present between the harmonics. It was thus decided to carry out experiments at two different distortion magnitudes; one of roughly 0.8 dynamic head, that is,

$$d_{c_x} = \frac{\Delta p_t}{\frac{1}{2}\rho \bar{c}_x^2}$$

$$= 0.8, \tag{2.1}$$

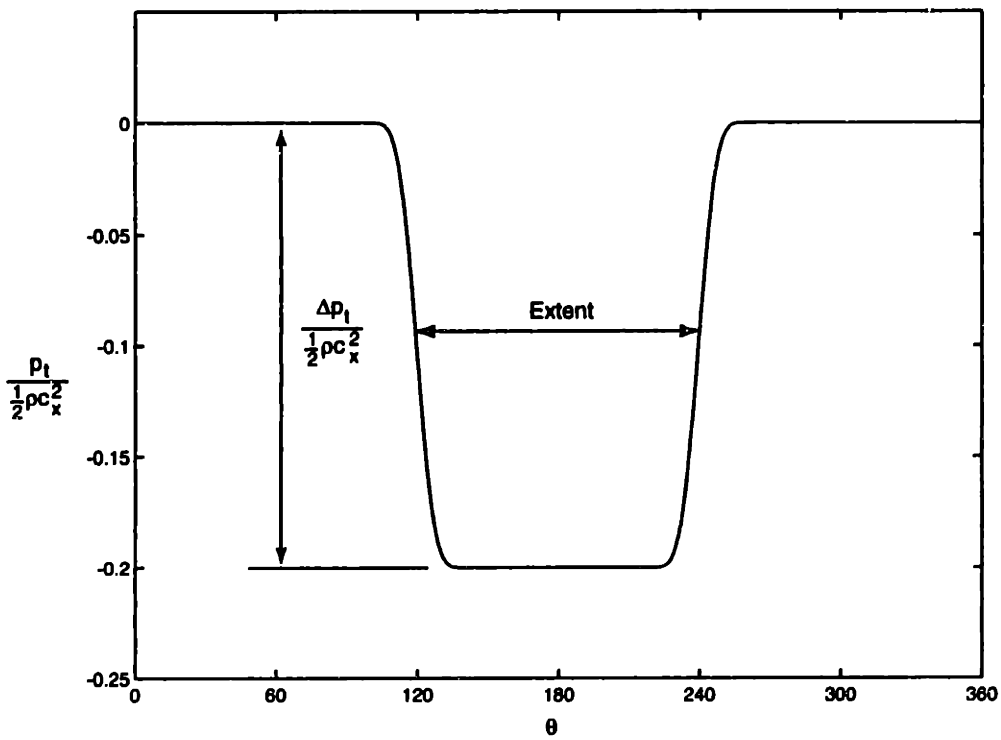

Figure 2.3: Distortion magnitude and extent.

where $\bar{c}_x$ is the mean axial velocity, Δp_t is the drop in total pressure across the screen, and ρ the density of air. The second distortion screen had a magnitude of 1.9 dynamic head. In both cases the distortion extent was 120°. Square-shaped distortions were used as this is a standard used by engine manufacturers. The screens were designed using the formulations given by Bruce [3] and Koo and James [24].

In the following pressures will be nondimensionalized by ρu_w^2 where u_w is the mean wheel speed, see Section 3.3.1. The distortion magnitude defined above has been nondimensionalized by the inlet dynamic head. The relation between distortion magnitudes is

$$d_{c_x} = \frac{2d}{\phi^2} \tag{2.2}$$

where $d = \frac{\Delta p_t}{\rho u_w^2}$ is the distortion magnitude in dynamic head based on wheel speed, and $\phi = c_x/u_w$ is the flow coefficient.

A parameter that is often used to assess the severity of inlet distortion is the DC(60) descriptor (see Williams [49]) defined by

$$\mathrm{DC}(60) = \frac{\bar{p}_t|_{360°} - \bar{p}_t|_{\text{worst } 60°}}{\frac{1}{2}\rho\bar{c}_x^2}. \tag{2.3}$$

In an idealized case where the static pressure is uniform, DC(60)=1 corresponds to zero-velocity flow in a 60° sector of the annulus. This is considered very poor inlet aerodynamics [49]. Experiments by Aulehla and Schmitz [2] on the Tornado showed that $0.15 \leq \mathrm{DC}(60) \leq 0.55$ as the angle of attack is varied over the range 3° to 35° degrees.

At the respective stalling flow coefficients, the 0.8 and 1.9 dynamic head distortions correspond to DC(60)=0.53 and DC(60)=1.31 respectively. Thus, the intensities of the two distortions used in the experiments represent typical and very poor inlet conditions.

2.3 Instrumentation

The layout of most of the instrumentation is shown in Figure 2.4. Steady state static pressures were measured with 8 upstream and 8 downstream wall taps on the outer casing of the compressor. Total-static Pitot probes were also mounted at 8 equally spaced locations around the annulus upstream of the AGVs, at midspan these were used to determine the compressor pressure rise and calibrate the hot-wires. The total-static Pitot probes were mounted 5° degrees away circumferentially from 8 of the hot-wires to ensure that they did not interfere with the flow at the hot-wire tips.

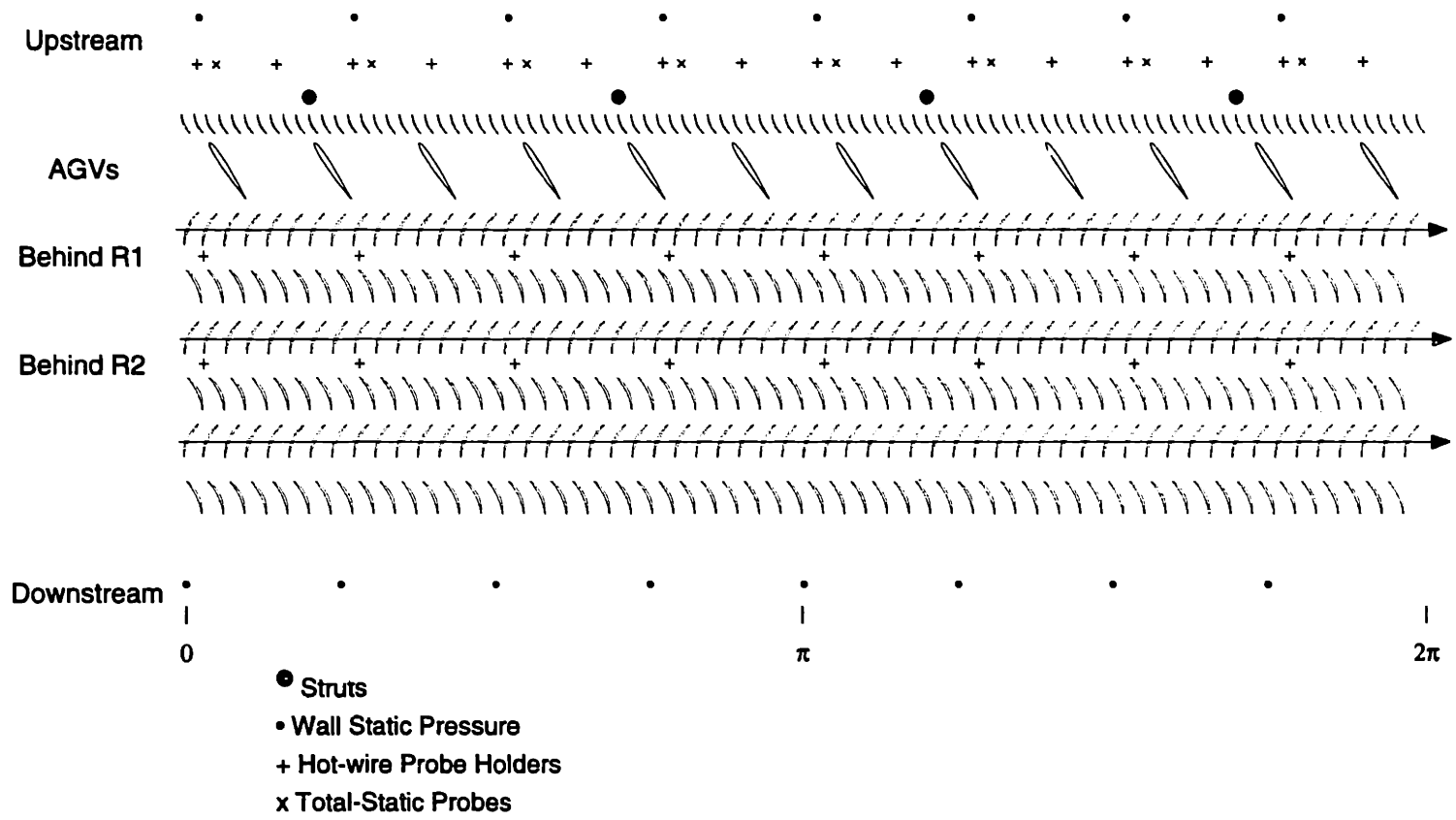

Figure 2.4: Sensor Locations.

Two total-static Pitot probes were mounted downstream of the distortion screen (not visible in Figure 2.4). All the pressure probes were connected to a 48-channel Scanivalve that was controlled by a VAXstation.

Mass flow was measured by an orifice plate far downstream of the throttle (see Figure 2.1). The pressure drop across the orifice plate was measured by an MKS Baratron. The standard deviation of the flow coefficient measurements reported here is less than 0.08%.

Rotor rotation speed was measured with a magnetic pick-up and 60 tooth gear mounted on the drive shaft.

Flow velocities were measured at midspan upstream of the AGVs with 16 equally spaced Dantec 55-P11 hot-wires connected to Dantec 56C17 bridges and CTA 56C01 units. The hot-wires were calibrated before each experiment over the range 6 m/s to 60 m/s (equivalent flow coefficient: 0.08 – 0.8); the calibration procedure is discussed in Section 2.4.1. The hot-wire signals were filtered with fourth order Bessel filters before they were sampled at 500 Hz. The filter cut-off frequency was set to 200 Hz. This cut-off frequency was low enough to give approximately 80 dB attenuation at the rotor blade passing frequency. Analogic HS DAS-16 16-bit A/D converters with AMUX-64-X 64 channel multiplexer were used to discretize the hot-wire signals. The resolution of the A/D was better than 0.01 m/s.

The 12 AGV servo motors were controlled by DMC 430 servo motion controllers. These controllers ran at 2 kHz sampling rate asynchronously from the main control loop. AGV deflections were measured by 4096 pulse per revolution incremental shaft encoders.

2.4 Experimental Procedures

In this section we outline the hot-wire calibration and measurement of the stalling flow coefficient procedures.

2.4.1 Hot-wire Calibration

A new hot-wire calibration procedure was developed to deal with the circumferentially nonuniform flow around the annulus. Eight total-static Pitot probes were used to measure the velocities around the annulus. There are large gradients in the steady flow profile at the edges of the distorted region and it was necessary to include the 5° separation between the hot-wires and total-static probes in the calibration procedure.

The calibration procedure was basically to measure the flow velocity with the total-static probes and then rotate the screen so that the measured velocities are aligned with one set of eight hot-wires. The actual procedure used is more involved and is explained with the aid of Figure 2.5 and the steps below. In the figure we assume the first hot-wire is at 0° and the first total-static probe at 5°. Recall that the hot-wires are separated by 22.5° so the angle between a total-static probe and the next hot-wire is 17.5°.

1. Select a mass flow and execute the following four steps.

   (a) Measure the velocities with the 8 total-static probes. The measured velocities are indicated by circles in the graph at the top of Figure 2.5.

   (b) Rotate the screen through 5° and measure all the hot-wire voltages. The voltages of the hot-wires at $0, 45°, \ldots$ correspond to the velocities obtained from the previous step. This is shown in the second graph from the top in the figure.

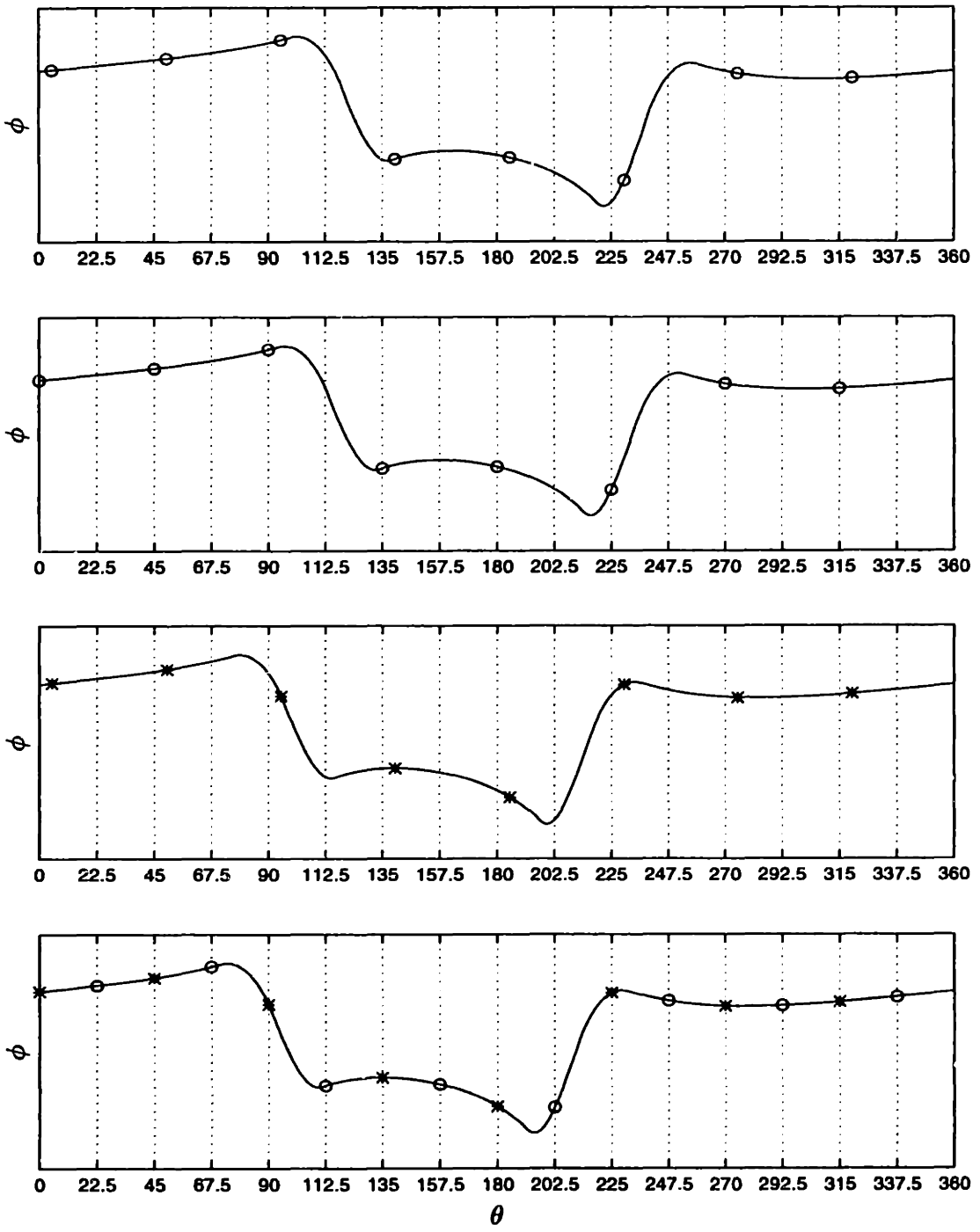

Figure 2.5: Hot-wire calibration. The circles and stars are velocities measured by total-static probes during various calibration steps — see the discussion. The grid lines are aligned with the hot-wires.

(c) Rotate the screen through 17.5° and measure the velocities with the total-static probes. These velocities correspond to the hot-wire voltages at $22.5, 67.5°, \ldots$ in the previous step. These velocities are indicated by stars in the third graph of the figure.

(d) Rotate the screen through 5° and measure all the hot-wire voltages. The voltages of the hot-wires at $0, 45°, \ldots$ correspond to the velocities obtained from the previous step — these velocities are indicated by stars in the bottom graph in the figure. In addition, the velocities measured in step 1(a) are now aligned with the hot-wires at $22.5, 67.5°, \ldots$ and is indicated by the circles in the graph at the bottom of the figure.

Steps 1(a)–1(d) give two calibration points for each hot-wire.

2. Steps 1(a)–1(d) are repeated three more times at 90° intervals, giving a total of eight calibration points for each hot-wire. This step uses the fact that the flow is nonuniform around the annulus and, instead of changing the mass flow, we move to a different point on the profile to get a different velocity.

3. Steps 1 and 2 above are repeated at two more flow coefficients to give a total of 24 velocities for each hot-wire. The three different flow coefficients are chosen so that the absolute minimum to absolute maximum velocity ranges from approximately 6 m/s to 60 m/s. This range covered all the velocities that were encountered during experiments. King's law [14] was used to determine a relation between the hot-wire voltages and corresponding velocities.

2.4.2 Stalling Flow Coefficient Measurement

It was found that the stall point was sensitive to the rate at which the throttle was closed. It was thus necessary to develop a procedure by which the stall point could be determined in a consistent way.

With a rough estimate of the stalling flow coefficient available, the throttle was closed slowly until the mean flow was about 3% above the stall point. From this point on the throttle was closed at the minimum possible rate until the expected stall point was reached — this typically took about two minutes. The throttle was then stopped. The system had to remain stable for at least two minutes at this flow coefficient before it was accepted as the possible minimum point. If the compressor was still stable after two minutes, the throttle was again closed at minimum rate until the flow coefficient was reduced by approximately 0.2%. Again the system had to remain stable for at least two minutes at this flow coefficient. This last step was repeated until a stall point was reached. After a stall the throttle was opened until the compressor returned to unstalled operation and then the procedure was repeated from the beginning. If the same flow coefficient was reached three times it was accepted as the stall point for the particular distortion/controller configuration. In most cases experiments were repeated on different days and the repeatability of the stalling flow coefficients was better than 0.2%.

---

3 Compression System Model

In this chapter we develop a complete model for a compressor operating in the presence of an inlet circumferential total pressure distortion. The goal is to obtain a linearized state space description of the behavior of small perturbations about a circumferentially nonuniform steady flow. We start by stating the ideas that underlie the model. Most variables are periodic and it is useful to express them as Fourier series. Manipulating Fourier series coefficients is convenient if we vectorize the coefficients; the mathematical tools for doing so are given in Section 3.2. Derivation of the linearized dynamics is done in two steps. In the first we determine a steady operating point (mean mass flow or throttle setting) by solving one or more sets of nonlinear partial differential equations. We then linearize the nonlinear partial differential equations about the operating point. These processes are described, as is the extension of the basic analysis to include a simple model of unsteady blade row response. The model is then used to compare uniform and nonuniform flow mode shapes, and explain the control theoretic difference between uniform and distorted flow.

3.1 Assumptions

In this section we summarize the relevant modelling assumptions. Detailed discussion is given by Haynes [20].

The flow is incompressible. In the experiment mean blade Mach number was 0.2 and the modal wave Mach number 0.1.

The flow is two dimensional so that radially averaged description is used. Haynes showed that this was a good approximation for high hub-to-tip ratio compressors. The

hub-to-tip ratio of the compressor used is 0.88.

Viscous effects are negligible outside the blade rows. This assumption is valid if inertial effects are much larger than viscous effects. In the experiment the Reynolds number for the nth harmonic was on the order of $6 \cdot 10^5/n$ so that this assumption is justified.

The compressor can be modelled as a semi-actuator disk. The compressor is the most complex component in the system. This assumption allows us to describe the pressure rise across the compressor in a simple way without describing the detail of the flow in the individual blade rows. The details of the assumption will be discussed when we present expressions for the pressure rise across the compressor.

It is important to note that two assumptions used in previous models for the control of rotating stall have not been included. The first is the assumption that the steady flow is circumferentially uniform. We are specifically interested here in the behavior of the compressor in the presence of circumferentially nonuniform steady flow. The second assumption that has been dropped is the unimportance of overall system (surge) dynamics. When the steady flow is circumferentially uniform and the velocity perturbations are small there is no coupling between the surge and rotating stall modes so that the surge dynamics can be ignored. When the steady flow is circumferentially nonuniform, however, strong coupling can exist between the surge-like and rotating stall modes. It is necessary to include a description of the overall compression system as well.

3.2 Spatial Fourier Series

Most variables in the model will be functions of θ and it is convenient to express them as Fourier series, that is, any function $f(\theta,\tau)$ will be written as

$$f(\theta,\tau) = \widetilde{f}_0(\tau) + \sum_{n>0}(\widetilde{f}_{cn}(\tau)\cos(n\theta) + \widetilde{f}_{sn}(\tau)\sin(n\theta)). \tag{3.1}$$

The function $\widetilde{f}_0(\tau)$ will be referred to as the zeroth harmonic and will always be included in the expansion. Harmonics one, two, ... will be referred to as higher harmonics. Note that we allow for time varying Fourier coefficients.

The development of the model is simplified considerably if we use vectors to represent Fourier series coefficients. To do so, we stack the Fourier coefficients in a vector $\widetilde{\boldsymbol{f}}$ as follows

$$\widetilde{\boldsymbol{f}} = [\widetilde{f}_0,\ \widetilde{f}_{c1},\widetilde{f}_{s1},\ \widetilde{f}_{c2},\widetilde{f}_{s2},\ \ldots,\widetilde{f}_{cn},\widetilde{f}_{sn}]^T. \tag{3.2}$$

Multiplication of Fourier series with known coefficients by Fourier series with unknown coefficients occurs frequently. Let $g(\theta)$ be a known Fourier series; we would like to write the coefficient vector $\widetilde{\boldsymbol{p}}$ of the product $p(\theta) = g(\theta)f(\theta)$ in terms of the coefficient vector $\widetilde{\boldsymbol{f}}$. Multiplication of two functions in the spatial domain corresponds to convolution in the Fourier domain, thus the coefficients of the product can be computed by a matrix multiplication. Let $F(g)$ be the Fourier convolution matrix corresponding to $g(\theta)$, then we can write

$$p(\theta) = g(\theta)f(\theta) \qquad \longleftrightarrow \qquad \widetilde{\boldsymbol{p}} = F(g)\widetilde{\boldsymbol{f}}. \tag{3.3}$$

The construction of $F(g)$ follows from standard trigonometric identities — the detail is presented in Appendix A. We will assume that the dimensions of the Fourier convolution matrices have been selected appropriately so that all multiplications and additions are well defined in the equations that follow.

Derivatives with respect to θ can also be written as a matrix multiplication. With $f(\theta)$ defined as before, let

$$g(\theta) = \frac{\partial f}{\partial \theta} \tag{3.4}$$

$$= 0 + \sum_{n>0} (n\widetilde{f}_{sn}(\tau)\cos(n\theta) - n\widetilde{f}_{cn}(\tau)\sin(n\theta)). \tag{3.5}$$

Vectorizing this we get

$$\widetilde{g} = D_\theta \widetilde{f} \tag{3.6}$$

where

$$D_\theta = \text{diag}\left[0, \begin{bmatrix} 0 & 1 \\ -1 & 0 \end{bmatrix}, \begin{bmatrix} 0 & 2 \\ -2 & 0 \end{bmatrix}, \ldots\right]. \tag{3.7}$$

Equations (3.3) and (3.6) allow us to vectorize all the expressions in the model.

3.3 Model With Quasi-Steady Viscous Flow Effects

We will study the compression system shown schematically in Figure 3.1. The system consists of a distortion screen, long upstream duct, actuator guide vanes (AGVs), a compressor, downstream duct, plenum, and throttle. The experimental compressor has a row of inlet guide vanes directly upstream of the AGVs (see Figure 2.4) that is not shown in this figure but will be accounted for in the modelling. Also shown in the figure is the axis system that will be used. The origin of the axial variable is taken at the face of the compressor.

3.3.1 Introduction

The following parameters will be used to nondimensionalize the various quantities.

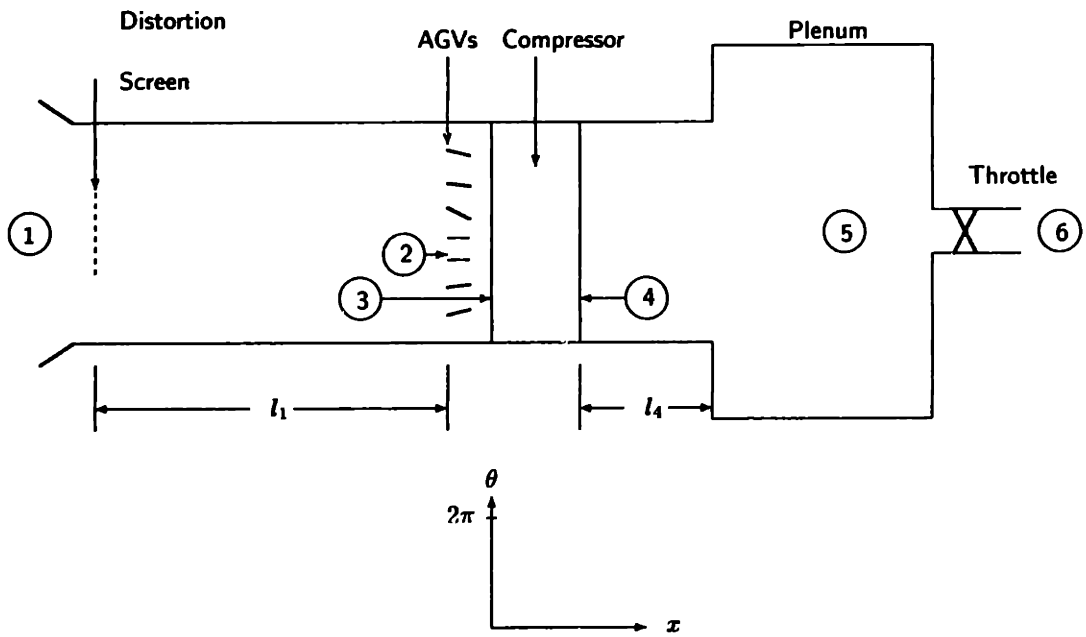

Figure 3.1: Compression System.

$\bar{r}$ = mean rotor radius

u_w = mean wheel speed

ρu_w^2 = dynamic head based on wheel speed,

ρ = density of air under operating conditions.

The following nondimensional independent variables are used.

θ = angle around annulus, positive in direction of rotor rotation.

τ = nondimensional time = (time)$u_w/\bar{r}$

x = nondimensional axial position, origin is at compressor face (see Figure 3.1)

The state of the system is described in terms of the axial and circumferential flow velocities, and total and static pressure. The model is presented in nondimensional form only and, to simplify notation, the nondimensionalization will not be shown explicitly, e.g., we will write p instead of $p/(\rho u_w^2)$. The main variables are

$$
\begin{aligned}
p_s(\theta,\tau,x) &= (\text{static pressure - } p_{\text{atmosphere}})/(\rho u_w^2) \\
p_t(\theta,\tau,x) &= (\text{total pressure - } p_{\text{atmosphere}})/(\rho u_w^2) \\
\phi(\theta,\tau,x) &= \text{flow coefficient} = (\text{axial velocity})/u_w \\
\gamma(\theta,\tau) &= \text{AGV deflection angle; we assume a continuum of blades.}
\end{aligned}
$$

The dependence on the independent variables will often be omitted.

The semi-actuator disk model uses the geometry of the compressor and the axisymmetric compressor characteristic. The parameters are

$$
\begin{aligned}
\psi(\phi,\gamma) &= \text{nondimensional steady state axisymmetric total-to-static pressure rise across the compressor.} \\
\psi_i(\phi) &= \text{nondimensional isentropic total-to-static pressure rise which follows from the torque work done on the air.} \\
\mu_r &= \text{rotor fluid inertia} = \sum_j \frac{b_{rj}}{\cos\gamma_{rj}} \text{ where } b_{rj} \text{ is the nondimensional rotor blade chord at midspan for the } j\text{th stage, and } \gamma_{rj} \text{ is the corresponding rotor stagger angle.}
\end{aligned}
$$

μ_s = same as μ_r but for stators.

μ_i = same as μ_r but for inlet guide vanes. The inlet guide vanes are not shown in Figure 3.1, see Figure 2.4 instead.

μ_c = $\mu_r + \mu_s + \mu_i$ = compressor fluid inertia.

μ_a = AGV fluid inertia = $\frac{b_a}{\cos \gamma_{s0}}$ where γ_{s0} is the circumferential mean AGV deflection.

x_m = nondimensional upstream axial location where all velocity and pressures are measured. Note that $x_m < 0$.

Steady state values will be indicated by a San Serif subscript s to distinguish them from the Roman subscript s that denotes stators. Station numbers as defined in Figure 3.1 will be denoted by parenthesized superscripts. All variables will be written as the sum of a steady state value plus a time varying perturbation; for example, the flow at the compressor face is

$$\phi^{(3)}(\theta, \tau) = \phi_s^{(3)}(\theta) + \delta\phi^{(3)}(\theta, \tau) \tag{3.8}$$

where δ indicates perturbation.

3.3.2 Pressure Balances

To derive the equations that express the flow in the compression system, pressure balances will be written for each component and then combined in an overall pressure balance for the complete system.

AGV pressure balance

The flow coefficient and pressure balance relations for the AGV operating under nonuniform steady flow are derived in Appendix B and are given by

$$\delta\phi^{(2)} = (1 + \mu_a \frac{\partial \gamma_s}{\partial \theta})\delta\phi^{(3)} + \mu_a \phi_s \frac{\partial}{\partial \theta}\delta\gamma \tag{3.9}$$

$$\triangleq f_\phi \delta\phi^{(3)} + f_\gamma \delta\gamma \tag{3.10}$$

$$\delta(p_t^{(3)} - p_t^{(2)}) = -\mu_a(1 + \frac{\mu_a}{2}\frac{\partial \gamma_s}{\partial \theta})\delta\dot{\phi}^{(3)} - \frac{\mu_a^2}{2}\phi_s \frac{\partial}{\partial \theta}\delta\dot{\gamma} \tag{3.11}$$

$$\triangleq p_{\dot{\phi}} \delta\dot{\phi}^{(3)} + p_{\dot{\gamma}} \delta\dot{\gamma}. \tag{3.12}$$

The expressions

$$f_\phi = 1 + \mu_a \frac{\partial \gamma_s}{\partial \theta} \tag{3.13}$$

$$f_\gamma = \mu_a \phi_s \frac{\partial}{\partial \theta} \tag{3.14}$$

defined in Equation (3.10) are independent of time and depend on the steady state AGV deflection γ_s and flow ϕ_s respectively so that they are functions of θ. The same holds true for

$$p_{\dot{\phi}} = -\mu_a(1 + \frac{\mu_a}{2}\frac{\partial \gamma_s}{\partial \theta}) \tag{3.15}$$

$$p_{\dot{\gamma}} = -\frac{\mu_a^2}{2}\phi_s \frac{\partial}{\partial \theta} \tag{3.16}$$

defined in Equation (3.12). Vectorizing Equations (3.10) and (3.12) using Equations (3.3) and (3.6) we get

$$\delta\widetilde{\boldsymbol{\phi}}^{(2)} = F_\phi \delta\widetilde{\boldsymbol{\phi}}^{(3)} + F_\gamma \delta\widetilde{\boldsymbol{\gamma}} \tag{3.17}$$

$$\delta(\widetilde{\boldsymbol{p}}_t^{(3)} - \widetilde{\boldsymbol{p}}_t^{(2)}) = P_{\dot{\phi}} \delta\dot{\widetilde{\boldsymbol{\phi}}}^{(3)} + P_{\dot{\gamma}} \delta\dot{\widetilde{\boldsymbol{\gamma}}}, \tag{3.18}$$

where

$$F_\phi = F(1 + \mu_a \frac{\partial \gamma_s}{\partial \theta}) \tag{3.19}$$

$$F_\gamma = F(\mu_a \phi_s) D_\theta \tag{3.20}$$

$$P_{\dot{\phi}} = -\mu_a F(1 + \frac{\mu_a}{2} \frac{\partial \gamma_s}{\partial \theta}) \tag{3.21}$$

$$P_{\dot{\gamma}} = -\frac{\mu_a^2}{2} F(\quad) D_\theta. \tag{3.22}$$

Upstream flow field

By taking the first integral of the axial momentum equation and nondimensionalizing we obtain [22]

$$\delta(p_t^{(2)} - p_t^{(1)}) = -\frac{1}{l_1} \delta\dot{\tilde{\phi}}_0^{(2)} - \sum_{n>0} \frac{1}{n} \left(\delta\dot{\tilde{\phi}}_{cn}^{(2)} \cos(n\theta) + \delta\dot{\tilde{\phi}}_{sn}^{(2)} \sin(n\theta) \right). \tag{3.23}$$

The equation is linear in the coefficients of $\delta\dot{\phi}^{(2)}$ so we can vectorize this by constructing a matrix

$$A_{21} = -\text{diag}\left[\frac{1}{l_1},\ 1, 1,\ \frac{1}{2}, \frac{1}{2},\ \frac{1}{3}, \frac{1}{3} \ldots, \right] \tag{3.24}$$

so that

$$\delta(\tilde{\boldsymbol{p}}_t^{(2)} - \tilde{\boldsymbol{p}}_t^{(1)}) = A_{21} \delta\dot{\tilde{\boldsymbol{\phi}}}^{(2)}. \tag{3.25}$$

We will work in terms of $\delta\phi^{(3)}$, the flow through the compressor. Substituting the time derivative of Equation (3.17) into Equation (3.25) gives

$$\delta(\tilde{\boldsymbol{p}}_t^{(2)} - \tilde{\boldsymbol{p}}_t^{(1)}) = A_{21} F_\phi \delta\dot{\tilde{\boldsymbol{\phi}}}^{(3)} + A_{21} F_\gamma \delta\dot{\tilde{\boldsymbol{\gamma}}}. \tag{3.26}$$

Compressor Pressure Balance

The total-to-static pressure rise across the compressor has been developed by Hynes and Greitzer [22]

$$p_s^{(4)} - p_t^{(3)} = \psi(\phi, \gamma) - \mu_r \frac{\partial \phi^{(3)}}{\partial \theta} - \mu_c \dot{\phi}^{(3)} \tag{3.27}$$

where $\psi(\phi, \gamma)$ is the steady inlet-total to exit-static pressure rise in axisymmetric flow, μ_r is the rotor fluid inertia, and $\mu_c = \mu_r + \mu_s + \mu_i$ is the total fluid inertia in the compressor. Linearizing this equation about the nonuniform steady flow ϕ_s we get

$$\delta(p_s^{(4)} - p_t^{(3)}) = \left[\frac{\partial \psi}{\partial \phi} - \mu_r \frac{\partial}{\partial \theta}\right] \delta\phi^{(3)} + \frac{\partial \psi}{\partial \gamma} \delta\gamma - \mu_c \delta\dot{\phi}^{(3)}. \tag{3.28}$$

Recall that $\frac{\partial \psi}{\partial \phi}$ and $\frac{\partial \psi}{\partial \gamma}$ are functions of θ. Vectorizing the last equation gives

$$\delta(\widetilde{p}_s^{(4)} - \widetilde{p}_t^{(3)}) = \left[F(\frac{\partial \psi}{\partial \phi}) - \mu_r D_\theta\right] \delta\widetilde{\phi}^{(3)} - \mu_c \delta\dot{\widetilde{\phi}}^{(3)} + F(\frac{\partial \psi}{\partial \gamma}) \delta\widetilde{\gamma}. \tag{3.29}$$

Downstream Ducts

Here we assume that the steady state compressor exit flow through a row of high solidity stators is axial and that there are no downstream obstructions. Under these conditions the static pressure is circumferentially uniform and will be the same as the plenum pressure [22]

$$p_s^{(4)} = p_s^{(5)}. \tag{3.30}$$

Using mass conservation through the compressor and the high solidity exit condition, Hynes and Greitzer [22] have shown that the downstream static pressure perturbations satisfy

$$\delta(p_s^{(5)} - p_s^{(4)}) = -\frac{1}{l_4} \delta\dot{\widetilde{\phi}}_0^{(3)} - \sum_{n>0} \frac{1}{n} \left(\delta\dot{\widetilde{\phi}}_{cn}^{(3)} \cos(n\theta) + \delta\dot{\widetilde{\phi}}_{sn}^{(3)} \sin(n\theta)\right). \tag{3.31}$$

We vectorize this equation in the same way as Equation (3.23) to get

$$\delta(\widetilde{p}_s^{(5)} - \widetilde{p}_s^{(4)}) = A_{54} \delta\dot{\widetilde{\phi}}^{(3)} \tag{3.32}$$

where

$$A_{54} = -\text{diag}\left[\frac{1}{l_4},\ 1,1,\ \frac{1}{2},\frac{1}{2},\ \frac{1}{3},\frac{1}{3}\ldots,\right]. \tag{3.33}$$

Plenum Dynamics

The nonuniform steady flow introduces coupling between the different harmonics, including the zeroth harmonic, and it is thus necessary to include pressure perturbations in the plenum in the description. Assuming that the pressure and density changes in the plenum can be related isentropically and that the flow through the throttle can be described by

$$p_s^{(5)} - p_s^{(6)} = \frac{1}{2}k_t\phi_0^2 \tag{3.34}$$

where k_t is the throttle constant, we obtain

$$\delta\dot{p}_s^{(5)} = \frac{-1}{4b_G^2 l_t k_t \tilde{\phi}_{s0}}(\delta p_s^{(5)} - \delta p_s^{(5)}) + \frac{1}{4b_G^2 l_t}\delta\phi_0^{(3)} \tag{3.35}$$

where

$$l_t = l_1 + l_4 + \mu_a + \mu_c \qquad \text{(effective compressor length)} \tag{3.36}$$

$$b_G = \frac{u_w}{2u_s}\sqrt{\frac{\text{Plenum volume}}{\text{Duct area} \times l_t}} \tag{3.37}$$

and u_s is the speed of sound. Note that we assume $\delta p_s^{(6)}$ to be nonzero and thus it acts as an external forcing function. Only the last term on the right hand side of Equation (3.35) needs vectorization. All we need to do here is construct a matrix that selects the zeroth harmonic of $\delta\phi^{(3)}$. The matrix has a single row with the first element equal to one and the rest of the elements zero. Thus

$$\delta\dot{p}_s^{(5)} = \frac{-1}{4b_G^2 l_t k_t \tilde{\phi}_{s0}}(\delta p_s^{(5)} - \delta p_s^{(6)}) + A_{5\phi}\delta\tilde{\phi}^{(3)} \tag{3.38}$$

$$A_{5\phi} = [\frac{1}{4b_G^2 l_t},\ 0,\ 0,\ldots]. \tag{3.39}$$

This completes the pressure balances for the compression system.

The overall pressure balance for the perturbations is given by

$$\delta(p_s^{(6)} - p_t^{(1)}) = (\delta p_s^{(6)} - \delta p_s^{(5)}) + (\delta p_s^{(5)} - \delta p_s^{(4)}) + (\delta p_s^{(4)} - \delta p_t^{(3)})$$
$$+ (\delta p_t^{(3)} - \delta p_t^{(2)}) + (\delta p_t^{(2)} - \delta p_t^{(1)}). \tag{3.40}$$

Substituting from the corresponding equations and simplifying we get

$$\begin{bmatrix} \delta\dot{\tilde{\phi}}^{(3)} \\ \delta\dot{p}_s^{(5)} \end{bmatrix} = \begin{bmatrix} A_{\dot{\phi}}^{-1}[F(\frac{\partial\psi}{\partial\phi}) - \mu_r D_\theta] & A_{\dot{\phi}}^{-1}A_{\phi 5} \\ A_{5\phi} & -1/(4b_G^2 l_t k_t \tilde{\phi}_{s0}) \end{bmatrix} \begin{bmatrix} \delta\tilde{\phi}^{(3)} \\ \delta p_s^{(5)} \end{bmatrix}$$
$$+ \begin{bmatrix} A_{\dot{\phi}}^{-1}F(\frac{\partial\psi}{\partial\gamma}) \\ 0 \end{bmatrix} \delta\tilde{\gamma} + \begin{bmatrix} A_{\dot{\phi}}^{-1}[A_{21}F_\gamma + P_{\dot{\gamma}}] \\ 0 \end{bmatrix} \delta\dot{\tilde{\gamma}}$$
$$+ \begin{bmatrix} A_{\dot{\phi}}^{-1} & 0 \\ 0 & 1/(4b_G^2 l_t k_t \tilde{\phi}_{s0}) \end{bmatrix} \begin{bmatrix} \delta\tilde{p}_t^{(1)} \\ \delta p_s^{(6)} \end{bmatrix} \tag{3.41}$$

$$\triangleq A\delta x + B\delta\tilde{\gamma} + E\dot{\tilde{\gamma}} + G[\delta\tilde{p}_t^{(1)},\ \delta p_s^{(6)}]^T \tag{3.42}$$

where

$$A_{\dot{\phi}} = \mu_c I - A_{21}F_\phi - P_{\dot{\phi}} - A_{54} \tag{3.43}$$

$$A_{\phi 5} = [1,\ 0,\ 0,\ \ldots]^T \tag{3.44}$$

and I is the identity matrix. We will denote the state vector $[\delta\tilde{\phi},\ \delta p_s^{(5)}]^T$ by δx.

Note that we assumed the total pressure perturbation $\delta p_t^{(1)}$ is nonzero. We thus have two external sources, $\delta p_t^{(1)}$ and $\delta p_s^{(6)}$, that force the system. These sources, called process noise in the control and estimation literature, will be used to study the effect of external noise on the system.

When we compare with experiments the velocity measurements $\delta\tilde{\phi}^{(x_m)}$ are taken upstream of the AGVs. We must therefore take the decaying potential field into account; the nth harmonic decays with e^{nx_m} (x is negative upstream). The state vector is defined in terms of $\delta\phi^{(3)}$ so we also need the relation between $\delta\phi^{(2)}$ and $\delta\phi^{(3)}$ given in Equation (3.17). Thus

$$E^{(x_m)} = \text{diag}[1, \quad e^{x_m}, e^{x_m}, \quad e^{2x_m}, e^{2x_m}, \ldots] \tag{3.45}$$

$$\delta\tilde{\phi}^{(x_m)} = E^{(x_m)}\delta\tilde{\phi}^{(2)} \tag{3.46}$$

$$= \left[E^{(x_m)}F_{\phi}, \quad 0\right]\delta x + E^{(x_m)}F_{\gamma}\delta\tilde{\gamma} \tag{3.47}$$

$$\triangleq C\delta x + D\delta\tilde{\gamma}. \tag{3.48}$$

The zero at the end of the matrix in Equation (3.47) multiplies the plenum pressure perturbations, the last state in the state vector δx.

Equation (3.42) contains the derivative of the control signal with respect to time so that it is not in the usual state space form. It can be converted to the usual form with the following transformation. Let

$$\delta z = \delta x - E\delta\tilde{\gamma}. \tag{3.49}$$

Applying this transformation to Equations (3.42) and (3.48)we get

$$\delta\dot{z} = A\delta z + (B + AE)\delta\tilde{\gamma} + G[\delta\tilde{p}_t^{(1)}, \ \delta p_s^{(6)}]^T \tag{3.50}$$

$$\delta\tilde{\phi}^{(x_m)} = C\delta z + (D + AE)\delta\tilde{\gamma} \tag{3.51}$$

that has the desired form. We note that the final state space description given by Equations (3.50) and (3.51) is input-output equivalent to Equations (3.42) and (3.48) but not state equivalent. We can recover the original state vector δx from the relation in Equation (3.49) if it is needed. However, for the homogeneous system $\delta\tilde{\gamma} = 0$ so that $\delta z = \delta x$

and we can use Equation (3.50) for eigenstructure analysis. The model just derived will be referred to as the basic Hynes-Greitzer model.

Before we can compute the matrices of the state space model we need to find the nonuniform steady flow ϕ_s. The equation that needs to be solved and solution method are discussed in the next section.

3.3.3 Steady State

The equation describing the steady state is obtained by writing a pressure balance for the system as we did in the previous section, but this time the pressure balance is for the steady variables. Because we are interested in the steady state solution all derivatives with respect to time can be set to zero to give

$$p_t^{(1)} - p_s^{(6)} = -\psi(\phi_c) + \mu_r \frac{\partial \phi_s}{\partial \theta} + \frac{1}{2} k_t \tilde{\phi}_{s0}^2. \tag{3.52}$$

The equation can be vectorized as before; the detail is omitted here. Once we have decided on an operating point (by specifying either the mean flow $\tilde{\phi}_{s0}$ or throttle constant k_t), and the shape, magnitude, and extent of the total pressure distortion $p_t^{(1)}(\theta)$, Equation (3.52) can be solved for the remaining unknown variables. Assume, as would be the case in an experiment, we have specified k_t so that all the coefficients of ϕ_s are unknown. In general we will need an infinite number of harmonics for ϕ_s. For practical purposes we approximate the solution with a finite number of harmonics so that the right hand side of Equation (3.52) will not equal the left hand side. By defining the error in the approximation as the difference between the left and right hand side of Equation (3.52) we can find a least squares solution for ϕ_s.

We are mainly interested in computing the linearized dynamics although steady state quantities are also important. We will use the relative error in the dominant poles and zeros

as a measure to determine the number of harmonics in the steady velocity $\phi_s(\theta)$ and number harmonics needed for the linearized dynamics $\delta\phi$. The "exact" values of the dominant poles and zeros are defined as those values obtained with a large number of harmonics. Once we have determined the number of harmonics needed to obtain the "exact" values, we determine the number of harmonics needed to give a desired relative error, for example 0.1%. By its very nature the procedure to determine the number of harmonics is iterative.

The actual number of harmonics needed for a good approximation is quite low. Through simulations it was found that if we want to compute the first n *modes* (that is, the eigenvalues (or poles) and corresponding eigenvectors) of the linearized dynamics accurately we need approximately $8n$ *harmonics* for ϕ_s. Once we have solved for ϕ_s we keep only the first $4n$ harmonics and use this truncated Fourier series to compute the linearized model. We need to start with about twice as many harmonics for ϕ_s as we are interested in to ensure that the $4n$ harmonics that we need are computed accurately. This can be explained as follows. If we multiply $\cos p\theta$ by $\cos q\theta$ we get products of the form $\cos(p+q)\theta$ and $\cos(p-q)\theta$ so that higher harmonics effects the lower harmonics.

Similarly, we need approximately $4n$ harmonics for the perturbations $\delta\phi^{(3)}$ in the state vector. We will see later that only the first four *modes* are needed to model the system for frequencies up to three rotor revolutions so that we need approximately 16 harmonics for $\delta\phi^{(3)}$ and initially 32 harmonics (plus the zeroth harmonic) for ϕ_s. Each harmonic needs two coefficients so that Equation (3.52) represents 41 coupled differential equations and the order of the state space model is 22. Solving the steady flow and computing the state space model takes about 2 minutes on an IBM RS6000 work station. The numbers quoted are conservative and apply to a square wave distortion. For distortions without discontinuities, e.g., a cosine, all the computations can be done with $4n$ harmonics.

All the experiments indicated that (for this particular compressor) four modes were

enough to capture the dynamics up to three rotor revolutions. It thus is possible to reduce the order of the final state space model from 22 down to eight for controller design. However, to get to this low number of states we need to start out with a rather large number of harmonics.

3.4 A Simple Approximation for Unsteady Viscous Behavior

In the semi-actuator disk model an instantaneous change in flow through the compressor results in an instantaneous change in pressure rise. Experiments by Nagano [35] and Mazzawy [32] have shown that total pressure changes lags a change in the flow and that this lag can be approximated quite well by a simple first order system with time constant one to two times the flow-through time. For simplicity, all the lags in the rotors will be lumped together. Similarly, the lags in the stators will also be lumped together. Haynes et al [21] used this approach with great success. We should note here that Longley [25] has found that in some compressors it is more important to model deviations rather than losses. Haynes et al [21] found deviation lags not to be important for this compressor. The absence of deviations here does not limit the generality of the model or the results and can be added if the need arises.

The additional dynamics can be included in the basic Hynes-Greitzer model by making two changes. First, we modify the expression that describes the pressure rise across the compressor to include the effect of the lags. Then we add the additional differential equations to the state space model, see Haynes et al [21].

The assumption is that the total pressure losses can be modelled by

$$l = l_r + l_s \tag{3.53}$$

$$= \psi_i - \psi \tag{3.54}$$

where

$$l = \text{total pressure loss in rotors and stators}$$

$$= \widetilde{l}_0 + \sum_{n>0} \widetilde{l}_{cn} \cos(n\theta) + \widetilde{l}_{sn} \sin(n\theta) \tag{3.55}$$

ψ_i is the ideal inlet-total to exit-static pressure rise, and l_r and l_s are the losses in rotors and stators respectively. It is further assumed that the contribution of the losses in the rotors and stators is in proportion to the reaction r of the compressor blading

$$l_r = rl \tag{3.56}$$

$$l_s = (1 - r)l. \tag{3.57}$$

With these definitions we can write

$$\psi = \psi_i - l_r - l_s. \tag{3.58}$$

The second change is the addition of differential equations for rotor and stator losses. The lags for the rotor and stator losses can be modelled by first order systems

$$\tau_r(\frac{\partial l_r}{\partial \tau} + \frac{\partial l_r}{\partial \theta}) = -l_r + l_{rs} \tag{3.59}$$

$$\tau_s \frac{\partial l_s}{\partial \tau} = -l_s + l_{ss}. \tag{3.60}$$

The time constants τ_r and τ_s are proportional to the flow-through times in the rotors and stators respectively

$$\tau_r(\theta) = \tau_f \frac{\bar{b}_r}{\phi(\theta)} \tag{3.61}$$

$$\tau_s(\theta) = \tau_f \frac{\bar{b}_s}{\phi(\theta)} \tag{3.62}$$

where $\bar{b}_r$ and $\bar{b}_s$ are the mean rotor and stator lengths respectively, and τ_f is a constant typically in the range 1.0–1.5. Linearizing Equations (3.59) - (3.62) about the steady state values ϕ_s, l_{rs}, and l_{ss} we get

$$\frac{\partial \delta l_r}{\partial \tau} = -(\frac{1}{\tau_r} + \frac{\partial}{\partial \theta})\delta l_r + \frac{1}{\tau_r}\frac{\delta l_{rs}}{\delta \phi}\delta \phi^{(3)} \tag{3.63}$$

$$\frac{\partial \delta l_s}{\partial \tau} = -\frac{1}{\tau_s}\delta l_s + \frac{1}{\tau_s}\frac{\delta l_{ss}}{\delta \phi}\delta \phi^{(3)}. \tag{3.64}$$

These equations can be vectorized and included in the basic analysis. The results are summarized in Table 3.1 on page 65. This model will be referred to as the extended Hynes-Greitzer model (XHG).

The parameters of the three-stage compressor is listed in Table 3.2 on page 66.

Steady State

Inclusion of the unsteady loss response also changes the equation for the steady flow and we discuss the necessary changes here. As before we need to modify the pressure rise expression and add a set of differential equations. The expression for the pressure rise modification has already been given in Equation (3.58). In steady state Equation (3.60) simplifies to a trivial identity and in Equation (3.59) we simply put the derivative with respect to time equal to zero. The final set of differential equations that must be solved are also shown in Table 3.1.

To solve the steady flow equations we need initial estimates for ϕ_s and l_s. A good initial guess is the steady state solution from the basic model, with zero as an initial estimate for the losses. Furthermore, it was found that the number of harmonics needed in all the calculations can be reduced by about 30%. The order of the final state space system is now about three times as large as the basic model due to the two additional sets of differential

Table 3.1: Extended Hynes-Greitzer model.

The steady flow ϕ_s and steady losses l_{rs} and l_{ss} are given by the solution of

$$p_t^{(1)} - p_s^{(6)} = -\psi_i + l_{rs} + l_{ss} + \mu_r \frac{\partial \phi}{\partial \theta} + \frac{1}{2} k_t \tilde{\phi}_{so}^2 \tag{3.65}$$

$$\tau_r \frac{\partial l_r}{\partial \theta} = -l_r + l_{rs}. \tag{3.66}$$

The complete state space description is given by

$$\delta \dot{\boldsymbol{x}} = A \delta \boldsymbol{x} + B \delta \tilde{\gamma} + E \delta \dot{\tilde{\gamma}} + G[\delta \tilde{\boldsymbol{p}}_t^{(1)}, \delta p_s^{(6)}]^T, \tag{3.67}$$

$$\delta \boldsymbol{x} = \left[\delta \tilde{\boldsymbol{\phi}}^{(3)}, \quad \delta \tilde{\boldsymbol{l}}_r, \quad \delta \tilde{\boldsymbol{l}}_s, \quad \delta p_s^{(5)}\right]^T, \tag{3.68}$$

$$A_{\dot{\phi}} = \mu_c I - A_{21} F_{\phi} - P_{\dot{\phi}} - A_{54} \tag{3.69}$$

$$A_{\phi 5} = [1,\ 0,\ 0,\ \ldots]^T \tag{3.70}$$

$$A_{5\phi} = [\frac{1}{4 b_G^2 l_t},\ 0,\ 0, \ldots] \tag{3.71}$$

$$A = \begin{bmatrix} A_{\dot{\phi}}^{-1}[F(\frac{\partial \psi}{\partial \phi}) - \mu_r D_\theta] & -A_{\dot{\phi}}^{-1} & -A_{\dot{\phi}}^{-1} & -A_{\dot{\phi}}^{-1} A_{\phi 5} \\ F(\phi_s \frac{\partial l_{rs}}{\partial \phi})/(\tau_f \bar{b}_r) & -[F(\phi_s)/(\tau_f \bar{b}_r) + D_\theta] & 0 & 0 \\ F(\phi_s \frac{\partial l_{ss}}{\partial \phi})/(\tau_f \bar{b}_s) & 0 & -[F(\phi_s)/(\tau_f \bar{b}_s) + D_\theta] & 0 \\ A_{5\phi} & 0 & 0 & -1/(4 b_G^2 l_t k_t \tilde{\phi}_{so}) \end{bmatrix} \tag{3.72}$$

$$B = \begin{bmatrix} A_{\dot{\phi}}^{-1} F(\frac{\partial \psi}{\partial \gamma}) \\ 0 \\ 0 \\ 0 \end{bmatrix} \qquad E = \begin{bmatrix} A_{\dot{\phi}}^{-1}[A_{21} F_\gamma + P_{\dot{\gamma}}] \\ 0 \\ 0 \\ 0 \end{bmatrix} \qquad G = \begin{bmatrix} A_{\dot{\phi}}^{-1} & 0 \\ 0 & 0 \\ 0 & 0 \\ 0 & 1/(4 b_G^2 l_t k_t \tilde{\phi}_{so}) \end{bmatrix} \tag{3.73}$$

Table 3.2: Three-stage compressor model parameters.

Nominal operating speed $u_w = 72$ m/s at 2400 revolutions per minute.

Geometric parameters.

$$\begin{aligned} \mu_r &= 0.6792 & \mu_s &= 0.3335 \\ \mu_a &= 0.2863 & \mu_i &= 0.0709 \\ \bar{b}_r &= 0.1184 & \bar{b}_s &= 0.1079 \\ l_1 &= 2.9923 & l_4 &= 1.5294 \\ b_G &= 0.1631 & x_m &= -0.6 \\ \bar{r} &= 286 \text{ mm} \end{aligned} \tag{3.74}$$

Pressure rise characteristics (measured by Haynes [20]); see Figure 3.2 p.67.

$$\psi = -10.07\phi^2 + 9.4306\phi - 1.1849$$

$$\psi_i = -15.5341\phi^3 + 24.1238\phi^2 - 15.0262\phi + 4.6951$$

$$\frac{\partial \psi}{\partial \gamma} = 2.8880\phi^2 - 3.6550\phi + 0.8251$$

Loss parameters.

$$r = 0.75$$

$$\tau_f = 1.5$$

---

equations (typically 60-80 states). As before, only four modes are needed to capture the dynamics up to three rotor revolutions so that the model can again be reduced to eight states, but this time significantly more computational work is needed before we can get down to this number. Solving for the steady flow of the extended model and computing the state space matrices takes about 5 times as long as with the basic model.

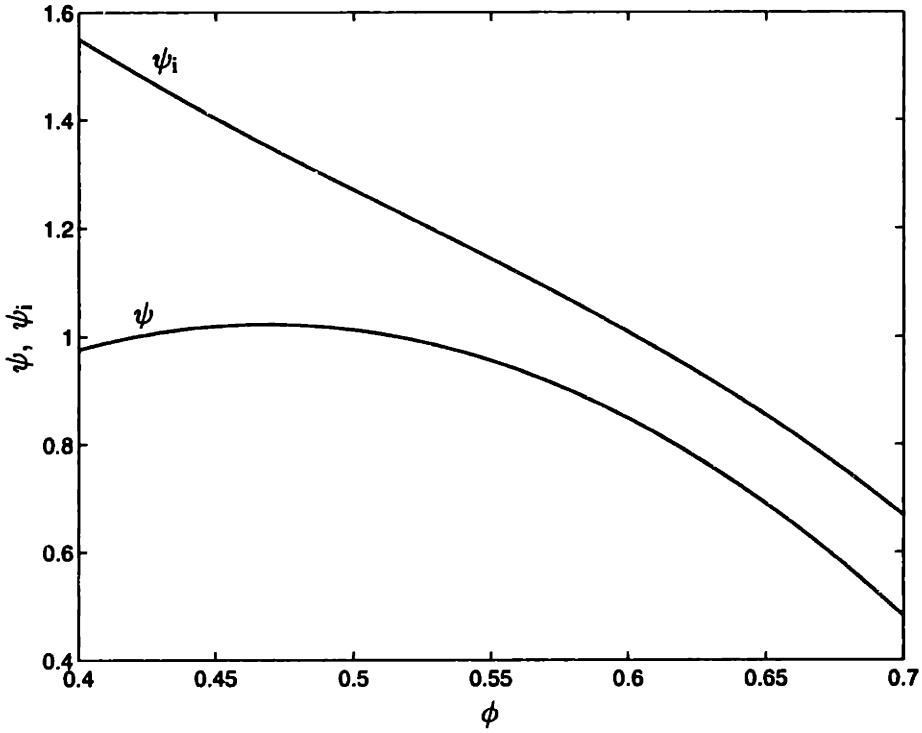

Figure 3.2: Three-stage compressor pressure rise characteristics.

3.5 Complex Transfer Functions

The state space model derived in the previous section tells us how the system behaves in the time domain. It is often convenient to analyze the system in the frequency domain by looking at transfer functions. For rotating systems it is attractive to view the inputs and outputs as phasors, and phasors are best represented as complex numbers. In this section we show how to transform the real-input real-output state space description to a complex-input complex-output description. The resulting transfer function will be called a complex transfer function. This is a slight misnomer because a transfer function is always complex — the term complex refers to the fact that we are using complex input and output signals.

The nth complex Fourier coefficient of the flow perturbation is defined by

$$\delta\widetilde{\phi}_n(\tau) = \delta\widetilde{\phi}_{cn}(\tau) + i\delta\widetilde{\phi}_{sn}(\tau). \tag{3.75}$$

Coefficients for negative values of n are conjugates of the corresponding positive valued coefficients. We note that this definition differs from the usual relation between real and complex Fourier coefficients. This nonstandard definition is used so that the resulting phasor rotates in the same direction as the rotor. In exactly the same way we define

$$\delta\widetilde{\gamma}_n = \delta\widetilde{\gamma}_{cn} + i\delta\widetilde{\gamma}_{sn} \tag{3.76}$$

for the AGV deflections. The expressions for computing the transfer function from $\delta\widetilde{\gamma}_n$ to $\delta\widetilde{\phi}_n$ given the real input-output state description is derived in Appendix C.1. All the transfer functions shown will be for complex inputs and outputs.

Power density spectra (PSDs) are used quite often to analyze the experimental data and here, too, we will compute the temporal spectral densities of the complex coefficients defined in Equation (3.75). The Fourier transform of a complex function does not have conjugate symmetry so that the PSD at positive frequencies will be different from the corresponding negative frequencies. See also Paduano [37].

3.6 Modal Analysis

In this section we discuss the distorted flow mode shapes and compare them to the uniform flow mode shapes.

The pole pattern of the neutrally stable system as predicted by the extended model is shown in Figure 3.3. The corresponding mode number is shown next to the eigenvalues. We now explain how the modes were numbered by considering the mode shapes.

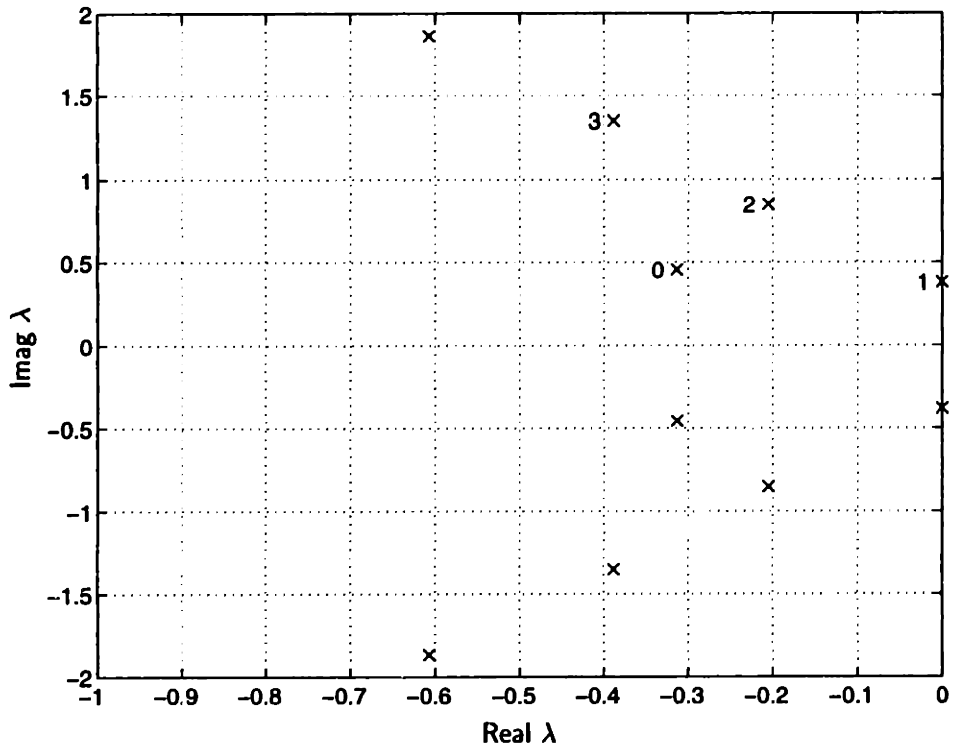

Figure 3.3: Eigenvalues of marginally stable system, 1.9 dynamic head distortion. The numbers 0, 1, 2, and 3 to the left of the eigenvalues indicate the mode number. Note that only the eigenvalues close to the origin are shown in this figure.

The mode shapes and relative strength of the harmonics in the four dominant modes are shown in Figure 3.4. The dominant modes are defined as those with eigenvalues closest to the origin. The mode shapes shown in these figures were all computed from the eigenvectors of the $A-$matrix (see Chapter 3). This choice was made as the eigenvectors are time invariant while the mode shapes are time varying. Putting it another way, the mode shapes obtained from the eigenvectors correspond to the mode shapes at time zero. In these figures the magnitude of the largest harmonic (or plenum pressure perturbation $\delta p_s^{(5)}$) was normalized.

The mode with eigenvalue $\lambda = -0.31 + 0.46i$ (top right hand graph) has a strong first

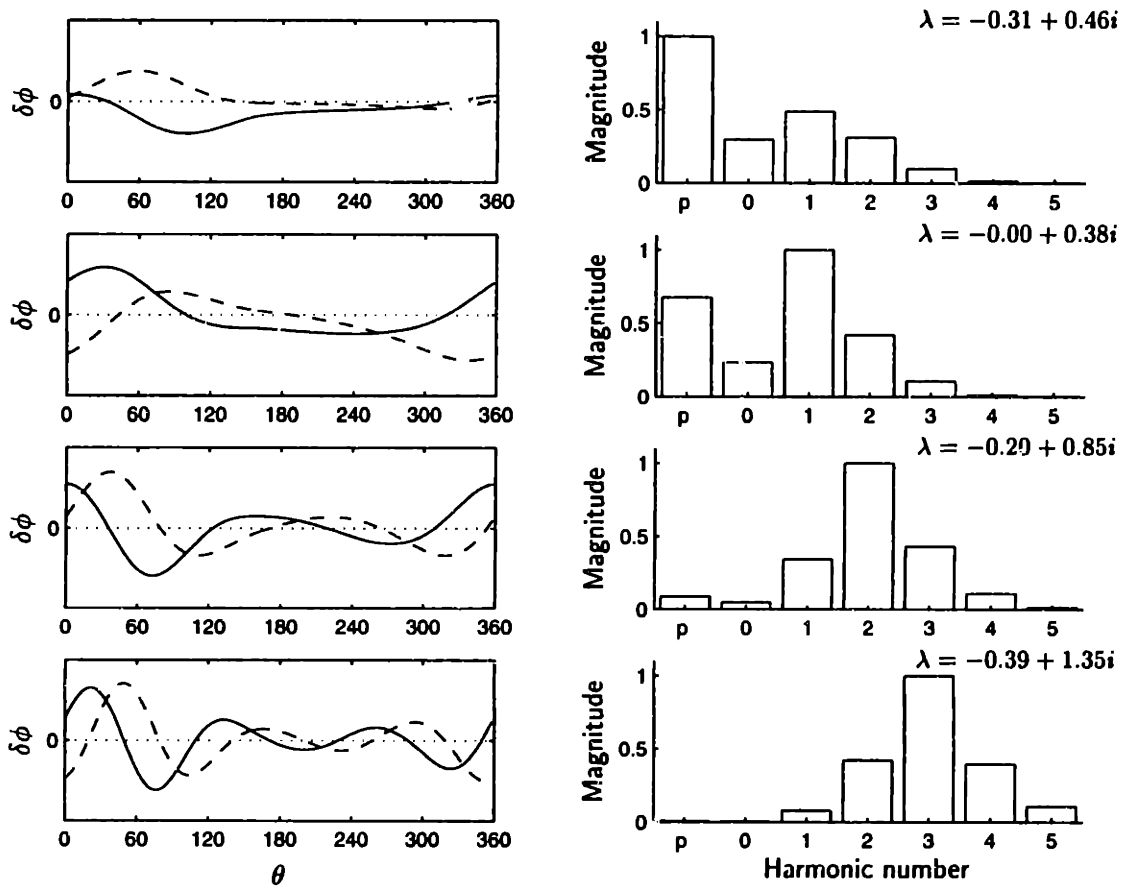

Figure 3.4: Mode shapes (left) and corresponding harmonic contribution (right). The solid and dashed lines show the real and imaginary parts of the mode shape respectively. The harmonic number indicated by p is the plenum pressure perturbations $\delta p_s^{(5)}$, 1.9 dynamic head distortion.

harmonic component. However, the large contribution of the plenum pressure perturbation $\delta p_s^{(5)}$ and presence of the zeroth harmonic suggest that this is a surge-like mode, and we will therefore refer to it as the zeroth mode. Note that the second harmonic also has significant presence in the mode. The real and imaginary parts of the corresponding mode shape at time $\tau = 0$ is shown in the top left graph.

The neutrally stable mode shown in the second set of graphs from the top in Figure 3.4 also has strong first harmonic content but the magnitude of the plenum pressure perturba-

tion $\delta p_s^{(5)}$ is smaller. We thus call this the first mode. The zeroth and second harmonics also have substantial contributions to this mode.

For the other two modes shown at the bottom of the figure the contributions of the zeroth harmonic and $\delta p_s^{(5)}$ decreased greatly and the modes consist mainly of the dominant harmonic plus the adjacent harmonics. These two modes will be called the second and third modes respectively. The higher spatial frequency content is clearly visible in the mode shapes of the second and third harmonics.

In all four cases the mode shapes are not purely sinusoidal and have large deviations outside the distorted region $120° \leq \theta \leq 240°$. In Chapter 4 we saw that the wave envelope was also large outside the distorted region. With distortion, irrespective of the mode that is excited, the envelope of the small perturbations will be nonuniform around the annulus. We note that the real and imaginary parts reflect the mode shape at two different points in time and thus give an idea of how the mode shapes change with time.

Neither the shapes nor the harmonic content of the modes change significantly as the extent of the distortion is changed to 180°. The magnitude of the distortion has a much larger effect. Figures 3.5 and 3.6 show the modes and harmonic contribution for 0.8 dynamic head distortion and for uniform flow respectively. The order of the modes in these figures is the same as in Figure 3.4. For the 0.8 dynamic head distortion the contribution of the first harmonic to the zeroth mode is less than half that with the 1.9 dynamic head distortion because the smaller magnitude distortion introduces less coupling between the harmonics. Similar arguments hold for the other modes. The mode shapes are also more sinusoidal compared to 1.9 dynamic head distortion. For uniform flow the mode shapes are purely sinusoidal with no coupling between the harmonics.

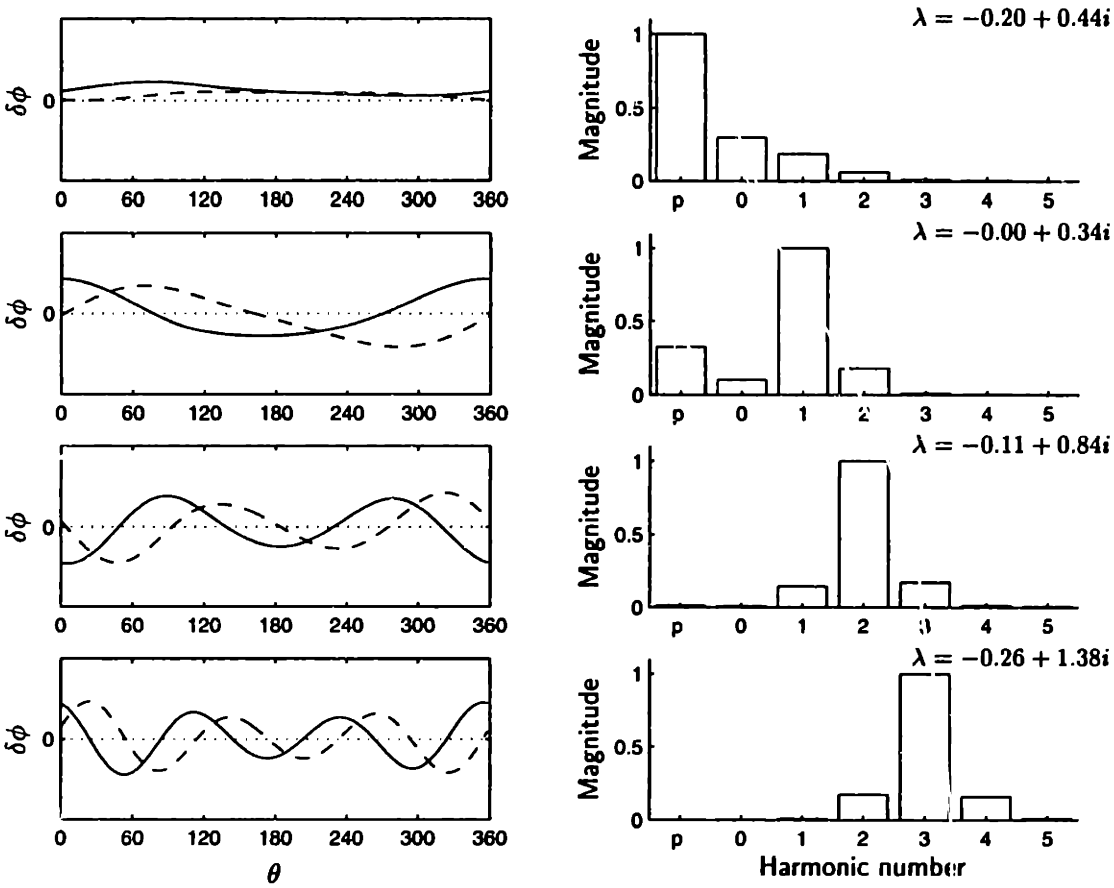

Figure 3.5: Mode shapes (left) and corresponding harmonic contribution (right). The solid and dashed lines show the real and imaginary parts of the mode shape respectively. The harmonic number indicated by p is the plenum pressure perturbations $\delta p_s^{(5)}$, 0.8 dynamic head distortion.

3.7 Why is Distortion a Hard Problem?

In this section we describe the main reasons that make control of rotating stall a harder problem in the presence of distortion.

Figure 3.7 shows the variation of the real part of the most unstable pole as a function of the distortion extent. The flow coefficient was held constant at 1% above the uniform flow open loop stall point while the extent was varied from 0°to 360°.

Without distortion (extent=0) the system is stable, that is, the real part of the eigen-

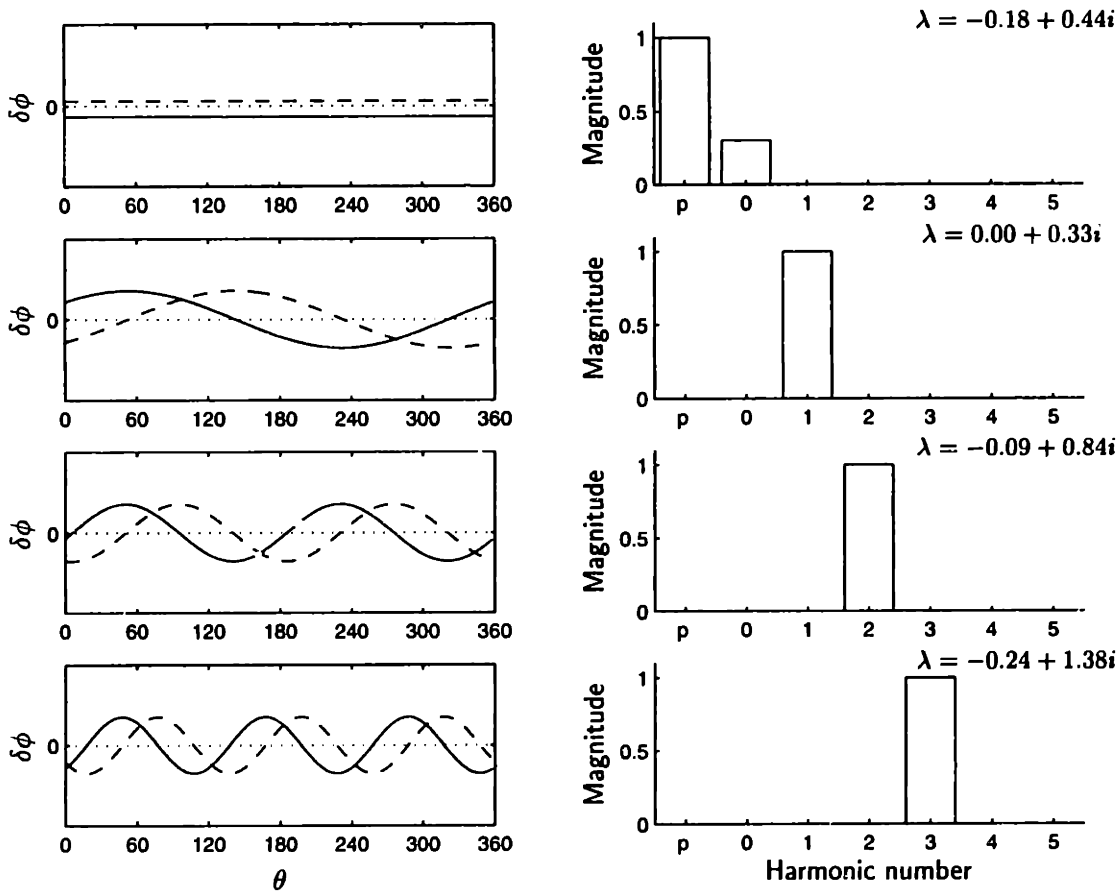

Figure 3.6: Mode shapes (left) and corresponding harmonic contribution (right). The solid and dashed lines show the real and imaginary parts of the mode shape respectively. The harmonic number indicated by p is the plenum pressure perturbations $\delta p_s^{(5)}$, uniform flow.

value λ is negative. As the extent of the distortion is increased the pole moves closer to the $i\omega$−axis and goes unstable at approximately 70° and remains unstable up to an extent of 230°. The real part of the pole assumes its maximum positive (most unstable) value at approximately 135°. This is a worst case situation and was the motivation for using a distortion with 120° extent.

Also shown in the figure is the real part of the dominant zero. The zero shows a similar trend but crosses the $i\omega$−axis at a smaller extent and stays in the right half plane over

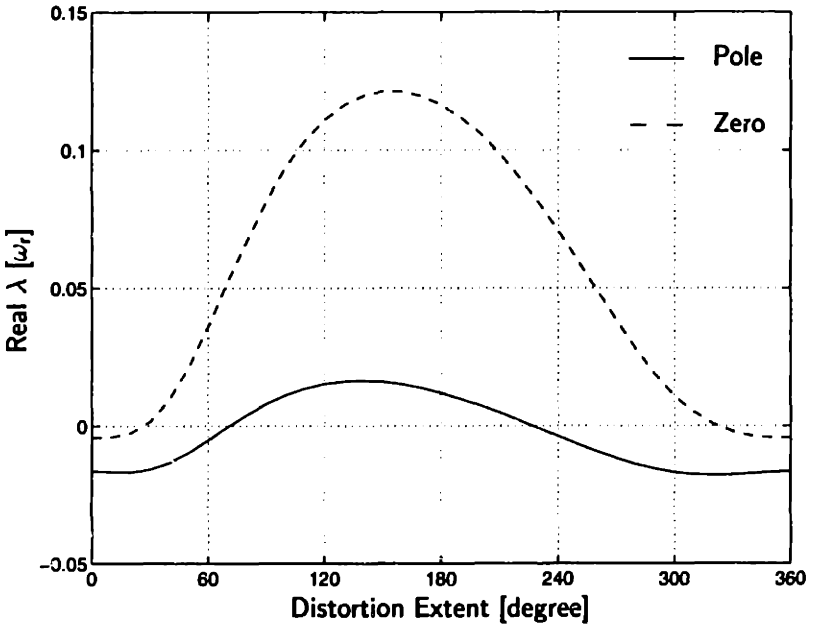

Figure 3.7: Effect of distortion extent on the most unstable pole and dominant zero, $\widetilde{\phi}_{s0} = 0.465$, 1.9 dynamic head distortion.

a larger range of extents. Zeros in the right half plane (that is, the real part of the zero is positive) are called nonminimum phase zeros and have an adverse effect on closed loop system performance.

Nonminimum phase zeros limit the performance of a feedback system in the following sense. Let the transfer function of the system and controller be denoted by $G(i\omega)$ and $K(i\omega)$ respectively, and let $|G(i\omega)K(i\omega)| \geq k > 1$ for $0 \leq \omega \leq \omega_c$. The gain-bandwidth product $k\omega_c$ is then limited and the frequency of the nonminimum phase zero is an upper bound for ω_c. See Maciejowski [30]. A limit in the gain-bandwidth product often translates into a limit on the bandwidth of the closed loop system. Therefore, an increase in k will result in more attenuation of disturbances, but over a smaller range of frequencies.

Systems with nonminimum phase zeros often have poor rejection of measurement noise [30]. We showed in Section 4.2.2 that the magnitude of the noise was larger for distorted flow and we can expect that this will have a negative effect on controller performance.

We saw in Figure 3.7 that the dominant zero is nonminimum phase for a large range of extents. Further, Figure 3.8 shows the dominant zeros for uniform flow, 0.8 and 1.9 dynamic head distortions (extent=120°). The zero becomes nonminimum phase at higher mass flows for larger distortions. The zeros of the uniform flow and 0.8 dynamic head

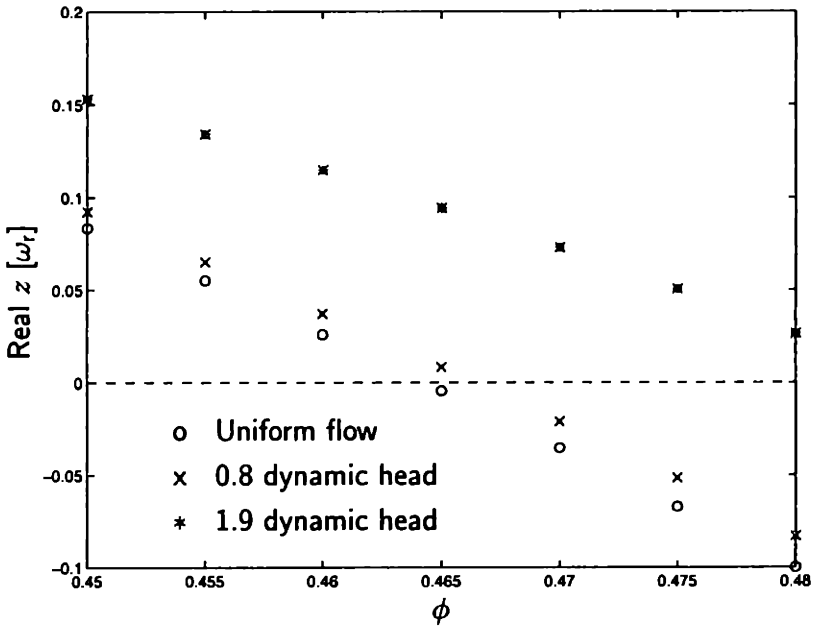

Figure 3.8: Real part of dominant zeros as function of ϕ for uniform flow, 0.8 and 1.9 dynamic head distortions.

distortion systems become nonminimum phase at approximately $\phi = 0.464$ and $\phi = 0.467$ respectively. Over the range of flow coefficients shown, the zero of the system with a 1.9 dynamic head distortion is always nonminimum phase.

Whether a zero is minimum or nonminimum phase is strongly affected by the type and configuration of sensors and actuators. For example, the model predicts that measuring velocity between the first rotor and stator instead of upstream of the compressor will increase the frequency of the nonminimum phase zero by 50% for the 1.9 dynamic head distortion. An increased frequency implies an increased gain-bandwidth product, thus we

expect an increase in the performance of the controller. Whether this results in measurable improvement in performance is investigated in Chapter 5.

In summary, the detrimental effect of distortion is twofold. First, a compressor operating in the presence of distortion becomes unstable at higher flow coefficients. Second, the dominant zeros become nonminimum phase at higher flow coefficients, limiting the closed loop bandwidth and increasing the sensitivity to measurement noise.

---

4 Experimental Results: Open Loop

In this chapter we assess the predictive capability of the extended Hynes-Greitzer model for steady state and dynamic compressor behavior. Comparison is made with compressor behavior with distortions of two magnitudes, 0.8 and 1.9 dynamic heads. Because the results were generally similar, unless stated otherwise, all the discussions in this chapter is for the 1.9 dynamic head distortion.

The chapter is divided into four parts. The first part presents the steady state velocity and pressure profiles, and pressure rise characteristics. Next, the unforced dynamics of the compression system is analyzed in the time and frequency domain (spectral analysis). This is followed by a comparison of the predicted and measured forced response of the compression system. The chapter ends with a summary.

4.1 Steady State Results

In this section we assess the steady state predictive capability of the model. Steady state results are important for two reasons. First, the nonlinear model is linearized about the nonuniform steady velocity so that an accurate estimate of the velocity is desirable. Second, the steady pressure rise in the presence of distortion is an important measure of performance.

4.1.1 Steady state profiles

The steady flow obtained by solving the nonlinear equations (3.65) and (3.66) gives the flow at the inlet of the first rotor. Pressure measurements, however, were carried out at a station

approximately 0.6 mean radii upstream of the compressor face (see Figure 2.4). We therefore comment first on the relation between these measurements and the flow at the inlet of the first rotor. The upstream static pressure decays exponentially. We can compute the static pressure and velocity at the sensor location by multiplying the nth harmonic of the static pressure at the inlet of the first rotor by $e^{n x_m}$. Predicted and measured static pressures are shown in Figure 4.1. The experiment and analytical profile (with mean values subtracted) of the XHG model are shown. The profiles have the same shape and the magnitudes agree well.

Gong [15] has relaxed the assumption that the upstream flow field can be modelled in a linearized way and used a full nonlinear Euler model instead; we will refer to this model as the XHG-Euler model. The result from his calculations is also shown in Figure 4.1 and again there is good agreement with the experimental results. This shows that the nonlinear effects in the unsteady flow field are small. In all the figures the extended Hynes-Greitzer and Euler models will be indicated by XHG and XHG-Euler respectively.

The predicted and measured steady state velocity profiles at the measurement location $x = x_m$ are shown Figure 4.2. The velocity predicted by the XHG-Euler model matches the measured profile in magnitude well. The width of the distorted region is slightly wider than the predicted width. The model predicts a lower velocity in the distorted region. This can be explained by comparing the predicted and measured total and static pressure shown in Figure 4.3. In this figure we see that the mean value of the measured static pressure is lower than the predicted pressure by 10% so that the predicted difference between total and static pressures in the distorted region is smaller than measured, resulting in a lower estimated velocity. This is especially true at approximately 200° where the predicted velocity (Figure 4.2 shows a large drop. The lower static pressure may be due to radial redistribution upstream of the compressor.

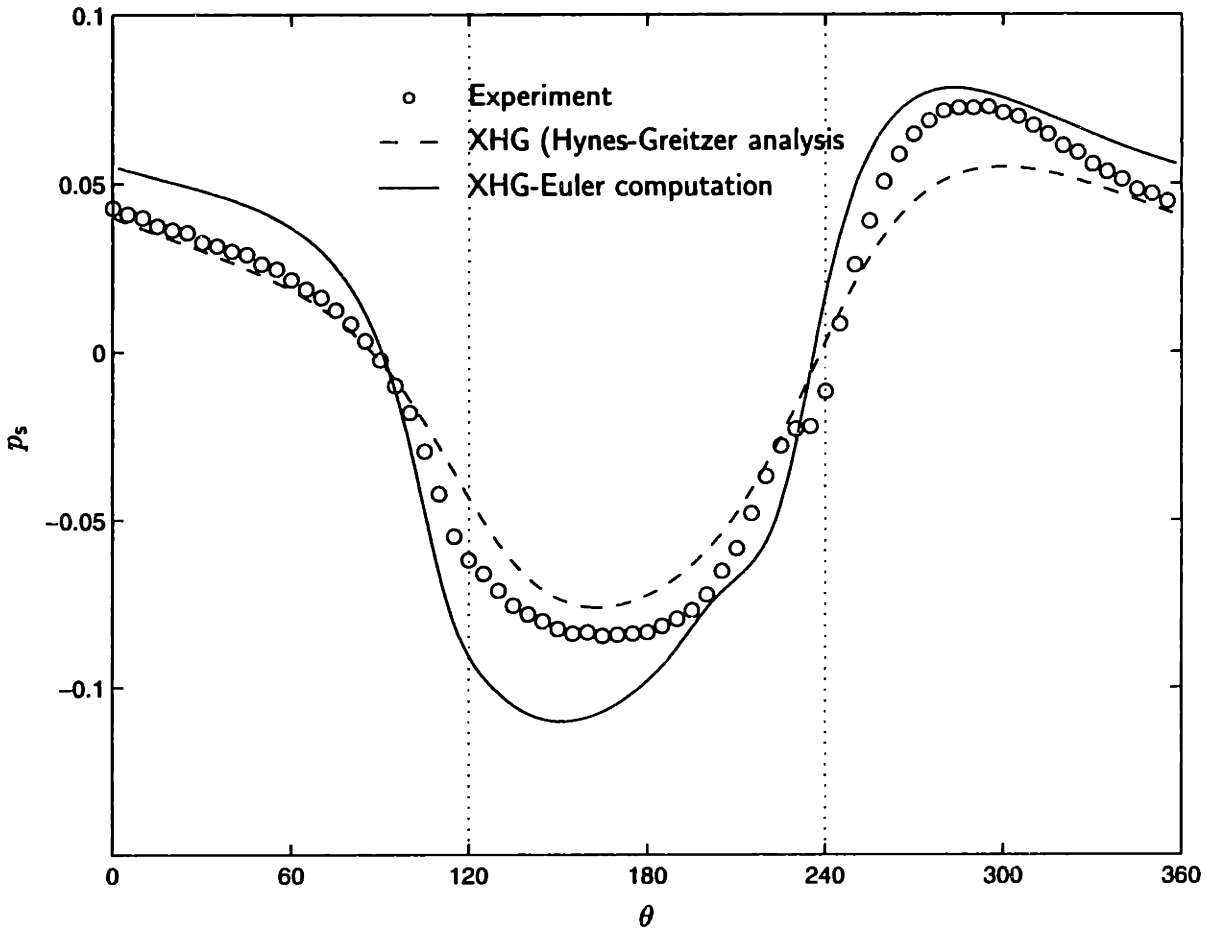

Figure 4.1: Static pressure at $x = x_m, \widetilde{\phi}_{s0} = 0.5$, 1.9 dynamic head distortion. The mean values have been subtracted to show the variation around the annulus. The distortion screen blocked the flow in the range $120° < \theta < 240°$ shown by the dotted lines.

In Figure 4.3 we also show the deviation of the exit static pressure $p_s^{(4)}$. The assumption was made that the exit static pressure is uniform around the annulus and we see the measurements support this assumption.

In Figure 4.4 we compare the velocities at the compressor face predicted by the XHG and XHG-Euler models; no velocity measurements are available at this location. The magnitudes of the velocities agree very well and the only difference between the profiles is due to the narrowing of the flow field.

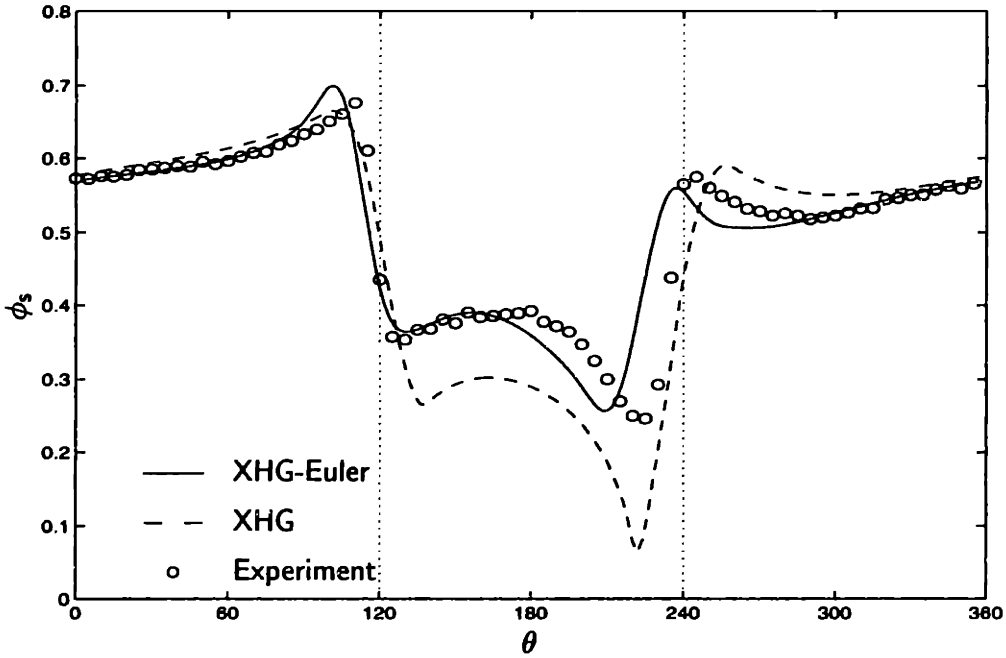

Figure 4.2: Steady state velocity profiles at $x = x_m$, $\widetilde{\phi}_{s0} = 0.5$ 1.9 dynamic head distortion.

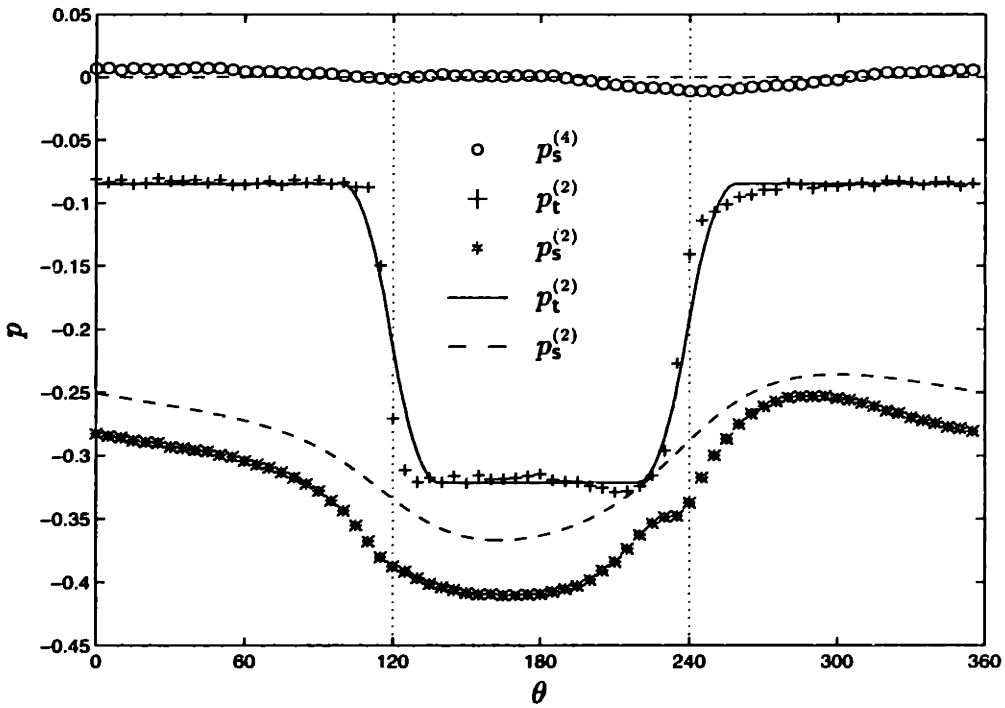

Figure 4.3: Total and static pressures, $\widetilde{\phi}_{s0} = 0.5$, 1.9 dynamic head distortion. The mean value of the static pressure at the compressor exit $p_s^{(4)}$ has been subtracted to reveal the variation around the annulus. The solid and dashed lines are for the extended Hynes-Greitzer model.

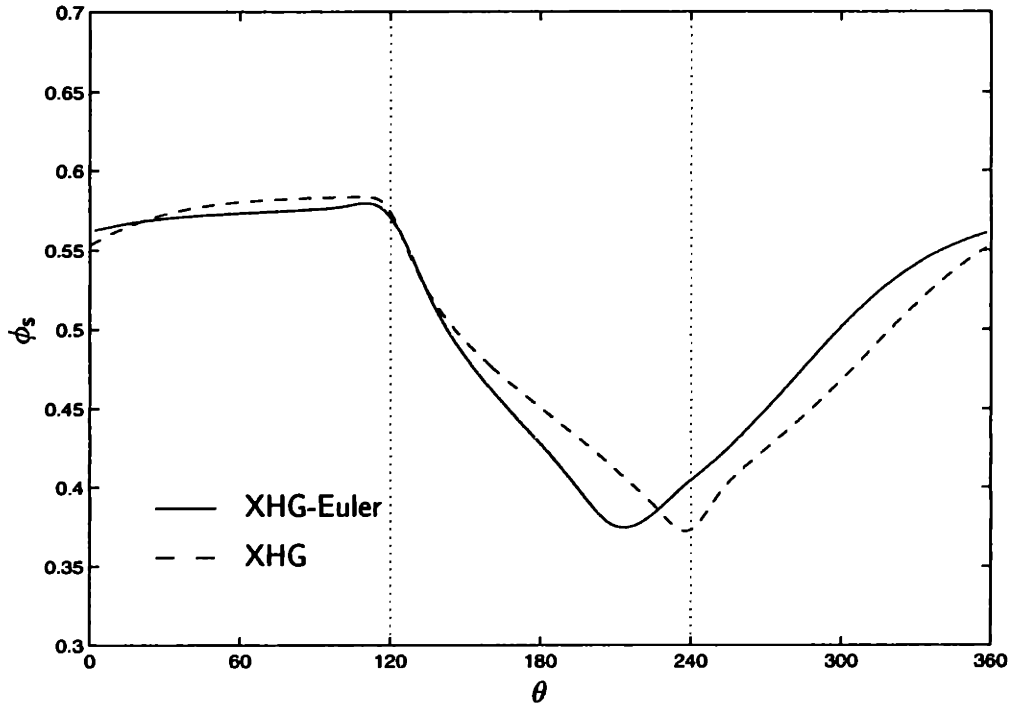

Figure 4.4: Steady state velocity profile at $x = 0, \widetilde{\phi}_{s0} = 0.5$.

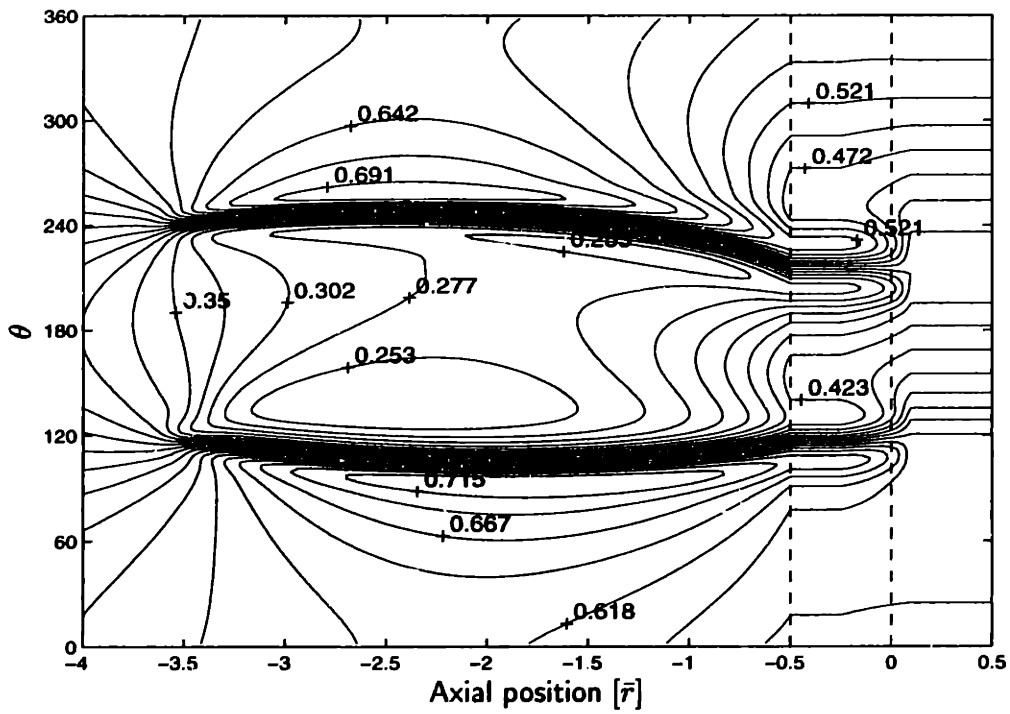

Figure 4.5: Axial velocity contours predicted by XHG-Euler model. The vertical dashed lines at $x = -0.5$ and $x = 0$ locate the inlet guide vanes and compressor face respectively.

Velocity contours in the $x - \theta$ plane calculated by the XHG-Euler model are shown in Figure 4.5. The narrowing of the low stagnation pressure region is clearly visible between roughly 100° and 220°. We also note the slight asymmetry in the region of the distortion screen at $x \approx -3.5$ suggesting some interaction between the compressor and distortion generator. (The XHG-Euler model assumes an infinitely long duct upstream of the screen while the experimental setup has a bellmouth.)

We can also estimate tangential velocity using the following procedure. We assume that the irrotational part of the velocity equals the difference between the velocities far upstream and at the sensor location; this is shown in the graph at the top of Figure 4.6. This gives enough information to solve for the tangential velocity which is compared against the tangential velocity obtained from the Euler model in the graph at the bottom of Figure 4.6. Outside the regions where the axial velocity ϕ_s has large gradients and the assumption thus not likely to be correct, there is good agreement between the experimentally derived and predicted velocities. This again, is a comparison that shows that nonlinear effects will be very localized as far as the upstream flow field.

4.1.2 Speed lines

Measured and predicted compressor performance curves for the 0.8 and 1.9 dynamic head total pressure distortions are shown in Figures 4.7 and 4.8 respectively. For the 0.8 dynamic head distortion the loss in pressure rise and the increase in stalling flow coefficient are small. The loss in pressure rise is 1.6% and the stalling flow coefficient increased by 0.4%. Both these numbers are predicted correctly by the XHG model. The large distortion clearly shows the detrimental effect of distortion — the pressure rise dropped by 7.6% and the stalling flow coefficient increased by 4.3%. The model predicted an increase of 2.0% in stalling flow coefficient and a drop in peak pressure rise of 4.4%. The characteristic that has been used

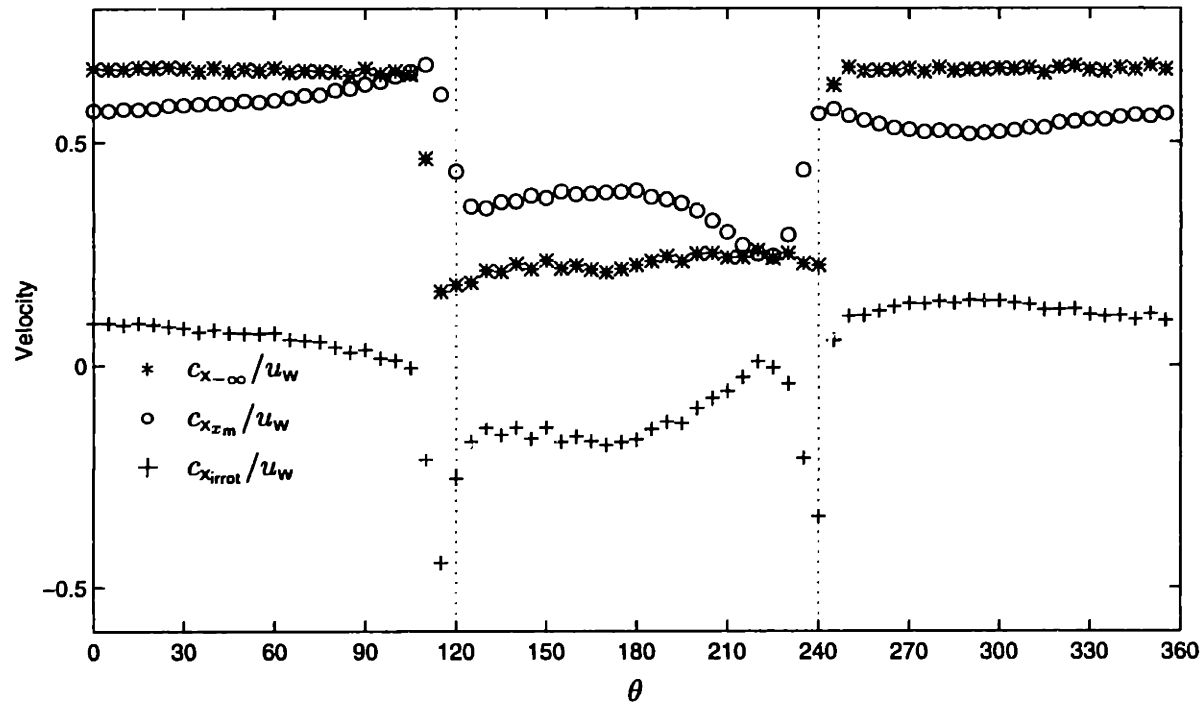

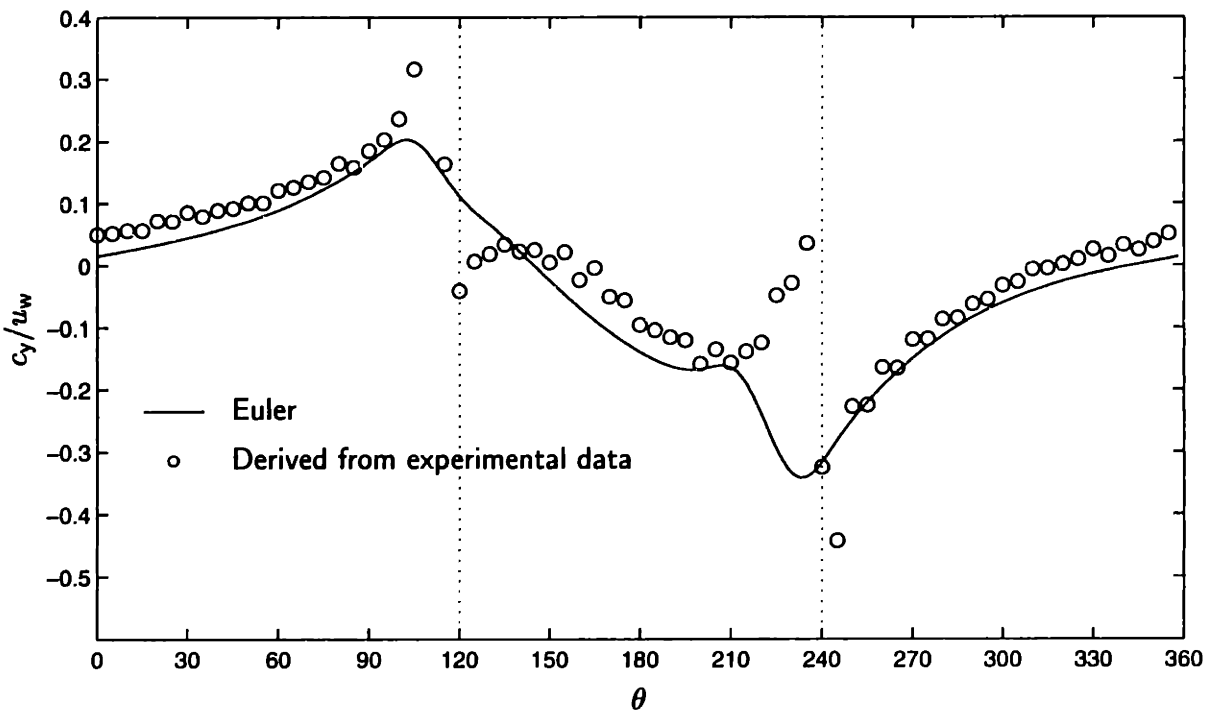

Figure 4.6: Computation of tangential velocity.

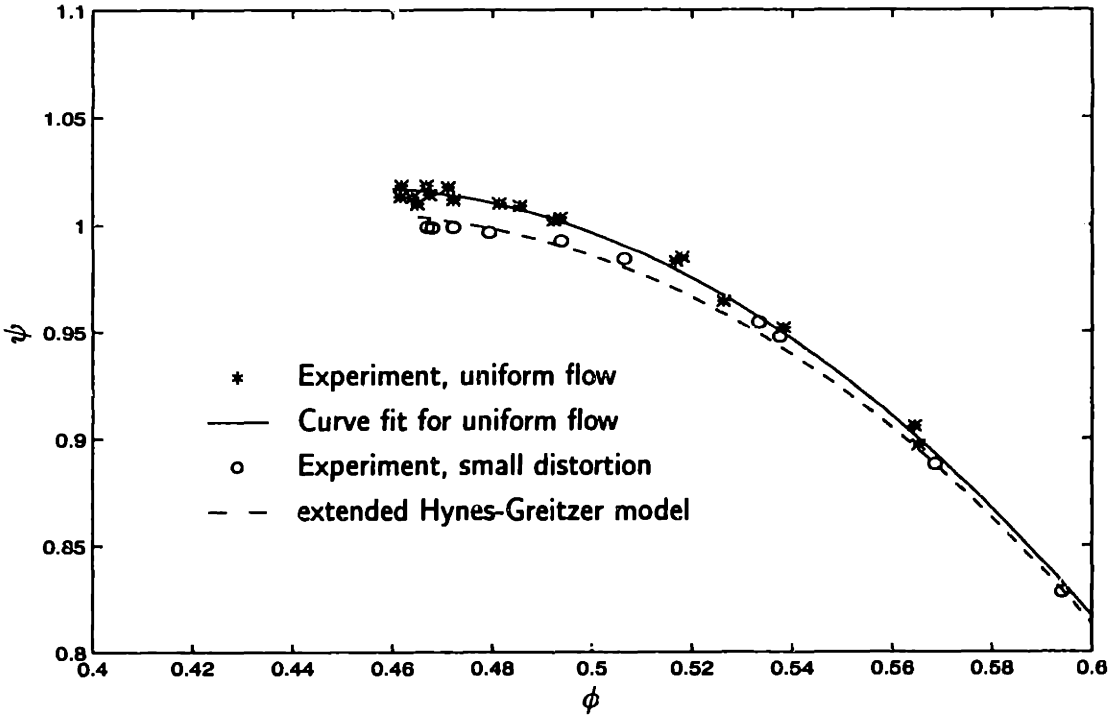

Figure 4.7: Compressor performance line for 0.8 dynamic head distortion.

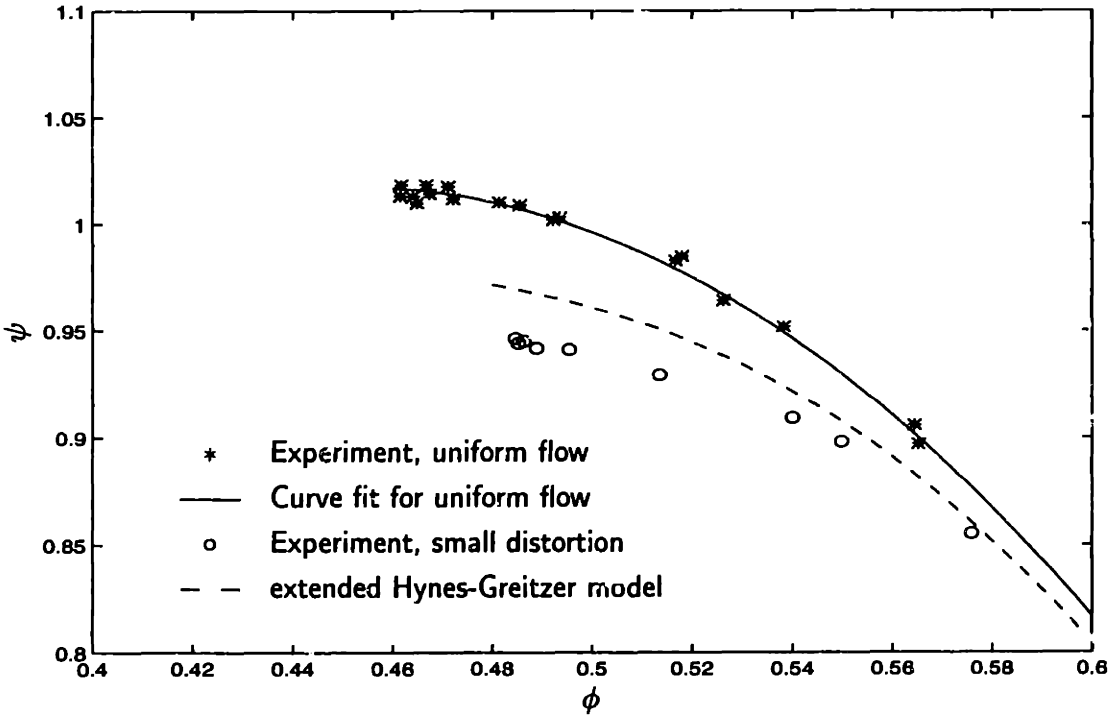

Figure 4.8: Compressor performance line for 1.9 dynamic head distortion.

was measured by Haynes [20] (see 3.2 on page 66) over the range $0.42 < \phi < 0.7$ and it has been assumed that the parabola that fits the data over this range of flow coefficients is also valid at flow coefficients down to 0.37, see Figure 4.4. The lower predicted stalling flow coefficient and smaller predicted drop in peak pressure rise suggest that the slope of the characteristic to the left of the peak ($\widetilde{\phi}_{so} = 0.460$) may be steeper than that of the parabola. Currently no method exists to measure the characteristic over the complete range of flow coefficients needed for the large distortion.

Table 4.1: Open loop stalling flow coefficients. Percentages are computed relative to $\phi = 0.460$.

	Uniform flow	120°, 0.8	120°, 1.9
ϕ_{stall} XHG model	0.460	0.462 0.4%	0.469 2.0%
ϕ_{stall} experiment	0.460	0.462 0.4%	0.480 4.3%

The extended model was used to obtain the predictions shown. The basic model predicts the trends but gives a higher stalling flow coefficient than the experiment. Despite this limitation the basic model will be shown to be a useful tool for designing controllers to stabilize the flow.

4.2 Dynamics

4.2.1 Time Domain Analysis

In this section we compare the dynamic behavior of the compression system with that predicted by the XHG model using time domain data. For the data available the signal to noise ratios (SNRs) of the velocity measurements are less than one so it is often difficult to distinguish the signal from the noise. The goal therefore is not so much to find how well the model predicts the behavior of the compression system but to observe trends of the small

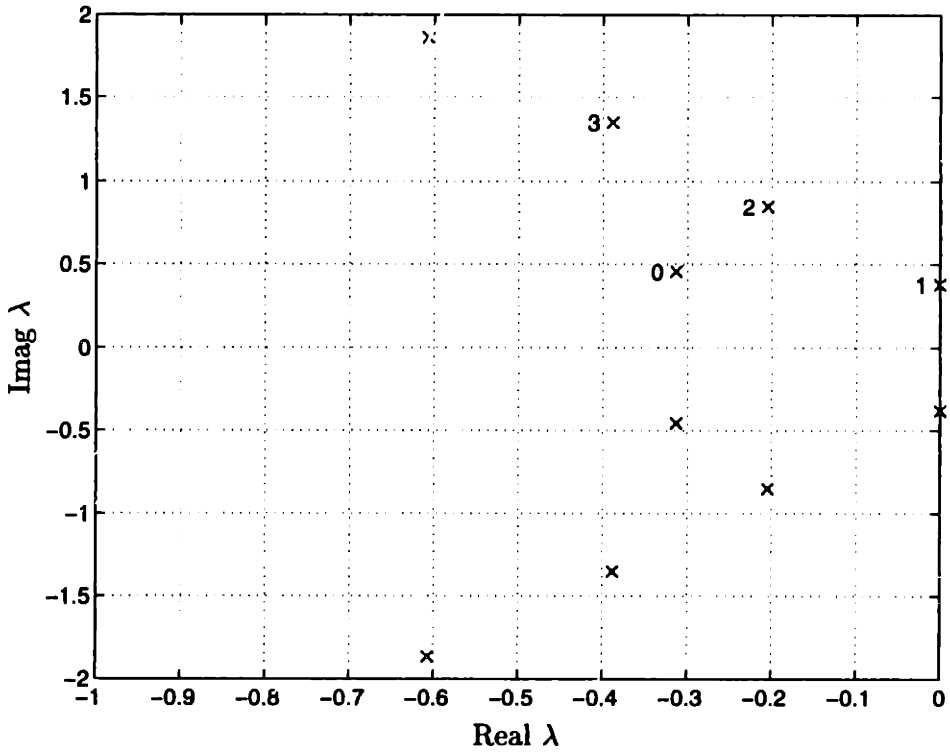

Figure 4.9: Eigenvalues of marginally stable system, 1.9 dynamic head distortion. The numbers 0, 1, 2, and 3 to the left of the eigenvalues indicate the mode number. Note that only the eigenvalues close to the origin are shown in this figure.

perturbation dynamics in the presence of distortion.

The pole pattern of the neutrally stable system as predicted by the extended Hynes-Greitzer model is shown in Figure 4.9. For reference we list the eigenvalues and corresponding mode number shown in the figure.

$$\lambda_0 = -0.31 + 0.46i \qquad \lambda_1 = -0.00 + 0.38i$$

$$\lambda_2 = -0.20 + 0.85i \qquad \lambda_3 = -0.39 + 1.35i.$$

In this figure we show only eigenvalues with magnitude less than $1.5\omega_r$ but a complete set

of eigenvalues will be shown later. We will refer to the neutrally stable mode with natural frequency $\omega_1 = 0.38$ as the first mode, similarly for others. The numbering of the modes was explained in Section 3.6.

We will compare the behavior of the experimental system just prior to stall with that of the unforced model when only the first mode has nonzero initial conditions. All the modes of the experimental system will be excited by noise. The marginally stable mode should dominate the behavior of the system, so it should correspond to the simulation. The homogeneous system

$$\delta\dot{\boldsymbol{x}} = A\delta\boldsymbol{x} \tag{4.1}$$

has the solution

$$\delta\boldsymbol{x} = e^{A\tau}\delta\boldsymbol{x}_0. \tag{4.2}$$

We will choose the initial state $\delta\boldsymbol{x}_0$ so that only the first *mode* is excited. The solution can be simplified if we express the $A-$matrix in terms of the eigenvalues and eigenvectors. Let

$$A = V\Lambda V^{-1}, \tag{4.3}$$

$$\text{where} \quad V = [\boldsymbol{v}_1, \boldsymbol{v}_2, \ldots] \quad \text{is the matrix of eigenvectors,} \tag{4.4}$$

$$\text{and} \quad \Lambda = \text{diag}[\lambda_1, \lambda_2, \ldots] \quad \text{is the matrix of eigenvalues.} \tag{4.5}$$

We assume without loss of generality that the first two eigenvalues and eigenvectors correspond to the neutrally stable mode so that $\lambda_1 = i\omega_1$, and $\lambda_2 = -i\omega_1$. With this choice

$$\delta\boldsymbol{x} = \Re(\boldsymbol{v}_1)\cos(\omega_1\tau) - \Im(\boldsymbol{v}_1)\sin(\omega_1\tau) \tag{4.6}$$

where $\Re$ and $\Im$ indicate the real and imaginary part respectively. Let the eigenvector be

$v_1 = [v_0, v_{c1}, v_{s1}, v_{c2}, v_{s2}, \ldots]^T$ then the reconstructed perturbation is

$$\begin{aligned}\delta\phi(\theta,\tau) &= \Re(v_0)\cos(\omega_1\tau) - \Im(v_0)\sin(\omega_1\tau) \\ &\quad + \sum_{n>0}[\Re(v_{cn})\cos(\omega_1\tau) - \Im(v_{cn})\sin(\omega_1\tau)]\cos(n\theta) \\ &\quad + \sum_{n>0}[\Re(v_{sn})\cos(\omega_1\tau) - \Im(v_{sn})\sin(\omega_1\tau)]\sin(n\theta) \qquad (4.7) \\ &\triangleq \delta\tilde{\phi}_0 + \sum_{n>0}\delta\tilde{\phi}_{cn}\cos(n\theta) + \delta\tilde{\phi}_{sn}\sin(n\theta). \qquad (4.8)\end{aligned}$$

Notice that the frequency of oscillation of the coefficients $\delta\tilde{\phi}_0$, $\delta\tilde{\phi}_{cn}$, and $\delta\tilde{\phi}_{sn}$ of the nth harmonic is the *same* for all the harmonics, see Equations (4.7) and (4.8). The expressions for the coefficients can be simplified by using standard trigonometric identities to obtain

$$\begin{aligned}\delta\phi(\theta,\tau) &= a_{c0}\cos(\omega_1\tau) + a_{s0}\sin(\omega_1\tau) \\ &\quad + \sum_{n>0} a_{cn}\cos(n\theta - \omega_1\tau) + a_{sn}\sin(n\theta - \omega_1\tau) \\ &\quad + \sum_{n>0} b_{cn}\cos(n\theta + \omega_1\tau) + b_{sn}\sin(n\theta + \omega_1\tau) \qquad (4.9)\end{aligned}$$

and the amplitudes a_{c0}, a_{s0}, a_{cn}, a_{sn}, b_{cn}, and b_{sn} depend the elements of the eigenvector; the exact expressions are not relevant to our discussion. The important point is that a mode can be decomposed into two waves: one travelling in the direction of rotor rotation and one travelling in the opposite direction and, in general, these waves have different amplitudes and phases. Because the amplitudes of the two waves differ the wave shape will change with time. No assumptions were made about the distortion so Equations (4.8) and (4.9) hold in general.

An example of the waves predicted by Equation (4.8) (or equivalently Equation (4.9)) is shown in Figure 4.10. Five wave forms approximately equally spaced in time over one period are shown together with the envelope of the wave. The variation in magnitude of

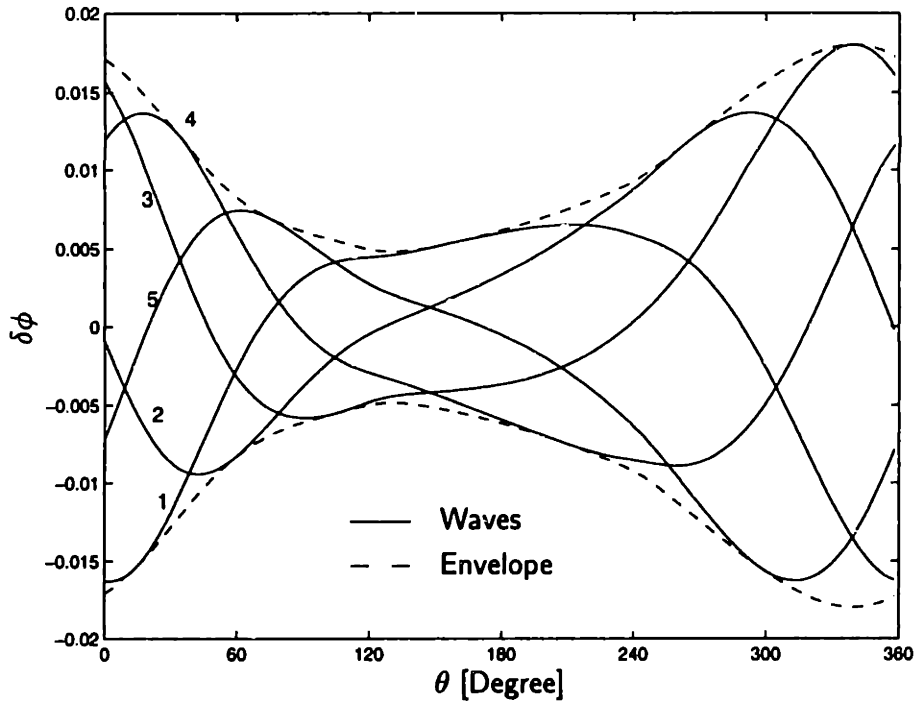

Figure 4.10: Velocity perturbations and envelope around annulus, 1.9 dynamic head.

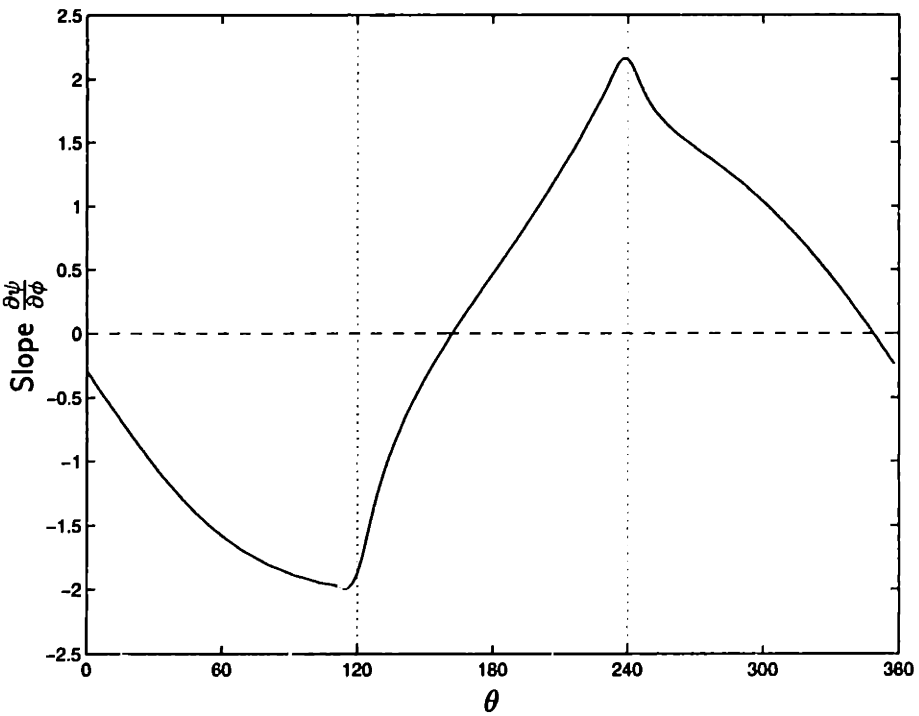

Figure 4.11: Slope around annulus, 1.9 dynamic head distortion.

the envelope around the annulus can be explained by looking at the slope $\frac{\partial \psi}{\partial \phi}$ shown in Figure 4.11. The magnitude of the envelope decreases when the slope is negative and increases when the slope is positive. Therefore, the magnitude of the envelope has a maximum where the slope changes from positive to negative.

A typical data set of stall inception is shown in Figure 4.12.

The origin of the time axis has been chosen as the point where the velocities exceed an arbitrary large limit. The exact value of the origin is not important as we are interested in the period prior to stall. Two properties predicted by the model are presented in the figure. Two parallel lines drawn through the peaks of the perturbations are used to help show that the wave is travelling around the annulus. An estimate of the speed at which the wave rotates can be obtained by counting the number of peaks in the trace at the bottom of the figure; between $\tau = -20$ and $\tau = -10$ there are a little more than four peaks giving a speed of just over $0.4\,\omega_r$ which agrees well with the predicted $0.38\,\omega_r$.

Second, if we look around the annulus at a fixed time (prior to stall) we see that the perturbation magnitude is large for small values of θ, decreases as θ increases, is small for $120° < \theta < 240°$, and increases again towards 360°; this is predicted by the model, see Figure 4.10.

Analysis of the perturbations around the annulus has shown that they are not distributed symmetrically about the mean values. The standard deviations (STDs) for positive and negative values of the perturbations are shown in Figure 4.13 where we see that for negative values of the perturbations the STDs match the envelope well, but for positive values of the perturbations the STD shows little variation around the annulus. This asymmetric behavior is not predicted by the model and shows either that there are dynamics not captured by the model or nonlinear behavior. For insight into the prestall behavior we decompose the perturbations $\delta\phi(\theta, \tau)$ into a Fourier series with complex harmonics as

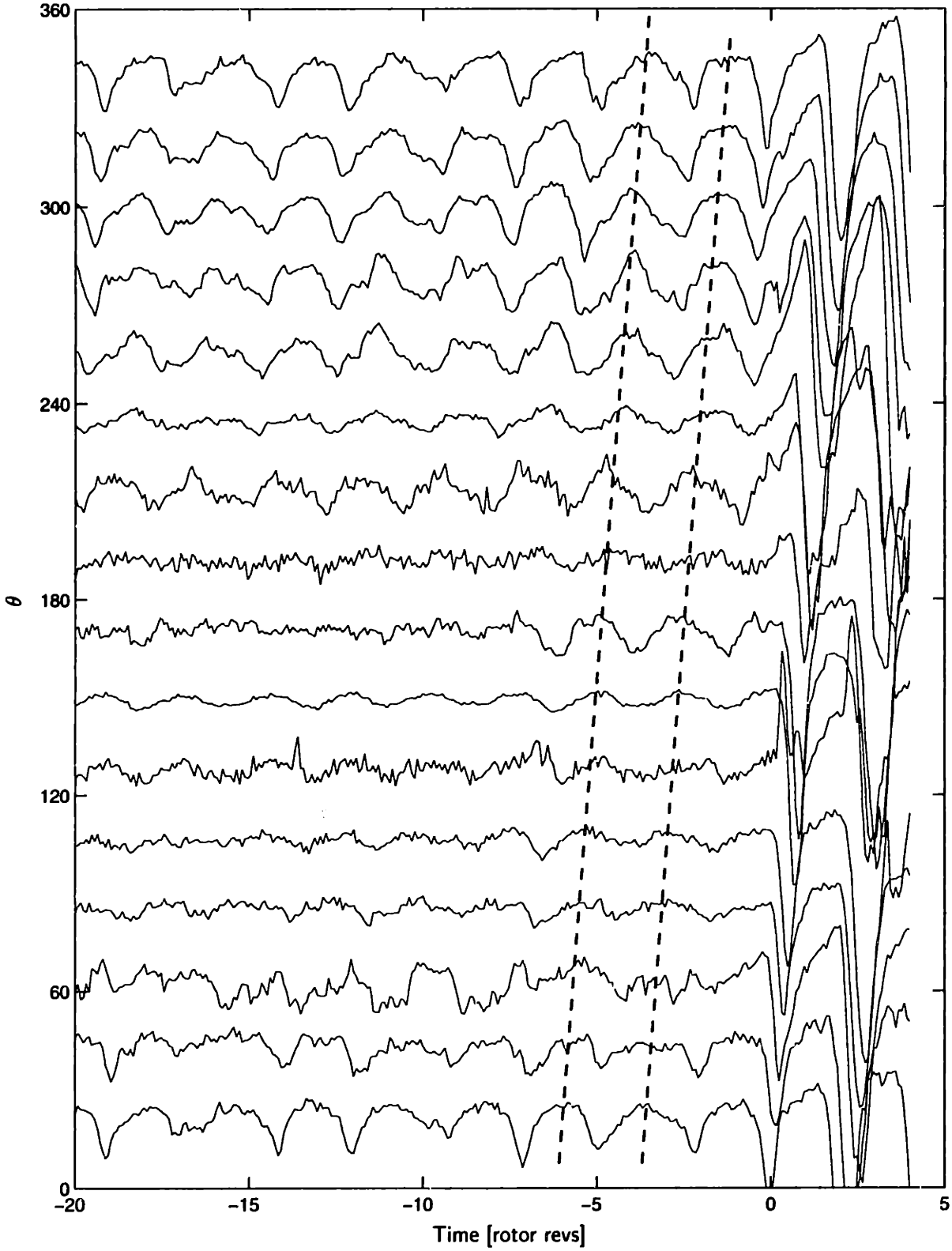

Figure 4.12: Circumferential velocity perturbations prior to stall.

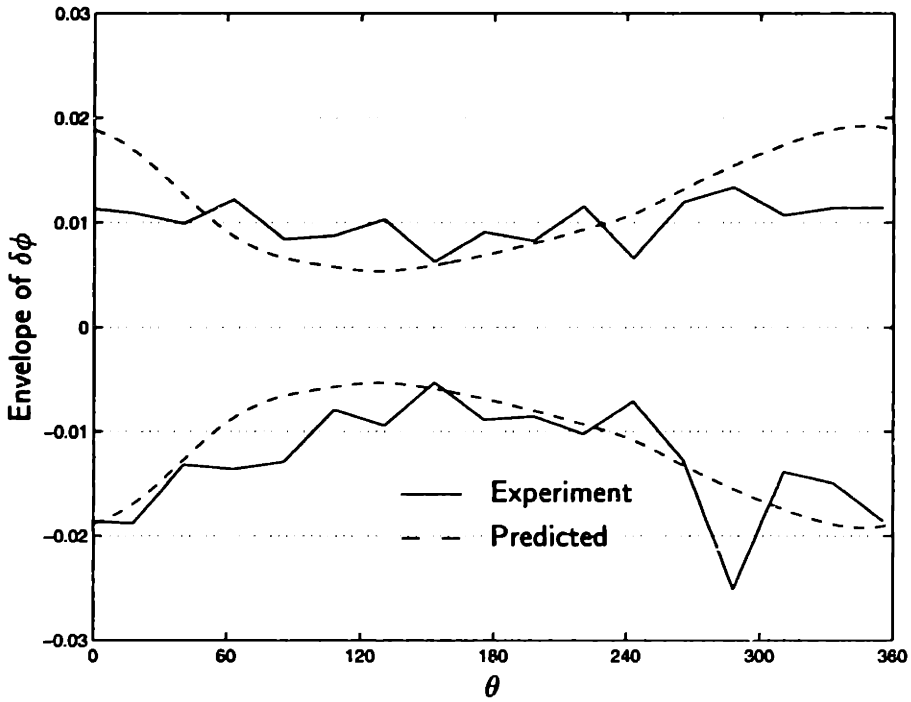

Figure 4.13: Standard deviation of the perturbations around annulus for $\delta\phi > 0$ and $\delta\phi < 0$. The standard deviations obtained from the different hot-wires were connected by straight lines to show the trend.

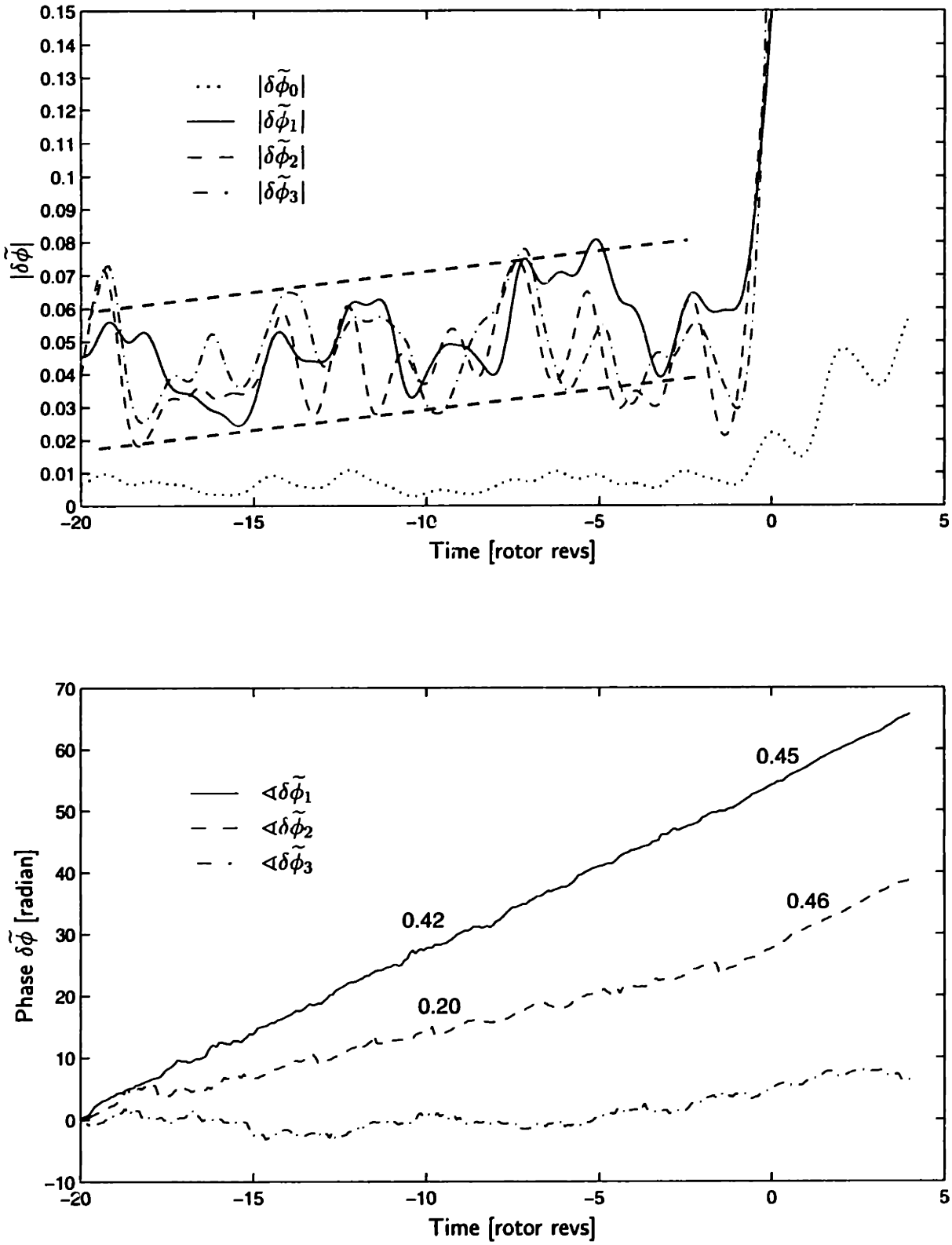

Figure 4.14: Magnitudes (top) and corresponding phases (bottom) of the harmonics $\delta\tilde{\phi}$. The magnitudes shown are as seen by the compressor.

discussed in Section 3.5. The nth harmonic is indicated by $\delta\widetilde{\phi}_n(\tau)$. The magnitudes of the zeroth, first, second, and third harmonics are shown in the graph at the top of Figure 4.14. The nth harmonic has been scaled by $e^{+n|x_m|}$ so the magnitudes shown are those seen by the compressor. In this figure we see that the magnitudes of the higher harmonics increase gradually from $|\delta\widetilde{\phi}_n| \approx 0.035$ for approximately 20 rotor revolutions prior to stall.

The unwrapped phases of the harmonics are also shown in Figure 4.14 where the travelling of the first harmonic at $0.43\,\omega_r$ is clearly visible. The phase of the second harmonic is more erratic but shows a definitive trend; the corresponding velocity of $0.20\,\omega_r$ is slightly lower than $0.43/2 = 0.215$. The phase speeds prior to stall were computed with least squares fits over the range $-15 < \tau < -5$. Poorer estimates for the higher harmonics must be expected because the higher harmonics decay exponentially and thus have lower SNRs. Phase unwrapping is sensitive to noise and so the velocities obtained from the phases should be considered rough estimates. Even so, the velocities for the first and second harmonics agree well with the predicted values of $0.38\,\omega_r$ and $0.19\,\omega_r$ respectively.

4.2.2 Spectral Analysis

The power density spectrum (PSD) is a powerful tool for analyzing the behavior of the system. The PSDs used here were computed using Welch's method [36] with a Hanning window.

Figure 4.15 show the PSDs of the complex harmonics $\delta\widetilde{\phi}_0$–$\delta\widetilde{\phi}_3$. Except for the third harmonic the first mode shows up strongly at $\omega_1 = 0.44\,\omega_r$ in the PSDs indicating there is a wave travelling around the annulus at 44% of the rotor speed. The travelling wave and peak in the PSDs of the harmonics are predicted by the model (see Equations (4.8) and (4.9)) and shows the strong coupling between the different harmonics, including the zeroth. The

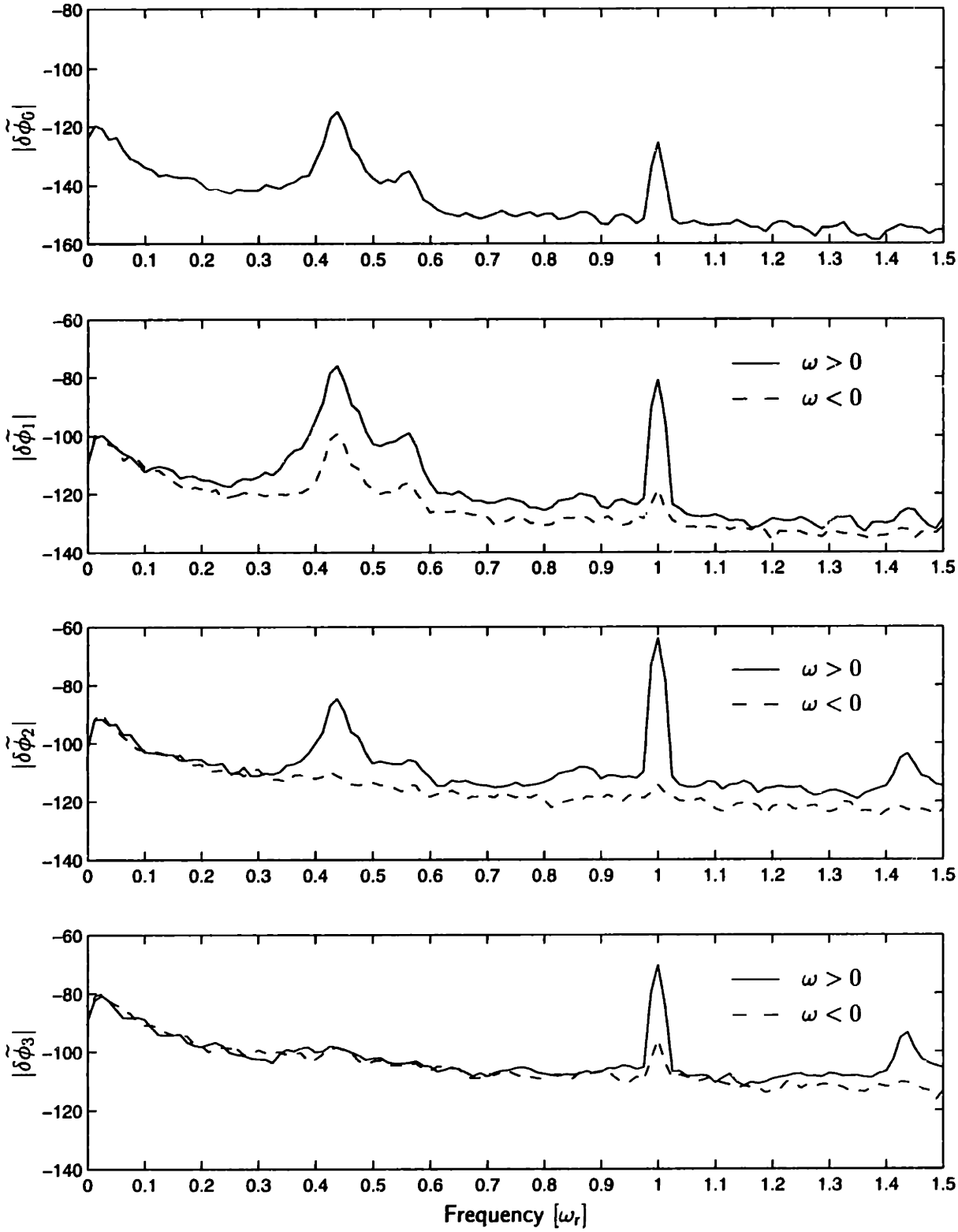

Figure 4.15: PSDs of $\delta\tilde{\phi}_0$, $\delta\tilde{\phi}_1$, $\delta\tilde{\phi}_2$, and $\delta\tilde{\phi}_3$. The PSDs at positive and negative frequencies are shown by the solid and dashed lines respectively, 1.9 dynamic head distortion.

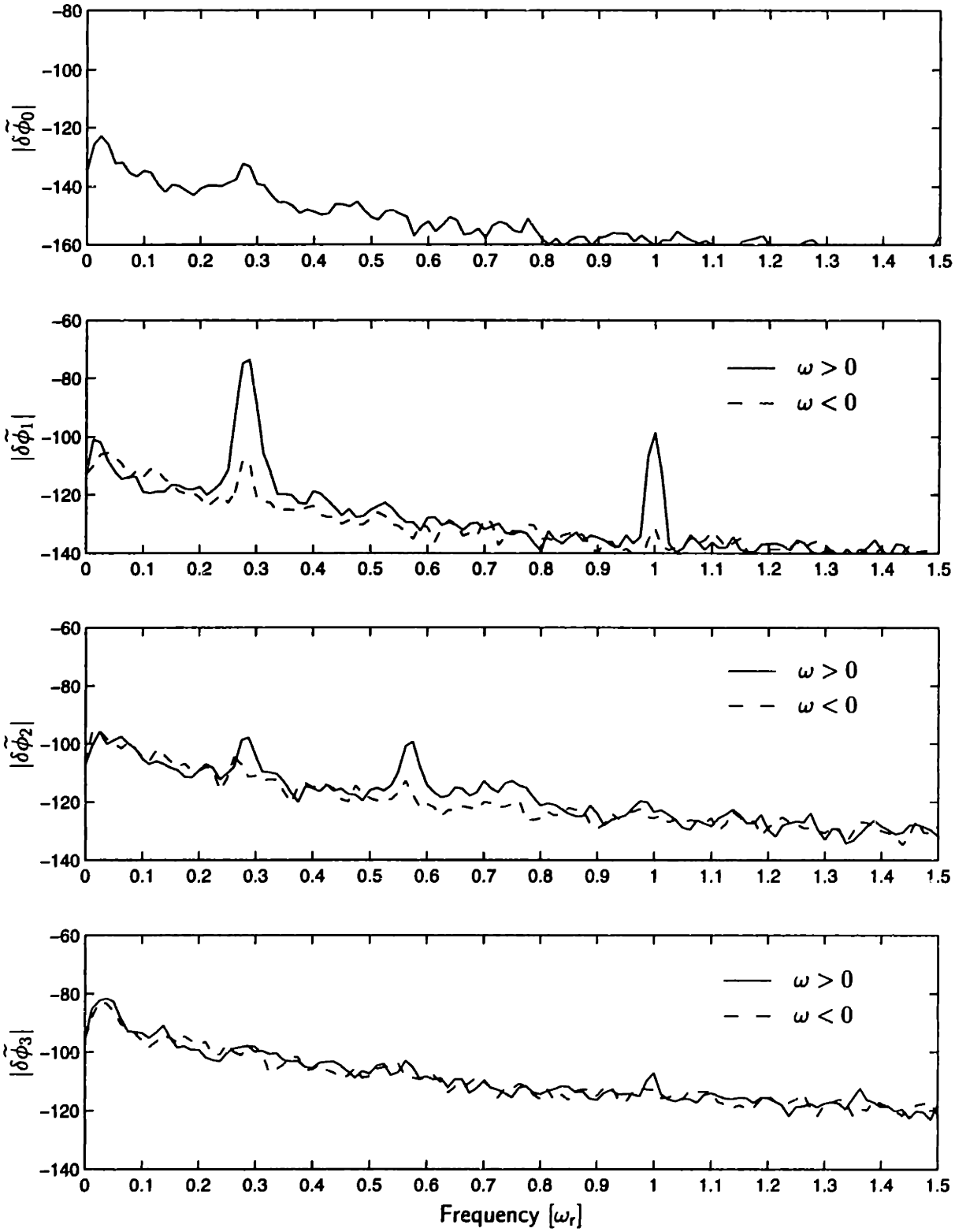

Figure 4.16: Uniform flow PSDs of $\delta\tilde{\phi}_0$, $\delta\tilde{\phi}_1$, $\delta\tilde{\phi}_2$, and $\delta\tilde{\phi}_3$. The PSDs at positive and negative frequencies are shown by the solid and dashed lines respectively.

coupling results from the nonuniform steady flow and does not occur with uniform mean flow; for uniform only the nth harmonic is present in the nth mode. The PSDs for uniform flow are shown in Figure 4.16. The first mode at $0.28\omega_r$ is clearly visible in the PSD for $\delta\tilde{\phi}_1$ and is barely visible in the PSDs of the other harmonics.

A comparison of the noise floors for distorted flow (Figure 4.15) with the corresponding uniform flow (Figure 4.16) shows that the magnitude of the noise is bigger for distorted flow. If the peak at $1\omega_r$ is excluded from the calculations, the distorted flow SNR for the zeroth, first, and second harmonics are 0.34(−9.4 dB), 0.63(−4 dB), and 0.29(−10 dB) respectively. The SNR for the first harmonic for uniform flow is 1.25(1.9 dB) that is better than the corresponding distorted case. The reason for the lower SNR when distortion is present is not known. The PSDs were computed over a period of 2400 rotor revolutions prior to stall. Directly prior to stall the magnitudes of the perturbations tend to increase so that the SNR improves and it becomes possible to distinguish the signal from the noise without additional signal processing as we have seen in Figure 4.12.

In Figure 4.15 we also see a large peak at exactly $1\omega_r$. Comparison with the uniform flow PSDs in Figure 4.15 shows that the $1\omega_r$ peak increased by approximately 20, 10, 40, and 30 dB for the zeroth to third harmonics respectively when distortion was added. It thus appears that this disturbance is related to circumferential nonuniform flow. We note that the PSDs also have peaks at 2 and $3\omega_r$ which are not shown.

In Figure 4.15 we also see peaks at $0.56\omega_r$ in the graphs for $\delta\tilde{\phi}_0$, $\delta\tilde{\phi}_1$, and $\delta\tilde{\phi}_2$ and at $1.44\omega_r$ for $\delta\tilde{\phi}_1$, $\delta\tilde{\phi}_2$, and $\delta\tilde{\phi}_3$. The frequencies $0.56\omega_r$ and $1.44\omega_r$ are exactly $\omega_r \pm \omega_1$ and shows coupling between the first mode and the disturbance at one rotor revolution. This coupling has the form of modulation (or multiplication) in the time domain, resulting in a sum and difference frequency in the frequency domain. The origin of the one rotor revolution mode and modulation is not known.

We also note that the PSDs at negative frequencies (shown in dashed lines) differ from those at the corresponding positive frequencies. Generally there is very little activity at negative frequencies.

4.3 Process Noise Model

In the previous section we saw that there was substantial noise present in the compression system. Two external disturbances forcing the system, $\delta p_t^{(1)}$ (far upstream) and $\delta p_s^{(5)}$ (at throttle exit), were included in the model (see Chapter 3) as process noise. These noise sources, however, do not describe the noise seen in the measurements.

Figure 4.17 shows the analytical and measured PSD of the first harmonic with $\delta p_t^{(1)}$ as the process noise for the 1.9 dynamic head distortion. A logarithmic frequency axis was chosen to show the trend. Except for the first mode peak, the magnitude of the PSD has a slope of 20 dB/decade as indicated by the dashed line. The analytical PSD has a constant slope at frequencies below $0.1\,\omega_r$ and rolls off very fast for frequencies above that of the first mode. For the analytical PSD it was assumed the noise $\delta p_t^{(1)}$ is white.

The 20 dB/decade slope suggests that the integral of white noise must be used as process noise. However, this will not give a slope of 20 dB/decade, but 40 dB/decade because the square of the magnitude of the transfer function is used in the computation of the PSD. The only way to obtain a 20 dB/decade slope at low frequencies is to assume that the PSD of the noise has a $1/\omega$ slope. If this is the case the discrepancy between the measured and analytical PSDs at frequencies above that of the first mode will be larger.

It may be possible that the noise seen at low frequencies is due to process noise while that at frequencies above ω_1 is measurement noise (not included in the model). Both these noises will have to have $1/\omega$ slope. Whether this explanation holds is not known.

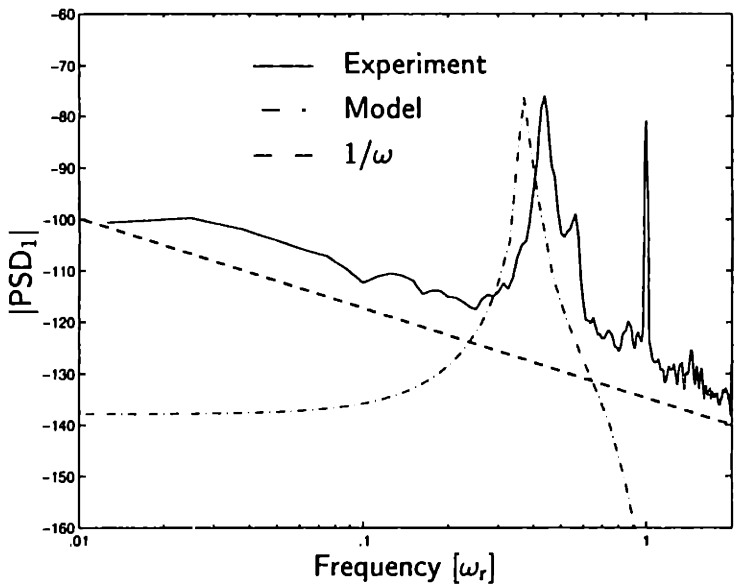

Figure 4.17: Experimental and analytical PSDs, 1.9 dynamic head distortion.

Similar results hold for the other harmonics and process noise $p_s^{(6)}$ and, in summary, the process noise can at most be in part responsible for the noise seen in the measured PSDs.

4.4 Transfer Functions

The state space description and corresponding time domain analysis is one way of looking at signals. An alternative way of looking at the system is in the frequency domain. Let the state space description be given by

$$\delta\dot{\boldsymbol{x}} = A\delta\boldsymbol{x} + B\delta\tilde{\gamma} \tag{4.10}$$

$$\delta\tilde{\boldsymbol{\phi}} = C\delta\boldsymbol{x} + D\delta\tilde{\gamma}. \tag{4.11}$$

We assume that the dependence on $\delta\dot{\gamma}$ has already been accounted for; see discussion on page 59. Taking the Laplace transforms of these equations and substituting the first

equation into the second we obtain

$$\delta\widetilde{\phi}(i\omega) = [C(i\omega I - A)^{-1}B + D]\,\delta\widetilde{\gamma}(i\omega) \tag{4.12}$$

$$= [CV(i\omega I - \Lambda)^{-1}V^{-1}B + D]\,\delta\widetilde{\gamma}(i\omega) \qquad \text{(from Equation (4.3))} \tag{4.13}$$

$$\triangleq G(i\omega)\,\delta\widetilde{\gamma}(i\omega). \tag{4.14}$$

The matrix $G(i\omega)$ is known as the transfer function matrix. The transfer function can be written in terms of the eigenvalues Λ and the eigenvectors (or mode shapes) V. Therefore, if there is good match between the predicted and measured transfer functions we can conclude there is good match between the predicted and measured mode shapes.

The method used for measuring the transfer function is discussed in Appendix C.2. In that appendix we also discuss the excellent noise rejection and robustness against nonlinearities of the measuring technique, with the conclusion that examination of transfer functions is the most reliable way to determine the accuracy of the model.

All the transfer functions shown will be for complex inputs and complex outputs as discussed in Section 3.5 and Appendix C.1.

We will show transfer functions from the first three harmonics of $\delta\gamma$ to the first three harmonics of $\delta\phi$ so that G is a square matrix

$$G = \begin{pmatrix} g_{00} & g_{01} & g_{02} & g_{03} \\ g_{10} & g_{11} & g_{12} & g_{13} \\ g_{20} & g_{21} & g_{22} & g_{23} \\ g_{30} & g_{31} & g_{32} & g_{33} \end{pmatrix} \tag{4.15}$$

$$g_{pq} = |g_{pq}|e^{i\arg(g_{pq})}, \quad p,q = 0,1,2,3.$$

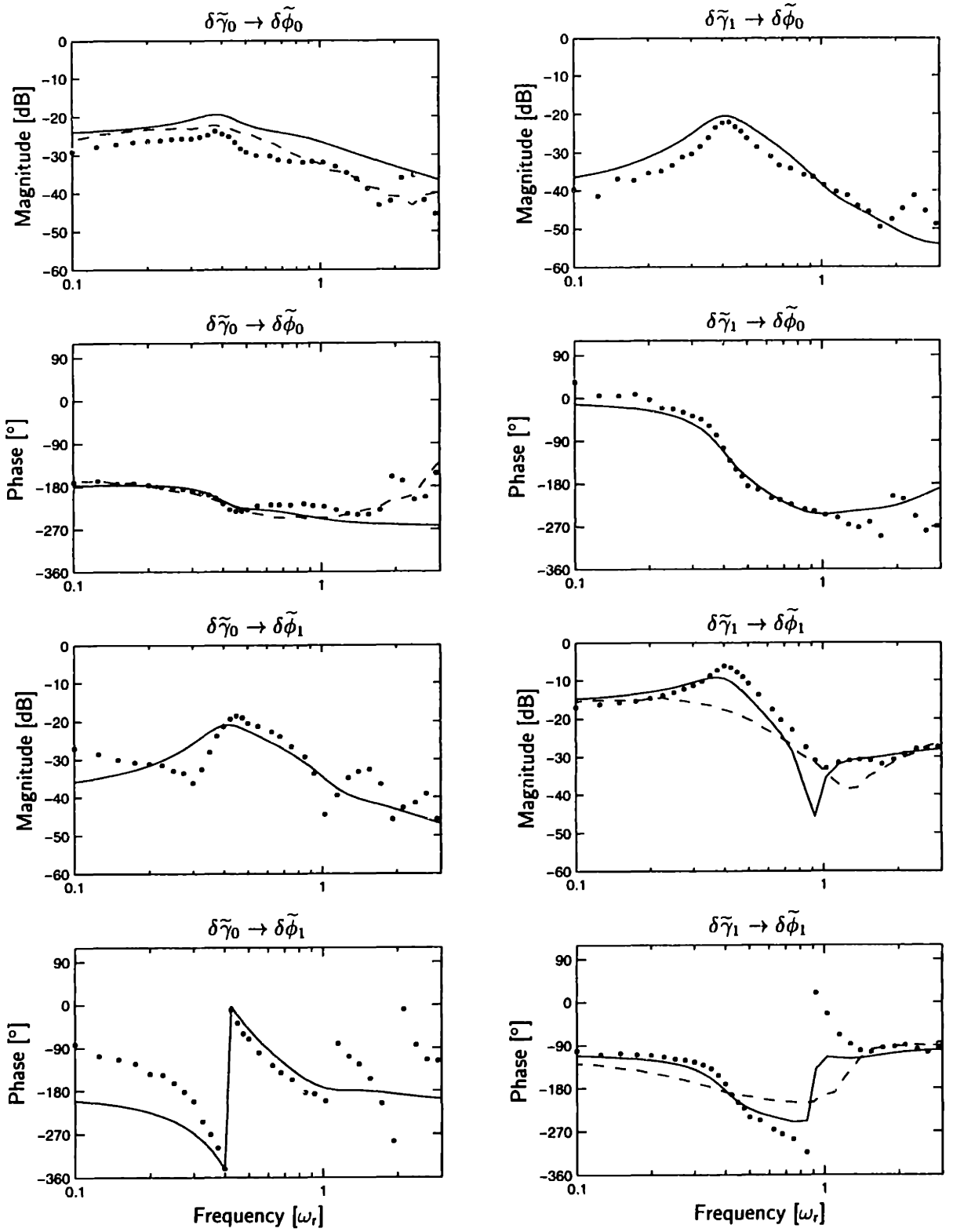

Figure 4.18: Transfer functions $\phi = 0.500$, 1.9 dynamic head distortion. Solid line=predicted, dots=experiment, dashed line=uniform flow experiment.

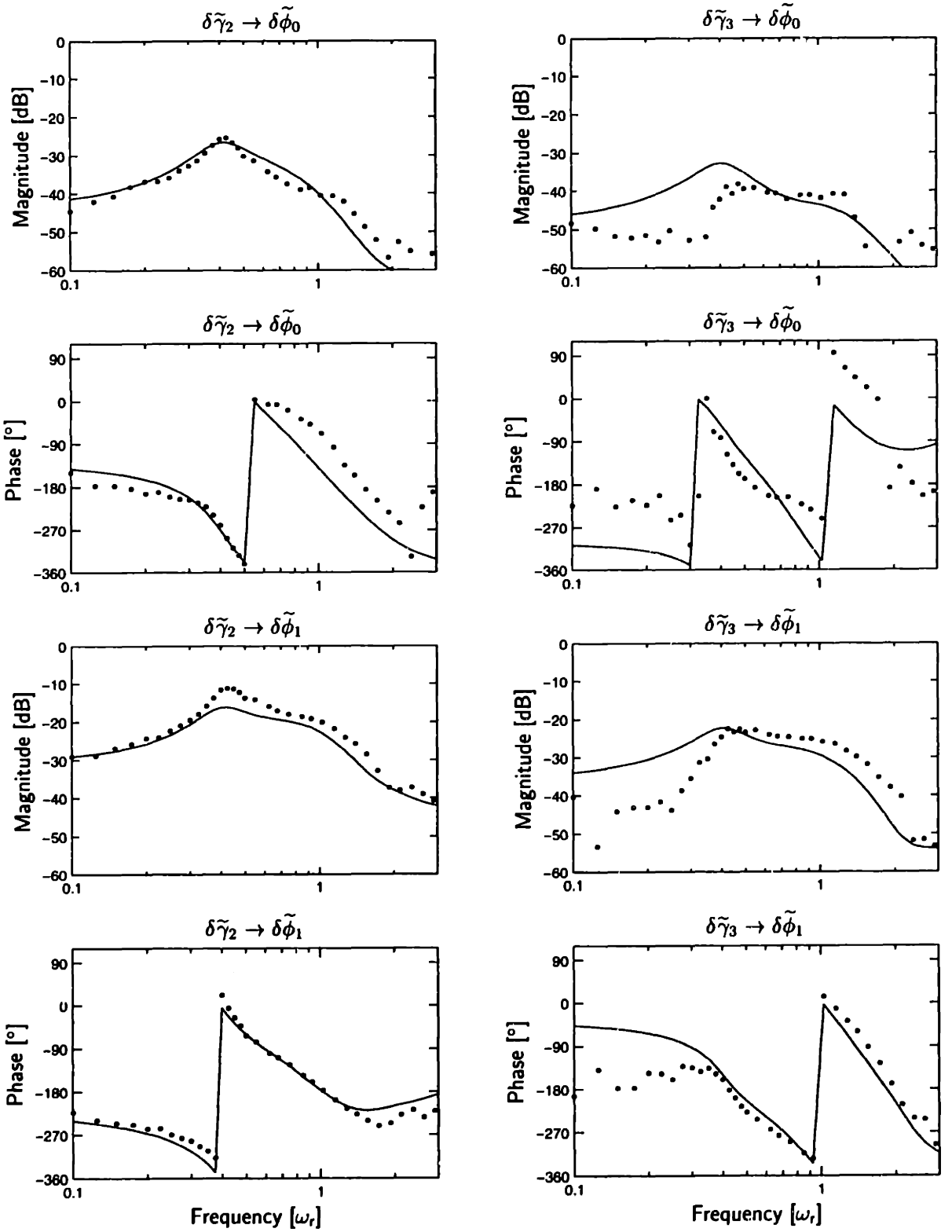

Figure 4.19: Transfer functions $\phi = 0.500$, 1.9 dynamic head distortion. Solid line=predicted, dots=experiment, dashed line=uniform flow experiment.

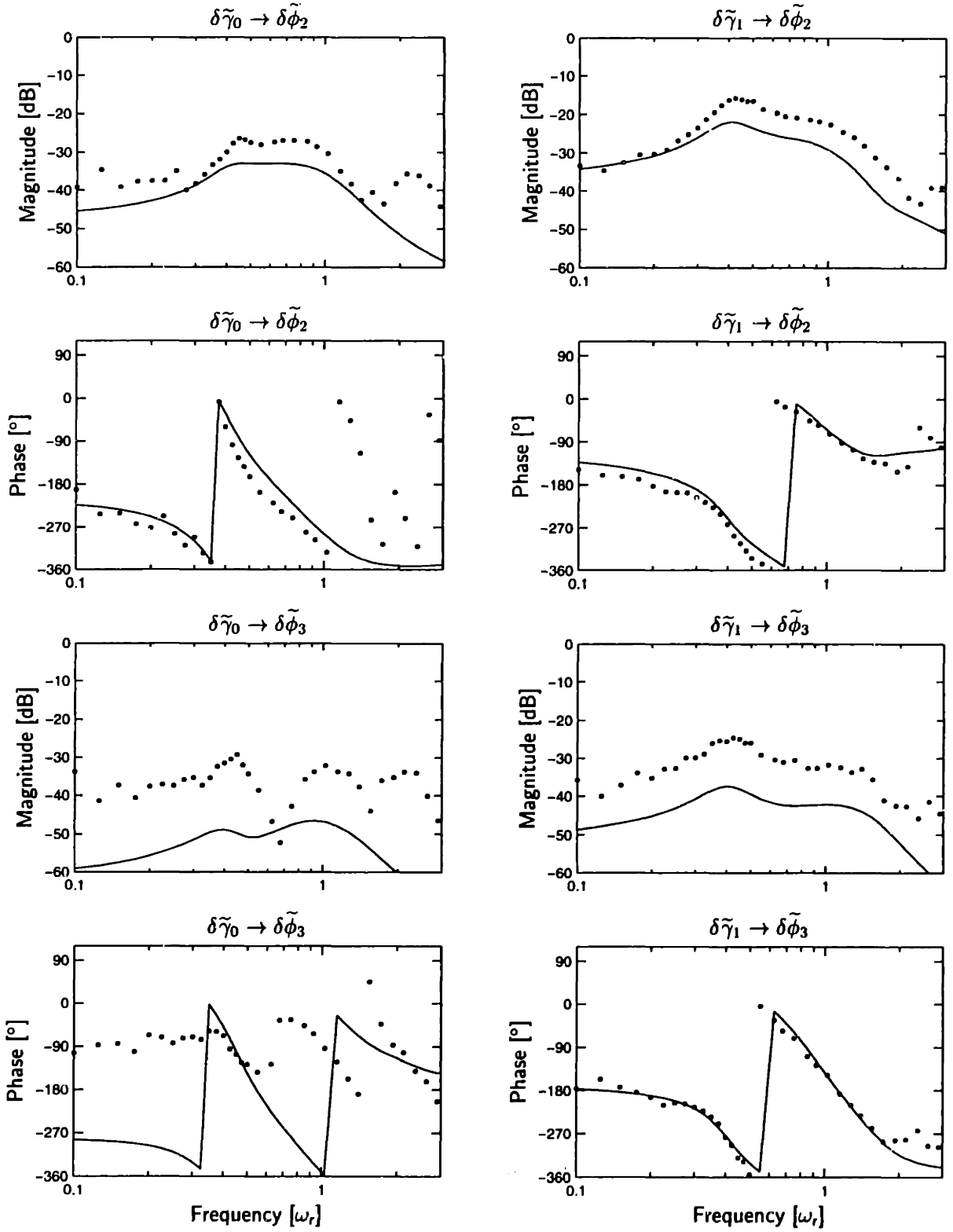

Figure 4.20: Transfer functions $\phi = 0.500$, 1.9 dynamic head distortion. Solid line=predicted, dots=experiment, dashed line=uniform flow experiment.

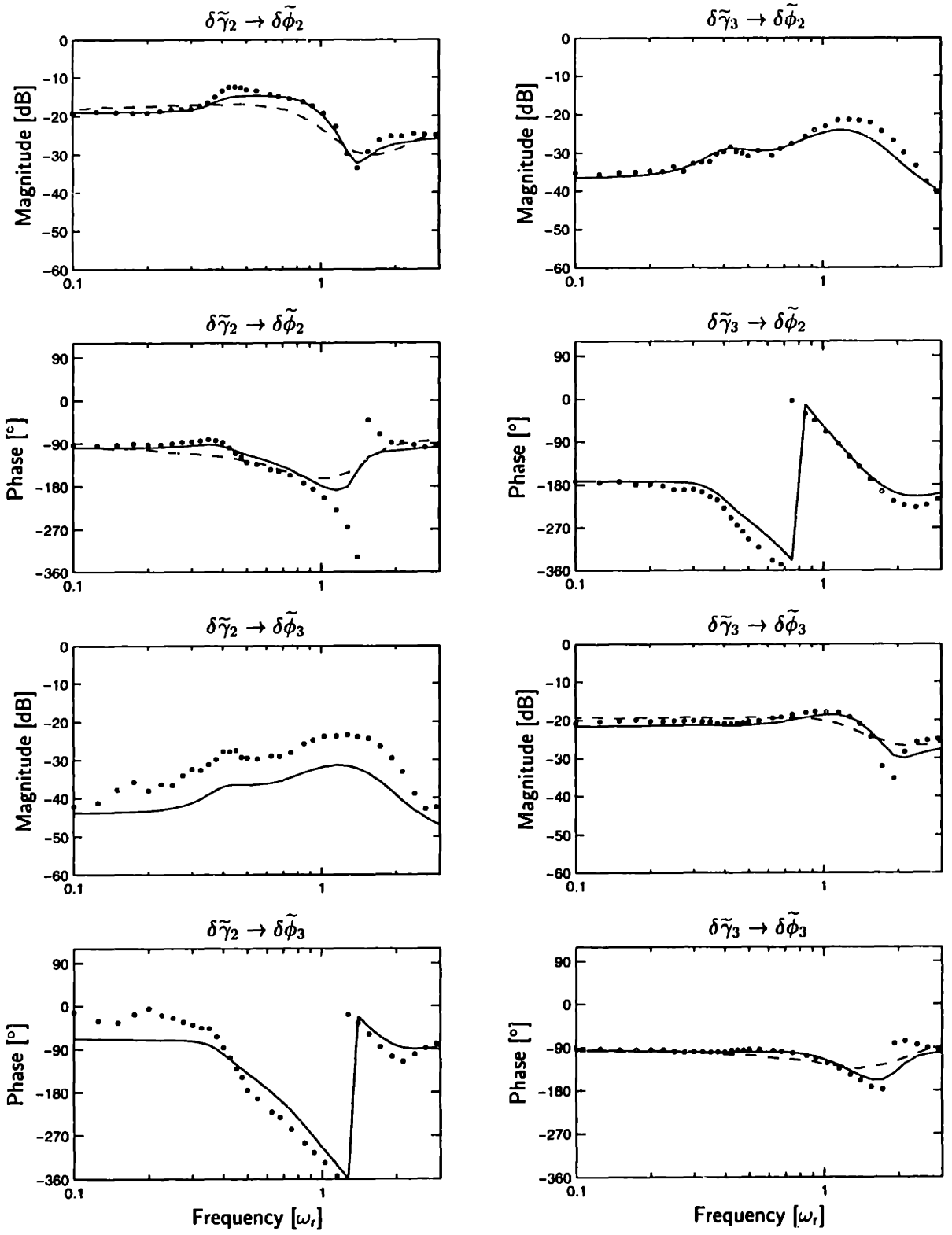

Figure 4.21: Transfer functions $\phi = 0.500$, 1.9 dynamic head distortion. Solid line=predicted, dots=experiment, dashed line=uniform flow experiment.

Figures 4.18 – 4.21 show the set of transfer functions for the 1.9 dynamic head distortion at $\widetilde{\phi}_{so} = 0.500$. This is approximately 17% above the stalling flow coefficient so that we expect the system to exhibit behavior that is well damped. In these figures the transfer function g_{pq} from $\delta\widetilde{\gamma}_q$ to $\delta\widetilde{\phi}_p$ is indicated by $\delta\widetilde{\gamma}_q \rightarrow \delta\widetilde{\phi}_p$. Four transfer functions are shown on each page. The magnitude of each transfer function is shown with the corresponding phase directly below it. The transfer functions along the diagonal of G also include the measured uniform flow transfer functions (shown with dashed lines); for uniform flow all off-diagonal transfer functions are zero.

The first harmonic has a strong presence in the first mode so we will concentrate the discussion on the transfer functions to and from the first harmonic. Peaks in the transfer function magnitudes indicate lightly damped modes at which the system will tend to resonate. For example, the measured transfer function from $\delta\widetilde{\gamma}_1 \rightarrow \delta\widetilde{\phi}_1$ at the bottom right hand corner of Figure 4.18 has a small peak at approximately $0.38\,\omega_r$ while the predicted peak is at $0.40\,\omega_r$. The model thus predicted the frequency of the first mode with an error of only $0.02\,\omega_r$, that is, to within 2% of the rotor frequency.

The peak at $\omega_1 = 0.38\,\omega_r$ is also visible in the magnitudes of the transfer functions g_{00} and g_{22} indicating that these harmonics are also present in the first mode. The smaller peaks in g_{00} and g_{22} can be explained by looking at the predicted pole-zero maps of the individual transfer functions shown in Figure 4.22.

For g_{00} we see that there is a zero close to the first mode pole so the transfer function magnitude will not show a large peak in the corresponding frequency range. For g_{22} there is an almost exact pole-zero cancellation, while g_{33} has an exact pole-zero cancellation with no peak in the transfer function magnitude. We also see in these pole-zero maps that the poles at negative frequencies are cancelled, or almost cancelled, by zeros and thus the transfer functions at negative frequencies do not have any large resonant peaks and are therefore not

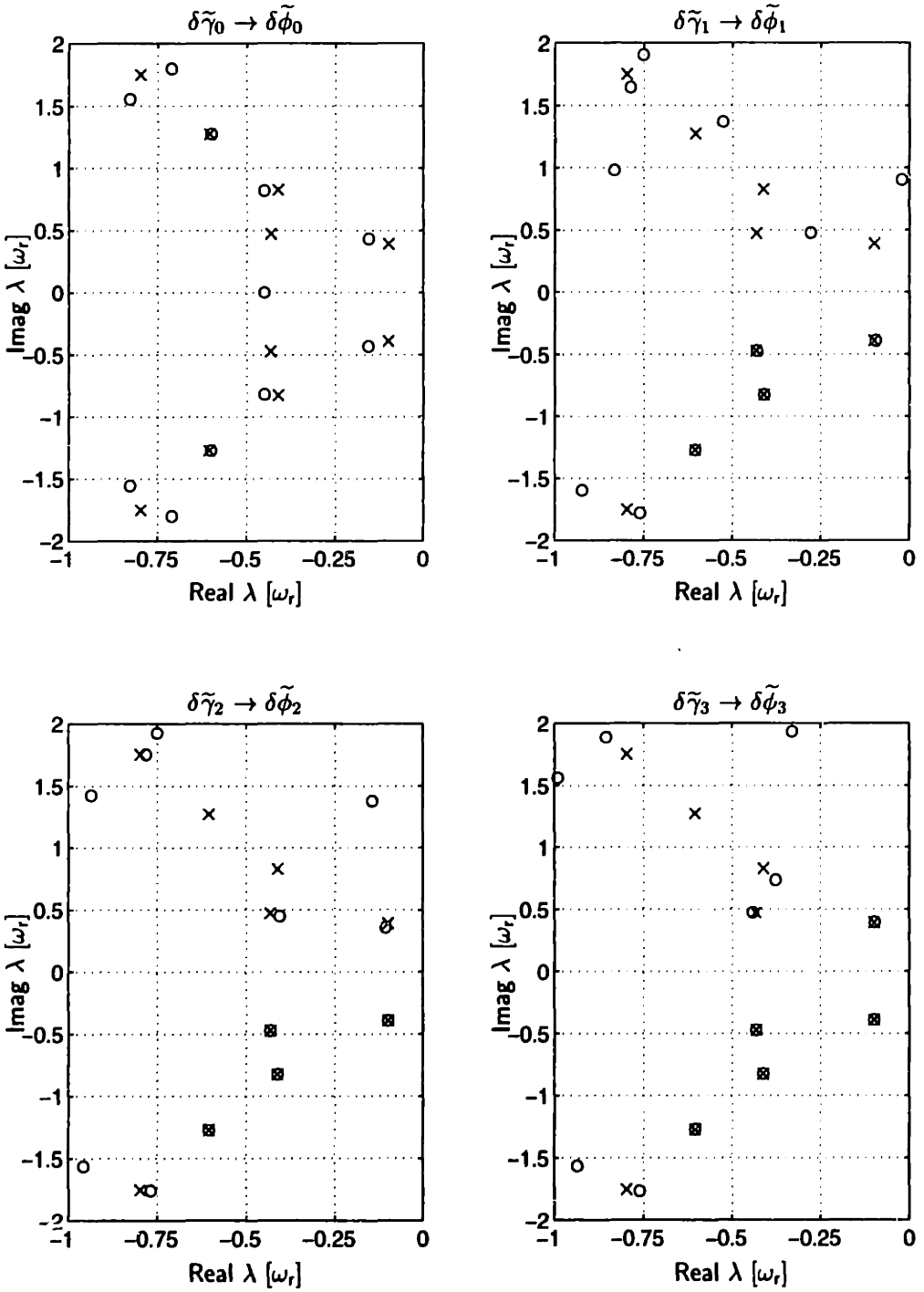

Figure 4.22: Pole-zero maps of $g_{jj}, j = 0, 1, 2, 3$. $\phi = 0.500$, 1.9 dynamic head distortion. x=poles, o=zeros

shown. The lack of strong resonance at negative frequencies was also visible in the PSDs showed earlier on, see Figure 4.15.

Because of the low SNR, transfer functions with magnitudes below approximately -40 dB will not be very accurate.

Comparing the uniform and distorted flow transfer functions g_{00}, g_{11}, g_{22}, and g_{33} we see that, except for g_{11}, the addition of distortion did not change these transfer functions significantly. The magnitude of g_{11} for distorted flow is 10 dB larger than the corresponding uniform flow transfer function, indicating that the eigenvalue of the dominant mode has moved closer to the $i\omega-$axis, that is, distortion has a destabilizing effect.

Valleys in the transfer functions indicate zeros close to the $i\omega-$axis. Again this is visible in the transfer function g_{11}. In this case it appears from the magnitude of g_{11} that the predicted frequency of the zero is lower than the measured frequency. The minimum values of the measured and predicted transfer function magnitudes are at $0.93\,\omega_r$ and $1.03\,\omega_r$ respectively, an error of $0.1\,\omega_r$. The measured and predicted phases of g_{11} changes abruptly to within $0.05\,\omega_r$, and we conclude that the frequency of the zero is predicted accurately by the model.

The predicted zero is minimum phase, that is, the real part of the zero is negative (see Figure 4.22) so that the phase increases for frequencies close to that of the zero frequency, while the measured zero is nonminimum phase (real part of the zero is positive) with a corresponding decrease in the phase. At this flow coefficient the zero is very close to the $i\omega-$axis as is evident by the abrupt change in both the measured and predicted phase. The predicted and measured zero are just to the left and right of the $i\omega-$axis respectively so that the absolute distance between the zeros is small.

The magnitudes of the transfer functions g_{01}, g_{10}, g_{12}, and g_{21} are in the range -30 dB

to -20 dB for frequencies close to that of the first mode, while the magnitude of g_{11} is approximately -10 dB at the same frequencies, indicating strong coupling between the zeroth, first, and second harmonics. Except for the transfer function from the zeroth to the first harmonic there is good agreement between the magnitudes and phases of the predicted and measured transfer functions. The transfer function from the zeroth to the first harmonic appears to have additional zeros not predicted by the model; however, the general trend of the magnitude and phase still follows the measured transfer function well up to $1\,\omega_r$. In general it was found that transfer functions from the zeroth harmonic to the higher harmonics were not predicted as well as the other transfer functions; however, the main trend was always captured well.

We also note in these figures that transfer functions g_{pq} for which $|p-q| \leq 1$ are predicted better than transfer functions for which $|p-q| > 1$. This trend can be explained by the fact that the higher harmonics decay like $e^{n x_m}$ so that the SNR is smaller for higher harmonics and it is more difficult to measure these transfer functions accurately. In addition, for higher harmonics the approximation that the 12 AGVs are a continuum also becomes poorer. This too will decrease the fidelity of the measured transfer functions.

To determine if the model captures the change in dynamic behavior of the compression system at different flow coefficients, transfer functions were measured at three different operating points. A subset of this data is shown in Figures 4.23 - 4.26. The graphs at the top, middle, and bottom show the magnitude (left) and phase (right) at $\phi_{stall} + 17\%$, $\phi_{stall} + 7\%$, and $\phi_{stall} - 0.4\%$ respectively. In general the trend was captured well by the model.

At the lowest flow coefficient the frequency of the first mode is under predicted by approximately $0.1\,\omega_r$. There are two possible reasons for this discrepancy. First, at $\phi_{stall} - 0.4\%$ the steady flow spans the range $0.36 \leq \phi_s \leq 0.55$. The characteristic has been measured

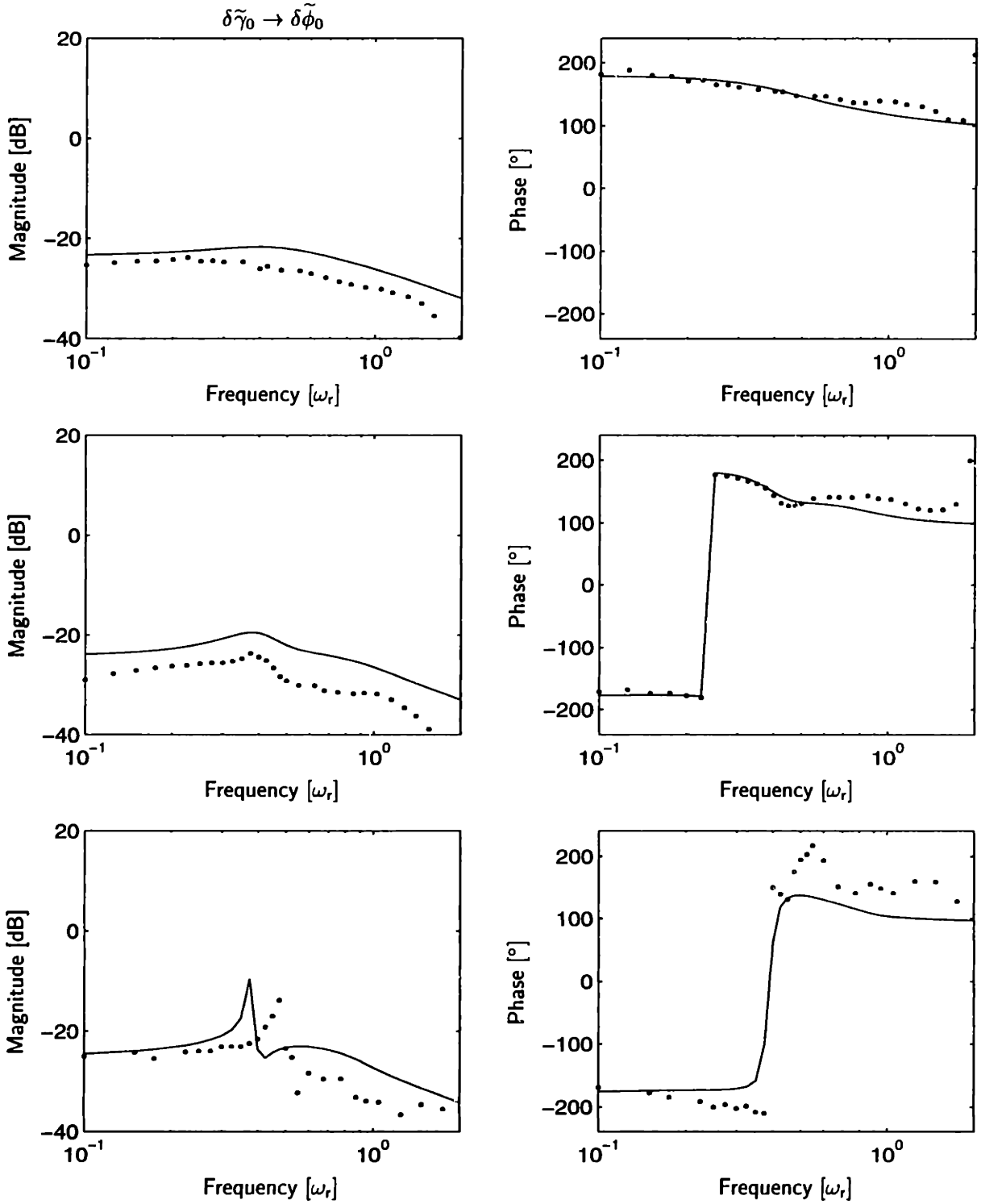

Figure 4.23: Magnitudes (left) and phase (right) of transfer functions from $\delta\tilde{\gamma}_0$ to $\delta\tilde{\phi}_0$ at $\phi_{\text{stall}} + 17\%$ (top), $\phi_{\text{stall}} + 7\%$ (middle), and $\phi_{\text{stall}} - 0.4\%$ (bottom), 1.9 dynamic head distortion. Solid line=predicted, dots=experiment.

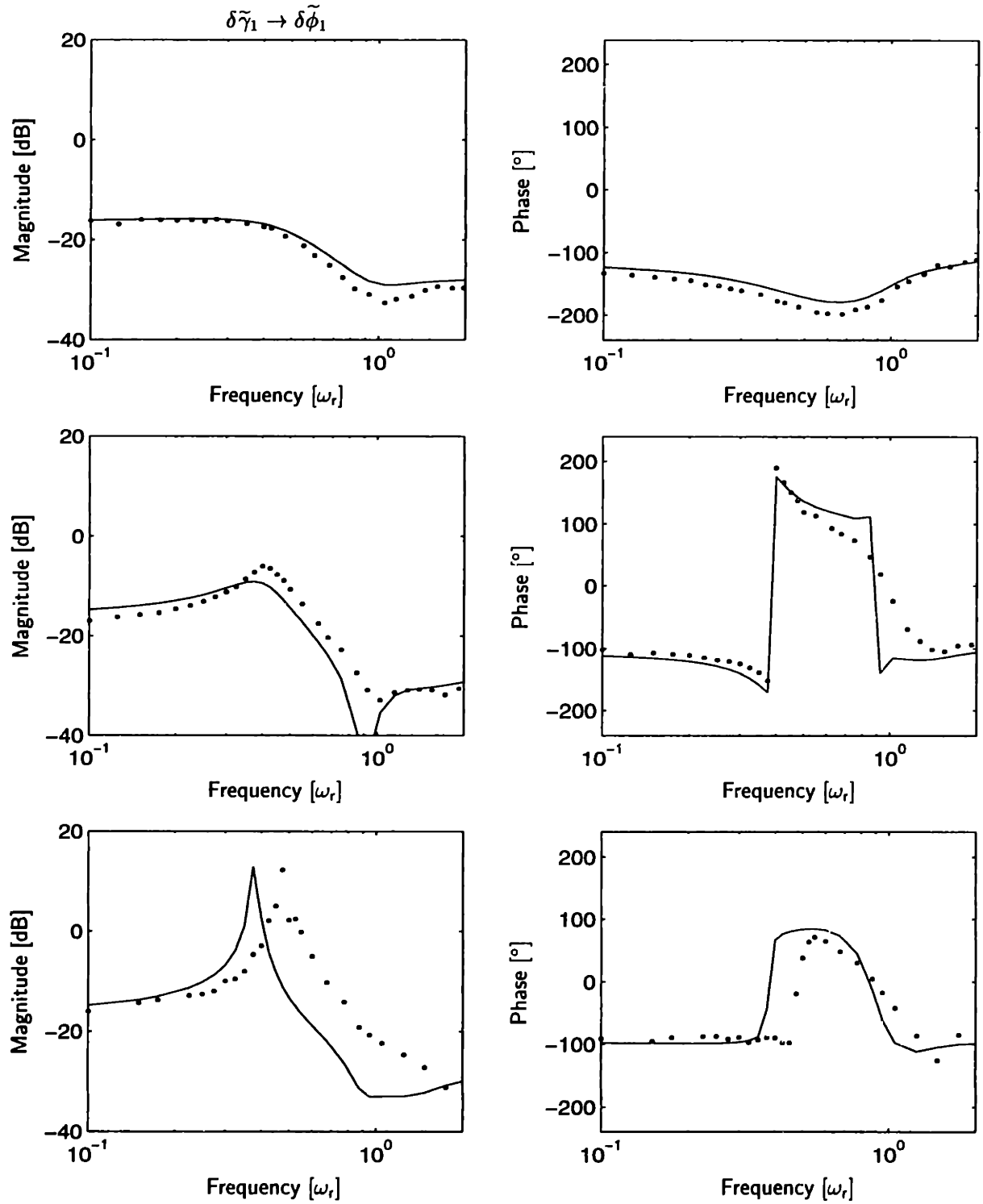

Figure 4.24: Magnitudes (left) and phase (right) of transfer functions from $\delta\tilde{\gamma}_1$ to $\delta\tilde{\phi}_1$ at $\phi_{\text{stall}} + 17\%$ (top), $\phi_{\text{stall}} + 7\%$ (middle), and $\phi_{\text{stall}} - 0.4\%$ (bottom), 1.9 dynamic head distortion. Solid line=predicted, dots=experiment.

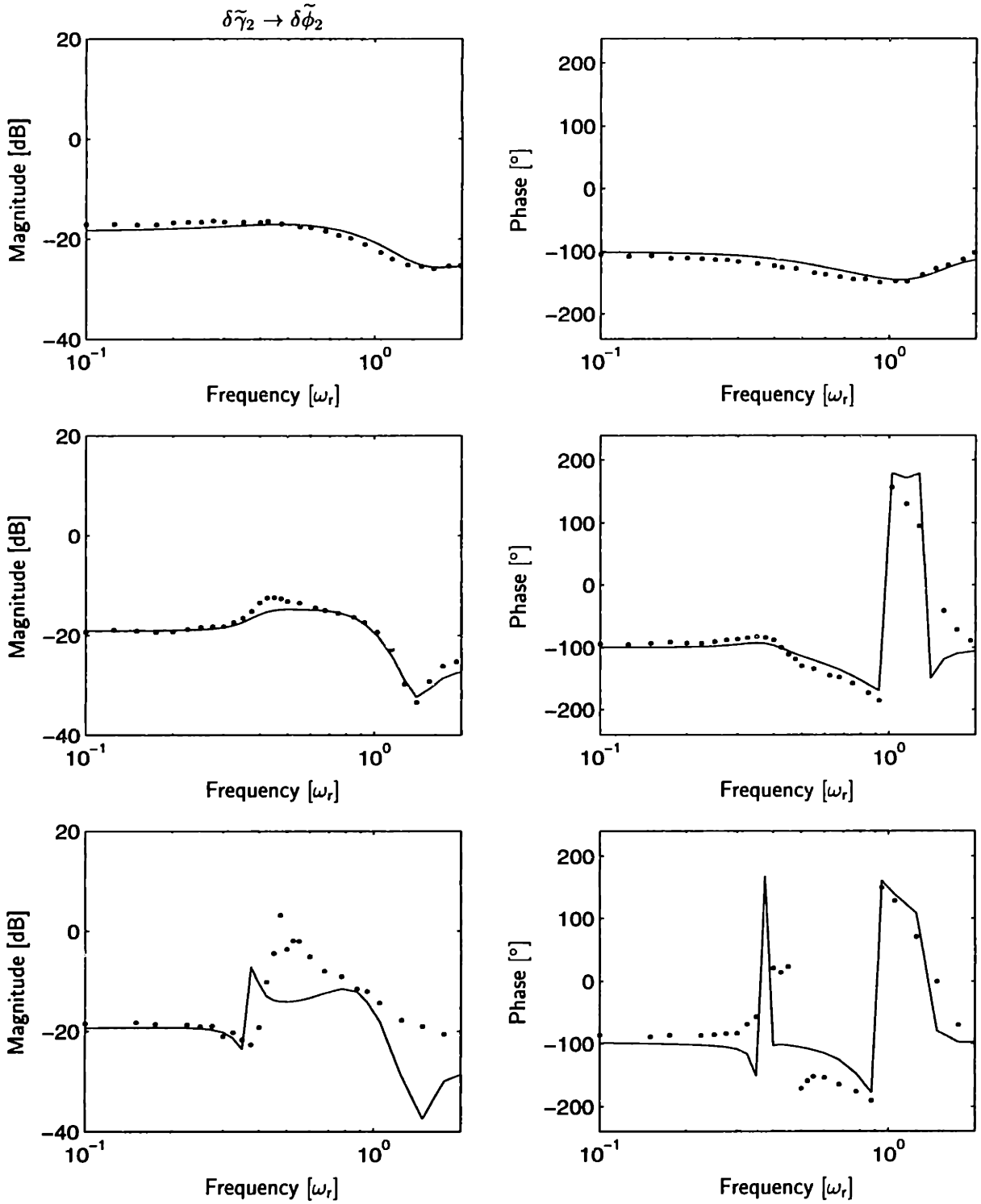

Figure 4.25: Magnitudes (left) and phase (right) of transfer functions from $\delta\widetilde{\gamma}_2$ to $\delta\widetilde{\phi}_2$ at $\phi_{\text{stall}} + 17\%$ (top), $\phi_{\text{stall}} + 7\%$ (middle), and $\phi_{\text{stall}} - 0.4\%$ (bottom), 1.9 dynamic head distortion. Solid line=predicted, dots=experiment.

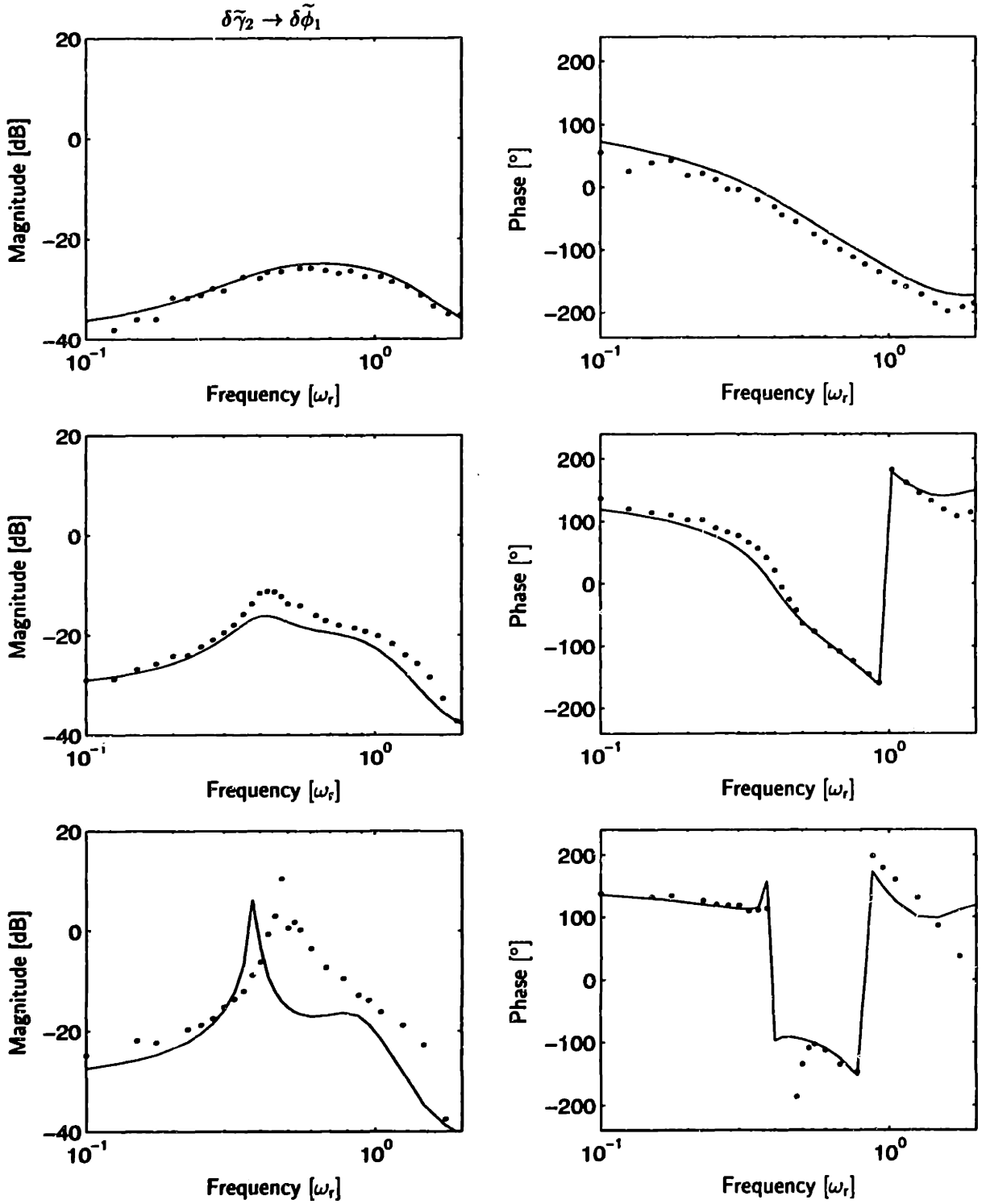

Figure 4.26: Magnitudes (left) and phase (right) of transfer functions from $\delta\widetilde{\gamma}_3$ to $\delta\widetilde{\phi}_3$ at $\phi_{\text{stall}} + 17\%$ (top), $\phi_{\text{stall}} + 7\%$ (middle), and $\phi_{\text{stall}} - 0.4\%$ (bottom), 1.9 dynamic head distortion. Solid line=predicted, dots=experiment.

only for $\phi_s > 0.42$ and thus we are operating on a part of the characteristic that is not known. For the predicted transfer functions shown in the figure it has been assumed that the characteristic for flow coefficients less than 0.42 is parabolic, and the actual slope may be different. Second, when the distortion generator was disassembled after completion of the experiments it was found that the screen was packed with dirt and thus the distortion intensity was higher than the value measured initially. The frequency of the modes increase with increasing distortion intensity, so the dirty screen explains, at least in part, the higher measured frequency of the first mode.

At the lowest flow coefficient shown, $\phi_{stall} - 0.4\%$, the system was open loop unstable so it was necessary to use active control to stabilize the system. Active control will be discussed in Chapter 5.

4.5 Summary

In this chapter we compared the dynamic behavior of small perturbations in both the time and frequency domain. All the major trends are predicted by the model. Analysis of the transfer functions showed the model accurately predicted the frequencies of the most unstable pole and dominant zero to within $0.02\,\omega_r$ and $0.1\,\omega_r$ respectively.

---

5 Active Control

5.1 Introduction

In this chapter we present the first experimental results of active control of rotating stall in the presence of large total pressure inlet distortion. Several questions will be addressed: Will modern controllers, whose designs are based purely on the model, stabilize the system? Are harmonic feedback controllers designed for uniform flow (used by Paduano [37] and Haynes [20]) effective in the presence of distortion? Can the coupling between the different harmonics due to the distortion be used to stabilize the compression system at lower flow coefficients? Does the model predict the range of flow coefficients over which the compressior system can be stabilized?

The figure of merit used to determine the performance of a controller will be the lowest flow coefficient at which the compression system can be stabilized. This is not the only or best measure of performance; other factors like disturbance rejection, sensitivity to noise, and robustness to system uncertainty are of practical importance. Also, the effectiveness of the controller against unknown, time varying distortions and different operating conditions are important for real applications. However, for a given compressor, determining the stalling flow coefficient experimentally is convenient, can be done in a consistent way, and has been used successfully in the past by Paduano [37], Haynes [20], and Gysling [19].

To answer the questions posed earlier four controllers were tested experimentally. We start with a discussion of the different controllers. This is followed by a presentation of the experimental results, an investigation into the loss of stability, and a chapter summary.

5.2 Control Laws

5.2.1 LQG Controller

The first controller is a linear quadratic Gaussian (LQG) controller. LQG controllers are usually used in optimal control applications where a quadratic cost function consisting of weighted sums of the state perturbations and control energy is minimized. For our application the LQG design procedure was not used for its optimal properties but simply because it provides a simple way to design controllers for multi-input multi-output systems. The basic model was used for the design of the LQG controllers. Because the basic model does not include any model of unsteady viscous response the predicted compressor slope is steeper than the effective slope; therefore, the slope of the characteristic at flow coefficients to the left of the peak of the characteristic was decreased until the predicted stalling flow coefficient matched the experimental valued. With this change it was found that the frequency of the first mode was also predicted correctly.

The LQG controllers are designed in two steps. In the first step it is assumed that all the states of the system are available for feedback and a constant gain is found such that a cost function, consisting of a weighted sum of the state and control energy, is minimized. Often all the states are not available for feedback in which case they must be estimated. In the second stage a steady state Kalman filter (or any other observer) is designed to estimate the states given a set of measurements. The design of the Kalman filter requires the specification of process and measurement noise statistics. For the LQG controllers used here it was assumed that both the process and measurement noise are white. The intensity of the process noise was assumed to be the identity matrix, and the intensity of the measurement noise was taken as a constant multiplied by the identity matrix. This constant was used to adjust the bandwidth of the Kalman filter. It was found experimentally that the bandwidth of the Kalman filter had to be in the range of $1\text{–}2\omega_r$ for satisfactory

performance. For larger bandwidths the LQG controllers were very sensitive to noise and destabilized the compressor. The design of the Kalman filter also requires the specification of the cross correlation between the process and measurement noise, and this was taken as zero. This is a crude assumption as there will be correlation between the upstream measurement noise and process noise. However, because the LQG controller was not used for its optimal properties this was deemed acceptable.

It was noted in Section 3.3.3 that approximately $4n$ harmonics were necessary to locate the poles of the first n modes. A complete set of poles and transmission zeros of the compression system at $\phi_{\text{stall}} - 1\%$ is shown in Figure 5.1. The poles and zeros corresponding to the actuator dynamics are not shown though they are included in the design model.

In this model 32 harmonics were used to compute the steady flow, and 16 harmonics were included in the state space description. Also shown in the figure are circles (with centers at the origin) with radii of 2 and $3\omega_r$. There are five modes within the $2\omega_r$ circle; these modes dominate the dynamics at frequencies of practical interest. The other modes are either further into the left half plain, that is, they have fast dynamics so that they can be approximated by constants at low frequencies, or the modes closer to the $i\omega$−axis are close to zeros and will have little resonance. We also note that there are several poles and zeros that almost cancel. This near pole-zero cancellation was also observed at other flow coefficients and distortion magnitudes.

With the full set of modes available the state space model can be reduced so that only the dominant modes are retained. The approach followed here was to convert the state space description into modal form and keep only the modes included in the $3\omega_r$ circle, typically 15 modes. It was found that the additional modes are necessary to capture the dominant zeros. If only the first four or five modes were included the zeros were off by as much as 50%. By keeping all the modes inside the $3\omega_r$ circles the gains and phases were

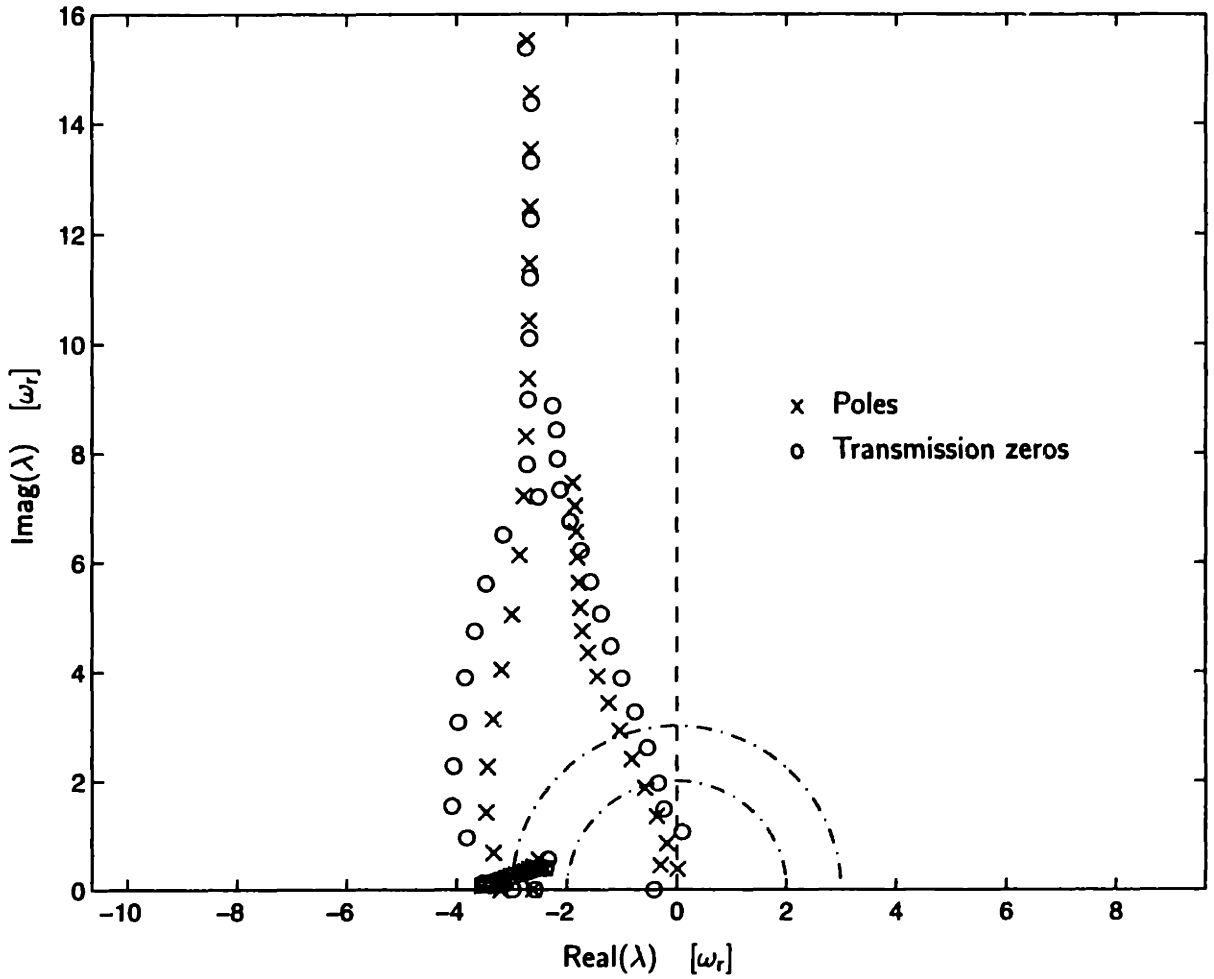

Figure 5.1: Poles and transmission zeros at mass flow $\phi_{\text{stall}} - 1\%$. The two semicircles have radii 2 and $3\omega_r$ respectively.

approximated very well up to $2\omega_r$, the bandwidth of the AGV motors. This reduced order model was then used in the LQG design. The modes of the LQG controller again separated into slow and fast modes so that model reduction was also applied to the controller; the final controllers had between 8 and 10 states. We note that the LQG controller is a dynamic controller while the controllers discussed below are constant gain controllers.

We note that an LQG controller is a full multi-input multi-output dynamic controller,

whereas all the remaining controllers are constant gain (no dynamics) controllers.

5.2.2 Harmonic Feedback

The second controller tested was used by Haynes [20] to control rotating stall with uniform flow on the same compressor. For uniform flow the modes have a one-to-one correspondence with the harmonics and go unstable one at a time. This behavior was used by Haynes [20] to experimentally find a set of independent optimal (in the sense of achieving lowest stalling flow coefficient) single-input single-output controllers for the first three harmonics. Because of the one-to-one correspondence between modes and harmonics each controller acted on only one harmonic. We will refer to this as harmonic feedback (HF). Because each harmonic feeds back only to itself the (multi-input multi-output) HF controller has a diagonal structure. The zeroth harmonic was not considered important for uniform flow and was not used by Haynes [20].

5.2.3 Harmonic Feedback with Coupling

As shown in Chapter 4 distortion introduces coupling between the harmonics and one can argue that the coupling can be used to improve the performance of a controller. For example, the first harmonic can be fed back to the zeroth and second harmonics, as well as itself. If we use only the first three harmonics (plus zeroth), we need to find 16 gains and 15 spatial phases (there is no spatial phase shift on the zeroth harmonic). It is very time consuming to find all these gains and phases experimentally, so it was decided to employ coupling between the zeroth, first and second harmonics only. The use of first and second harmonics was based on the strong presence of these two harmonics in the first and second modes (see Chapter 4 for numbering of the modes). In the experiments with the distortion it was

found that the compression system was extremely sensitive to changes in the mean mass flow (that is, the rate at which the throttle was closed, see Section 2.4.2) so that it was argued that coupling between the zeroth and first harmonics might have a stabilizing effect.

With this scheme the form of the controller is

$$K = \begin{pmatrix} k_{00} & k_{01} & 0 & 0 \\ k_{10} & k_{11} & k_{12} & 0 \\ 0 & k_{21} & k_{22} & 0 \\ 0 & 0 & 0 & k_{33} \end{pmatrix}, \qquad k_{pq} = |k_{pq}|e^{i\beta_{pq}}, \quad p,q = 0,1,2,3.$$

The optimal values determined by Haynes were used for k_{11}, k_{22}, and k_{33}, and the other values k_{00}, k_{01}, k_{21} and k_{12} were determined experimentally. This controller will be referred to as harmonic feedback with coupling (HFC).

5.2.4 Distributed Feedback

Instead of decomposing the velocity perturbations into a sum of harmonics and feeding back the harmonics as we did with HF and HFC, we can view the velocity perturbation as a spatially distributed error signal which is fed back after it has been multiplied by a gain. Also, because the perturbation is rotating around the annulus it may be advantageous to include a spatial phase shift β to provide phase lead to compensate for the computational delay and actuator dynamics. These two simple arguments lead to the control law

$$\delta\gamma(\theta) = k\,\delta\phi(\theta - \beta). \tag{5.1}$$

This feedback law will be referred to as distributed feedback (DF). The constant gain k and spatial phase shift β was determined experimentally.

It is interesting to compare this new control law with the HF controller. We can rewrite Equation (5.1) in terms of the individual harmonics

$$\delta\widetilde{\gamma}_n = ke^{-in\beta}\delta\widetilde{\phi}_n \tag{5.2}$$

that is, the nth harmonic $\delta\widetilde{\phi}_n$ is rotated through an angle $n\beta$ and multiplied by a gain k to give nth harmonic $\delta\widetilde{\gamma}$. In contrast, each harmonic of the HF controller has its own gain k_{nn} and spatial phase shift β_{nn}

$$\delta\widetilde{\gamma}_n = k_{nn}e^{-i\beta_{nn}}\delta\widetilde{\phi}_n. \tag{5.3}$$

Another difference between the two control laws is that the spatial phase shifts of the higher harmonics of the DF controller are constrained to be multiples of that of the first harmonic. As a result, the phase relation that exists between the harmonics of $\delta\phi$ is preserved by the DF controller but not by the HF controller.

5.2.5 Controller Implementation

All the constant gain controllers can be implemented in a computationally efficient way without computing the harmonics. Let n_s be the number of sensors around the annulus and F_{n_s} be the DFT matrix corresponding to n_s sensors. Then we can compute the harmonics

$$\delta\widetilde{\boldsymbol{\phi}} = F_{n_s}\delta\boldsymbol{\phi}(\theta_s) \tag{5.4}$$

where $\delta\boldsymbol{\phi}(\theta_s)$ is a vector of velocity perturbation measurements at sensor locations $\theta_1, \ldots, \theta_{n_s}$ around the annulus. The harmonics of the control signal are now computed as

$$\begin{aligned}\delta\widetilde{\boldsymbol{\gamma}} &= K\delta\widetilde{\boldsymbol{\phi}} \\ &= KF_{n_s}\delta\boldsymbol{\phi}(\theta_s) \qquad \text{(from 5.4)}\end{aligned} \tag{5.5}$$

Table 5.1: Gains and spatial phases of the HF, HFC, and DF controllers.

Controller	k_{00}	k_{11}	β_{11}	k_{21}	β_{21}	k_{22}	β_{22}	k_{33}	β_{33}
HF	0	5.0	36°			4.1	91°	2.1	110°
HFC	0	5.0	36°	2.0	45°	4.1	91°	2.1	110°
DF	3	3.0	30°			3.0	60°	3.0	120°

where K is any constant gain controller. Let $F_{n_a}^{-1}$ be the inverse DFT matrix for synthesizing the AGV deflections $\delta\gamma(\theta_a)$ at n_a actuator locations $\theta_1, \ldots, \theta_{n_a}$ around the annulus, then

$$\begin{aligned}\delta\gamma(\theta_a) &= F_{n_a}^{-1}\delta\tilde{\gamma} \\ &= F_{n_a}^{-1} K F_{n_s}\, \delta\phi(\theta_s) \qquad \text{(from 5.5)} \\ &\triangleq K'\delta\phi(\theta_s). \end{aligned} \tag{5.6}$$

All the quantities are known so the matrix K' can be precomputed and therefore we can compute the individual actuator signals directly from the individual sensor signals without computing the harmonics. If the number of sensors is different from the number of actuators or if the sensors and actuators are at different locations around the annulus, K' is *not* a diagonal matrix even if the controller K is diagonal. The nondiagonal form is due to the interpolation of the inverse DFT.

5.3 Active Control Experimental Results

5.3.1 LQG Controller

The stalling flow coefficient for the LQG controllers are 0.455 and 0.475 for the 0.8 and 1.9 dynamic head distortions for an increase in stable operating range of 1.5% and 1.1%

respectively. The stable operating range has been increased by a small amount, but the point is that controllers based completely on the model can be used to stabilize the compressor.

Because LQG controllers assume that certain phase relations exist between the harmonics it is interesting to determine how sensitive the stalling flow coefficient is to changes in the phase relations. This was determined experimentally by turning the screen away from the position for which the controller was designed. The resulting stalling flow coefficients are shown in Figure 5.2. We see that for both positive and negative offsets a point is

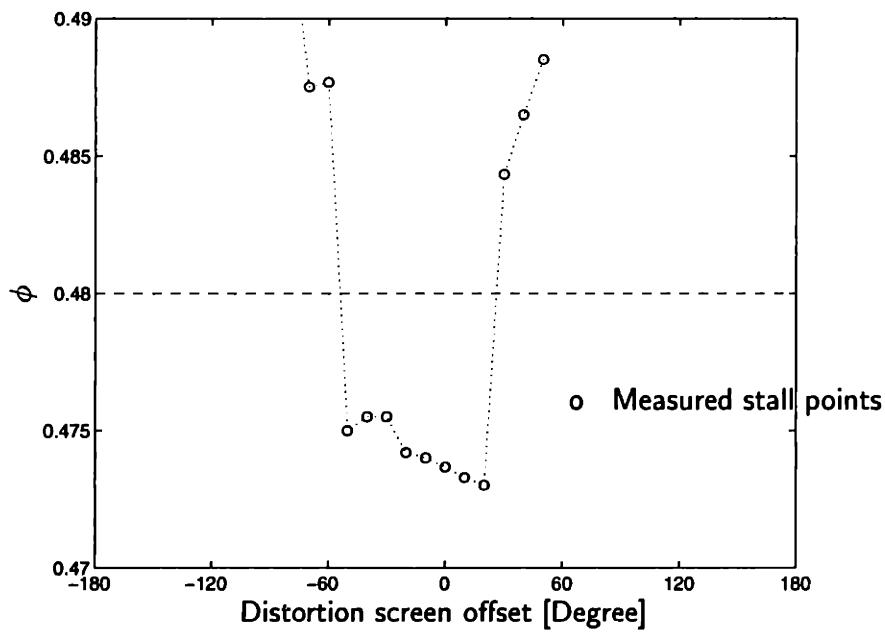

Figure 5.2: LQG sensitivity to offsets in distortion location. The dashed line shows the stalling flow coefficient without control.

reached beyond which the stalling flow coefficient increases suddenly above that of the open loop stall point so that the LQG controller has a destabilizing effect. This clearly shows the sensitivity of the LQG design to changes in system parameters.

The sensitivity to an offset in the distortion screen can be explained as follows. Rotating the screen away from its nominal position is equivalent to rotating both the sensors and

actuators in the opposite direction through the same angle. We will use the latter approach. If the angle through which the sensor and actuators are rotated is θ_o, that is, the screen is rotated by $-\theta_o$, then the rotated input and output harmonics are

$$\delta\tilde{\gamma}_n^{\theta_o} = \delta\tilde{\gamma}_n e^{+in\theta_o}$$

$$\delta\tilde{\phi}_n^{\theta_o} = \delta\tilde{\phi}_n e^{+in\theta_o}$$

respectively. Thus, the transfer function corresponding to the rotated configuration is obtained from the nominal transfer function G (see Equation (4.15)) as

$$G^{\theta_o} = \text{diag}[1,\, e^{+i\theta_o},\, e^{+i2\theta_o},\, e^{+i3\theta_o}]\; G\; \text{diag}[1,\, e^{-i\theta_o},\, e^{-i2\theta_o},\, e^{-i3\theta_o}] \tag{5.7}$$

$$= \begin{pmatrix} g_{00} & g_{01}e^{-i\theta_o} & g_{02}e^{-i2\theta_o} & g_{03}e^{-i3\theta_o} \\ g_{10}e^{+i\theta_o} & g_{11} & g_{12}e^{-i\theta_o} & g_{13}e^{-i2\theta_o} \\ g_{20}e^{+i2\theta_o} & g_{21}e^{+i\theta_o} & g_{22} & g_{23}e^{-i\theta_o} \\ g_{30}e^{+i3\theta_o} & g_{31}e^{+i2\theta_o} & g_{32}e^{+i\theta_o} & g_{33} \end{pmatrix}. \tag{5.8}$$

The transfer functions on the diagonal are unchanged, but the off-diagonal (or coupling) transfer functions are phase shifted. The LQG controller is a multi-input multi-output controller and uses all the relations between the different input and output harmonics, including coupling between different harmonics. By rotating the screen we have changed the system for which the controller was designed, and the phase change from the coupling was enough to destabilize the system. The sensitivity of the controller to changes in the coupling between the harmonics is not unique to the LQG controller. Any controller that directly relies on the coupling will be sensitive to offsets in the distortion.

5.3.2 Harmonic Feedback and Harmonic Feedback with Coupling

One question posed at the beginning of the chapter was whether HF controllers designed for uniform flow can stabilize the system in the presence of distortion. The answer to this question is affirmative. The stalling flow coefficients of the HF controller are 0.452 and 0.475 for the 0.8 and 1.9 dynamic head distortions for 2.2% and 1.1% increase in stable operating range respectively. Because the HF controller does not use any coupling between the harmonics it is insensitive to changes in the circumferential location of the distortion.

With the HF controller under uniform flow inlet conditions, Haynes [20] achieved an increase of 7.8% the operating range.

Another question is whether the flow coefficient can be lowered even further if we take the coupling into account. The HFC controller was used to address this. Spatial phases for the gains k_{12} and k_{21} were varied between 0 – 360°. It was found that $k_{12} = 0$ and $k_{21} = 2e^{i135^\circ}$ gave the best result, lowering the flow coefficient to 0.448 for the 0.8 dynamic head distortion, a 3% increase in stable operating range. A similar procedure was followed to determine k_{01} and k_{10} but it was found that the addition of these gains led to no improvement. The HFC controller thus increased the stable operating range 36% more than the HF controller which had no coupling between the harmonics. This improvement stems from knowledge of the coupling between the harmonics and thus the HFC controller will also be sensitive to offsets in the circumferential location of the distortion. The HFC controller was not used for the 1.9 dynamic head distortion.

5.3.3 Distributed Feedback Controller

The DF controller was experimentally tested under both distortions and uniform flow. In all cases it was found that a spatial phase shift in the range $30 \leq \beta \leq 70^\circ$ gave the best per-

formance. Unless stated otherwise $\beta = 30°$ was used. The stalling flow coefficients obtained with this controller were 0.445 and 0.472 for the 0.8 and 1.9 dynamic head distortions respectively. The corresponding improvement in stable operating ranges are 3.7% and 1.7%. Both these flow coefficients are lower than the corresponding HF and HFC stalling flow coefficients. The DF controller does not introduce coupling between the harmonics so that its performance is invariant under changes in the circumferential location of the distortion. An analysis comparing the HF and DF controllers will be given after we have discussed the effectiveness of the DF controller. Finally, we note that for all the controllers the model predicts that the system should be stable at the flow coefficients where we lose stability. Possible reasons for the loss of stability are discussed in Section 5.4.

Figure 5.3 shows the PSDs measured under closed loop operation using the DF controller. For reference the open loop PSDs (Chapter 4) are also shown in the graphs. The figures show frequencies only up to $1.1\,\omega_r$ because most of the energy in the perturbations is below $1\,\omega_r$. The effect of control is seen from the attenuation of the peaks of the first mode at $0.43\,\omega_r$ in the zeroth, first and second harmonics by 15, 23 and 8 dB respectively. The third harmonic did not show much open loop resonance and control appears to have little effect. In the PSDs we also see that control had very little, if any, effect on the peak at $1\,\omega_r$ suggesting that the disturbance corresponding to this frequency is (almost) uncontrollable from the AGVs. This was also true for the other controllers.

The magnitudes of the noise in the first and second harmonics has increased significantly from the corresponding open loop values for frequencies below $0.1\,\omega_r$; the situation is worse for the second harmonic where the noise had increased almost 15 dB for frequencies up to $0.35\,\omega_r$. The PSD is a measure of the energy in the signal at a specific frequency. In all the closed loop PSDs we see the largest values at very low frequencies and at $1\,\omega_r$, indicating significant energy at these frequencies and thus may be causes for the system losing stability;

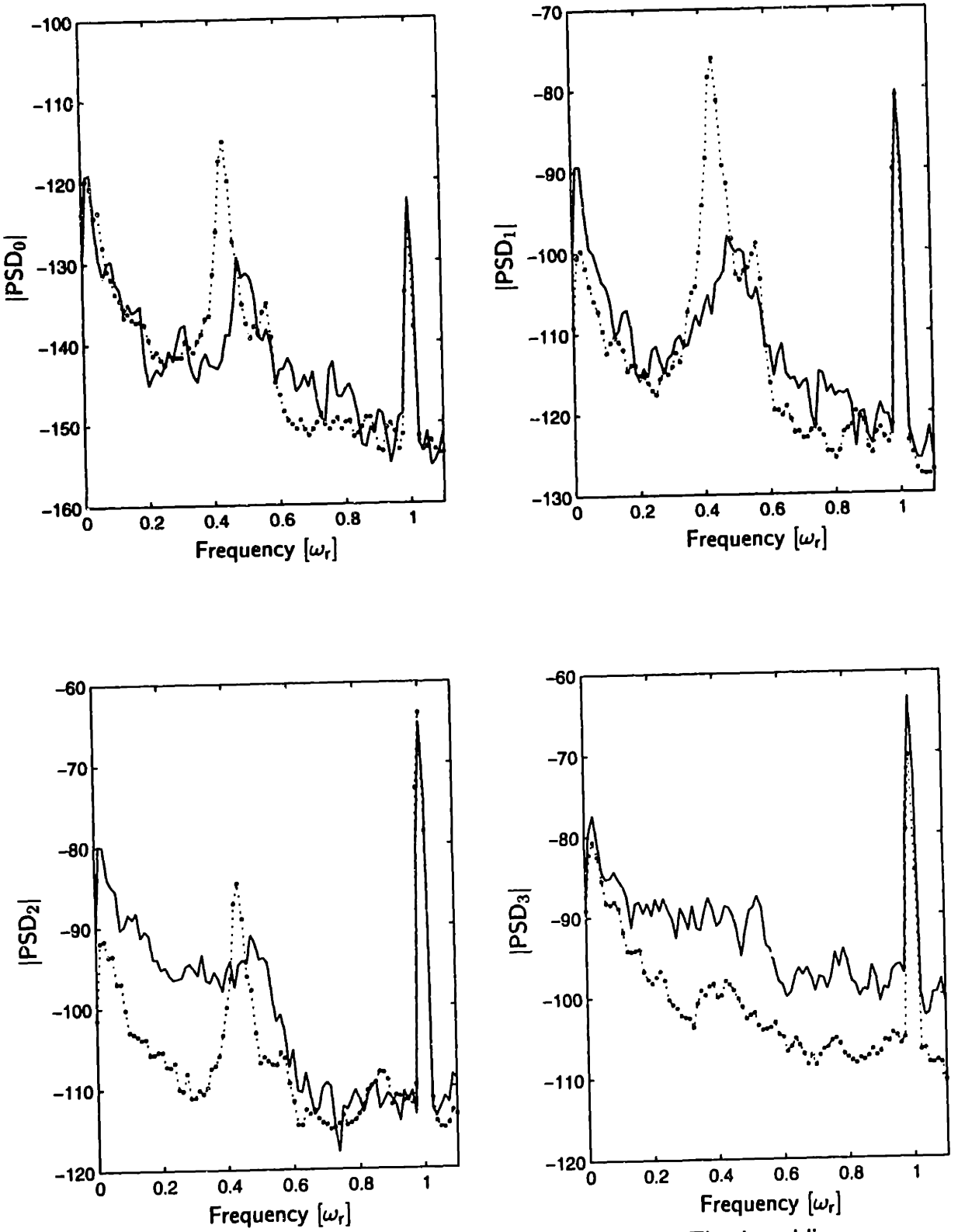

Figure 5.3: Closed loop PSDs for DF controller, solid line. The dotted lines are the open loop PSDs (Chapter 4).

this will be discussed further in Section 5.4.

5.3.4 Comparison between Harmonic and Distributed Feedback

We now compare the HF and DF controllers. The PSDs prior to stall with the HF controller look very much like the corresponding DF PSDs and are not shown. To highlight the differences between the two controllers we show in Figure 5.4 the differences in the magnitudes of the PSDs, that is,

$$\Delta|\mathrm{PSD}_n| = |\mathrm{PSD}_n^{\mathrm{HF}}| - |\mathrm{PSD}_n^{\mathrm{DF}}| \quad \text{for} \quad n = 0, 1, 2, 3. \tag{5.9}$$

In these figures positive values indicate that the DF controller attenuated perturbations more than the HF controller. For all the harmonics the HF controller attenuated perturbations more than the DF controller over the range $0.4 - 0.6\,\omega_r$ (approximately). For the zeroth, second, and third harmonics and for frequencies below $0.3\,\omega_r$ the DF controller attenuated disturbances more than the HF controller.

Earlier in this section we mentioned that there is a large amount of energy in the noise at frequencies below $0.1\,\omega_r$ where the DF controller generally had better disturbance rejection than the HF controller. It may thus be that noise at low frequencies contributes to the loss of stability at higher flow coefficients for the HF controller. For the zeroth, first, and second harmonics the DF controller attenuated perturbations more than the HF controller in the range $0.6 - 0.8\,\omega_r$.

The differences between the controllers can be explained by looking at the predicted root loci of the two controllers systems shown in Figure 5.5. As the gains are increased from zero (no control) to 100% (experimental values) the poles trace out the paths shown by the dots. In this figure we see that the HF controller stabilizes the pole associated with the first mode slightly more than the DF controller, consistent with the greater attenuation

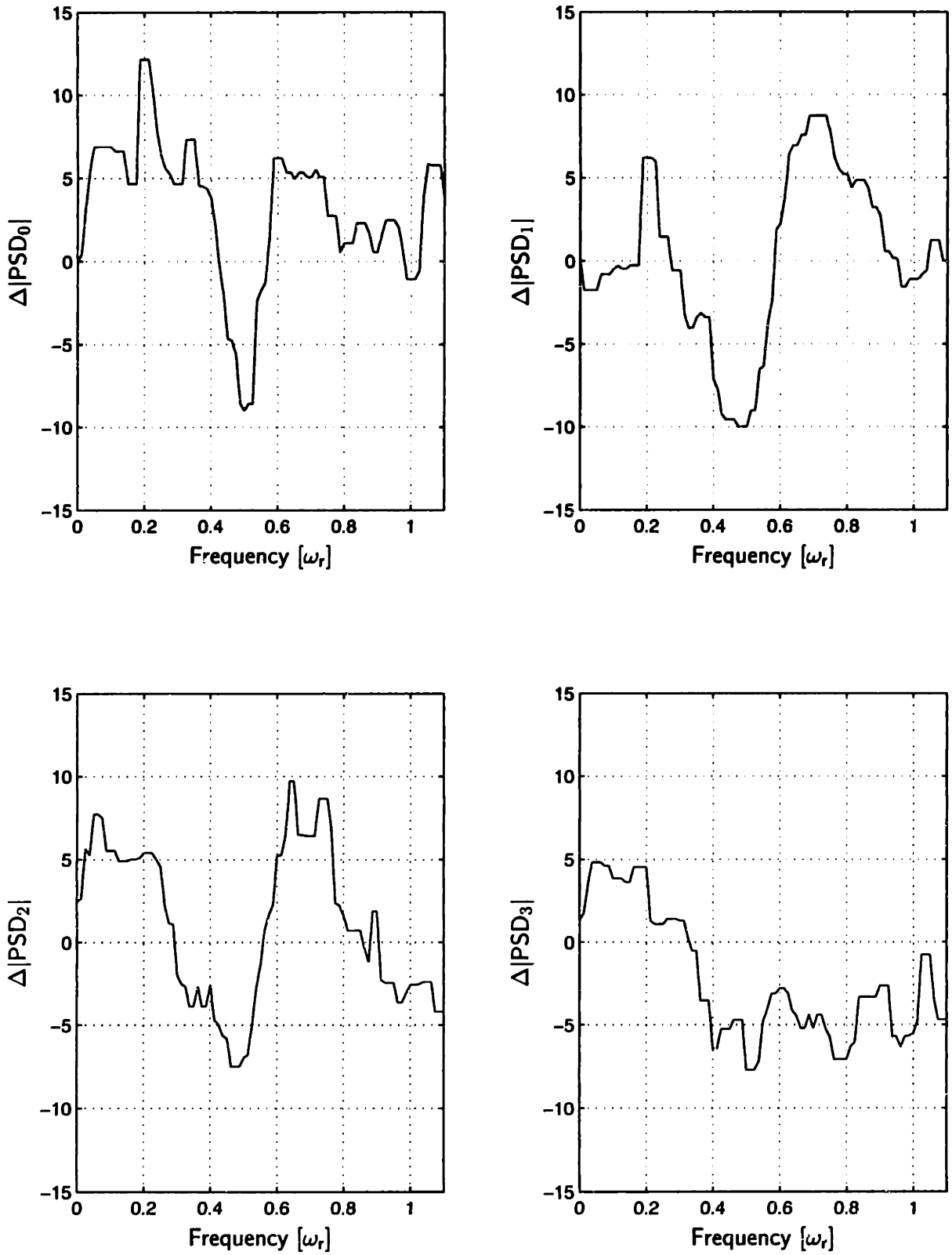

Figure 5.4: Difference between PSD magnitudes for HF and DF controllers. $\Delta|\text{PSD}_n| = |\text{PSD}_n^{\text{HF}}| - |\text{PSD}_n^{\text{DF}}|$.

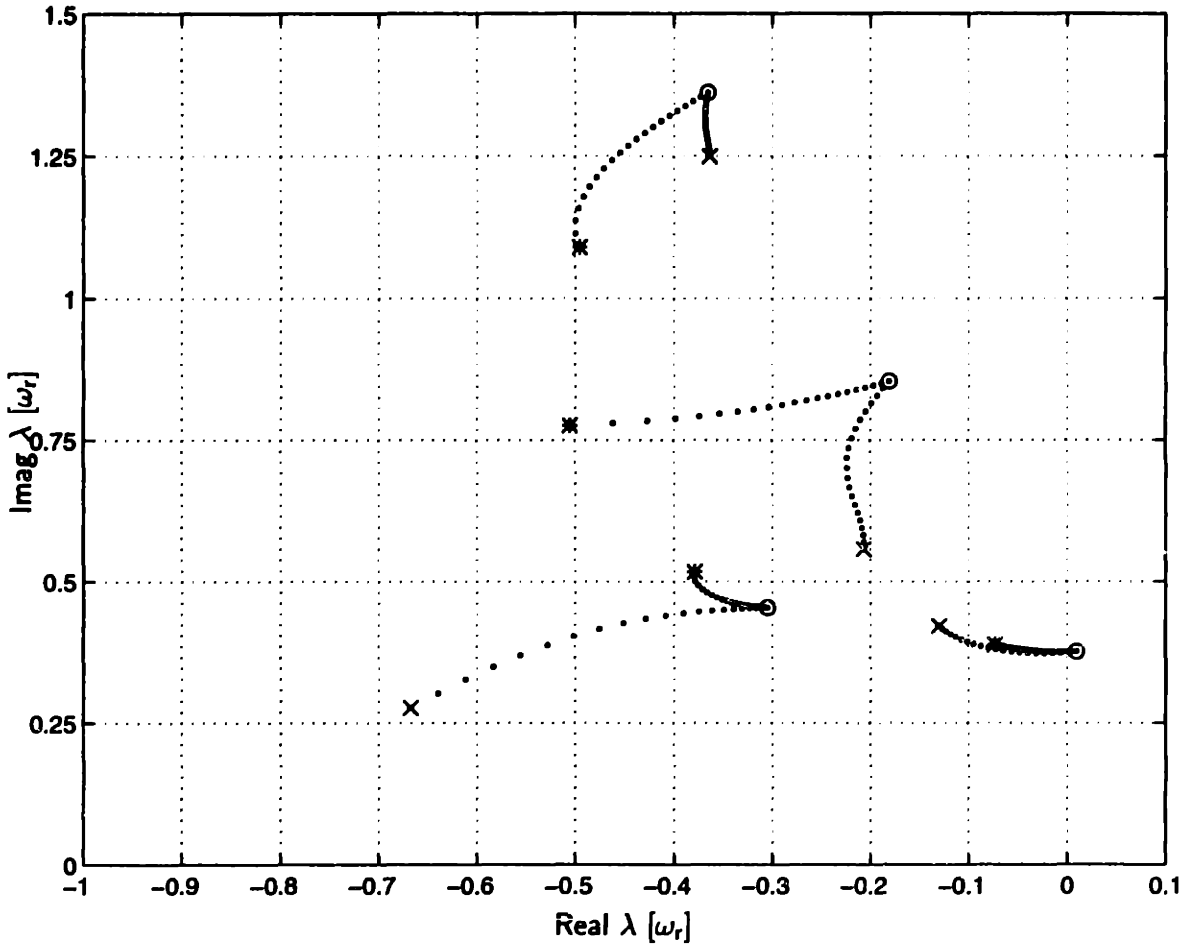

Figure 5.5: Root loci for HF and DF controllers. In this figure the dots trace the root locus as the gains are varied from 0% (no control) to 100% (experimental values). $*$ =DF controller, x=HF controller.

of perturbations by the HF controller in the frequency range $0.4 - 0.6\omega_r$ seen in Figure 5.4. The gain of the HF controller on the first harmonic, which is dominant in the first mode, is 66% larger than the corresponding DF controller gain while the spatial phase shifts are almost equal, 30° versus 36°.

The biggest difference between the two controllers is seen in the second mode. The DF controller has moved the pole associated with the second mode essentially horizontally into the left hand plane while the HF controller moved it almost vertically, offering little stabilization. The pole associated with the second mode of the DF closed loop system at approximately $\omega_2 = 0.75$ is in the range $0.6 - 0.8\omega_r$ over which the DF controller had more attenuation (Figure 5.4). This is surprising as the gain of the HF controller on the second harmonic, which is dominant in the second mode, is 37% larger than that of the DF controller. However, the phases of the two controllers are different, being 91° and 60° respectively. Thus, we conclude that the better stabilization of the second mode by the DF controller is due to the difference in the spatial phase shifts.

The third mode is also stabilized more by the DF controller. In this case the HF gain is approximately 30% smaller than that of the DF controller and the spatial phases, 110° for HF and 90° for DF, are different. The HF controller moved the pole vertically so that we again attribute the better stabilization to the difference in the phases of the two controllers. We have seen in the PSDs that the third harmonic did not show strong resonance. This is in part due to the fact that the third harmonic is not as strong in the first mode as the zeroth, first, and second harmonics, and in part due to the exponential decay of the higher harmonics upstream of the compressor which strongly attenuates the third harmonic. It is thus hard to determine the importance of the third harmonic.

In Section 3.6 we saw that the zeroth harmonic has a strong presence in the zeroth mode. It is thus surprising to see that the HF controller moved this mode further to

the left than the DF controller, even though the gain of the HF controller on the zeroth harmonic is zero, while that of the DF controller is $k = 3$. The first harmonic, however, has strong coupling with the zeroth harmonic. The larger gain on the first harmonic of the HF controller must have affected stabilization through this coupling. Thus, the model predicts, and experiments showed, that the DF controller stabilizes the compressor better than the HF controller.

The model predicts that the DF controller also performs better on distortions with different magnitudes and extents. The results obtained so far with the DF controller are promising, but additional experimental results are needed before its superiority can be established. However, the simplicity and ease of tuning make it a very attractive alternative to the HF and HFC controllers.

5.3.5 Other Experiments with Distributed Feedback Controller

We end this section by mentioning some variations of the DF controller that were used in experiments. In the previous discussion emphasis was put on the spatial phase shift β with little reference to the gain k. The experiments showed there was no measurable difference in the stalling flow coefficients for $2.5 \leq k \leq 4$. For $k < 2.5$ the stalling flow coefficient increased and for $k > 4.5$ the AGVs were continually driven into saturation with no decrease in stalling flow coefficient. The value $k = 3$ was thus used for all the experiments.

It was mentioned earlier that the compressor was very sensitive to changes in the mean mass flow (obtained through changes in the throttle setting). It was believed it might be due to the direct relation between mean mass flow and the zeroth harmonic and experiments were conducted where the gain on the zeroth harmonic was varied while gains on the

other harmonics were kept constant. No measurable changes were detected in stalling flow coefficients or PSDs. The root loci also show little variation when the gain on the zeroth harmonic is changed. The sensitivity due to changes in the mean mass flow thus remains unresolved.

The experimental rig had 16 hot-wires so that it was possible to measure the first seven harmonics. It was found that feeding back more than the first three harmonics (in the DF controller) led to no decrease in stalling flow coefficient. Due to the exponential decay of the upstream flow field the fourth harmonic is attenuated more than 20 dB, and the fifth, sixth, and seventh harmonics even more, so that the SNR of these harmonics will be much smaller than one. In addition, the model predicts that these harmonics do not have a strong presence in the first and second modes so that it is difficult to determine if they are important for active control.

Experiments were also conducted with eight hot-wires in the usual upstream locations and eight hot-wires installed downstream between the first rotor and stator. The hot-wires were at the same circumferential locations (see Figure 2.4, p.41). In this sensor configuration the DF controller was used to stabilize the system using either eight upstream or eight downstream hot-wires and the HF controller was used only with the eight upstream hot-wires. The stalling flow coefficients are listed in Table 5.2 for all the controllers.

For the DF controller, the stalling flow coefficient for using eight upstream hot-wires is higher than with 16 hot-wires, giving an increase of stable operating range of 1.7% versus 3.7% for 16 hot-wires. The degradation in performance is believed to be a result of the coarser localization of the wave with the smaller number of hot-wires. The HF controller performed poorly in this experiment and gave very little stabilization with only eight hot-wires. With the eight hot-wires behind the first rotor the DF controller had a lower stalling flow coefficient than the corresponding upstream case, 0.450 (2.6%) versus 0.454 (1.7%).

Table 5.2: Stalling flow coefficients. The first line shows the stalling flow coefficients and percentage increase in flow coefficient without control. The remaining lines list the stalling flow coefficients and percentage increase in stable operating range. The HF-8 and DF-8 indicate that only 8 hot-wires were used with these controllers. Percentages are computed with respect to the uniform flow stalling flow coefficient without control, $\phi = 0.460$.

Controller	Upstream 1.9 dynamic head		Upstream 0.8 dynamic head		Behind rotor 1 0.8 dynamic head	
No control	0.480	4.3%	0.462	0.4%	0.462	0.4%
LQG	0.475	1.1%	0.455	1.5%		
HF	0.475	1.1%	0.452	2.2%		
HFC			0.448	3.0%		
DF	0.472	1.7%	0.445	3.7%		
HF-8			0.460	0.4%		
DF-8			0.454	1.7%	0.450	2.6%

This result was unexpected as the hot-wires are in the rotor wakes so the SNR is decreased. However, this degradation is partly offset because the sensing is closer to the source of the perturbations so that the signal, especially the higher harmonics, will be captured better. In addition, analysis of the transmission zeros showed that moving downstream increased the frequency of the nonminimum phase zero by 50%. Thus, we should expect better stabilization.

5.4 Investigating Loss of Stability

In the previous section we mentioned that we lose stability at flow coefficients for which the extended model predicts the system should be stable. In this section we discuss experiments that were also performed to asses some conjectures concerning loss of stability. Two

simulations were also performed to determine if actuator saturation and nonlinear effects were causing the loss of stability.

Gysling [19] has found that acoustic modes in compression systems can have a destabilizing effect. To determine if any acoustic modes exist in the experimental compressor, high response pressure probes were installed in the plenum and the compressor was run at 1500, 1900, 2100 and 2400 revolutions per minute. In all the cases PSD analysis showed no new peaks and the peak of the first mode scaled with the mean rotor frequency. The experiments were repeated with the exhaust fan (see Figure 2.1 on p.36) turned on; again no differences were detected. It thus appears that acoustic modes are not responsible for the loss of stability.

Day [7] has found that some compressors do not show modal perturbations prior to stall. Instead, the stall cell developed out of a short length scale perturbation. To determine if short length scale perturbations were present eight hot-wires were removed from upstream and installed between the first rotor and stator. The limited experiments conducted with this sensor arrangement showed no evidence of short length scale perturbations. However, it was found that the formation of the stall cell was visible approximately one rotor revolution earlier by the hot-wires behind the rotor.

In the PSDs of Chapter 4 we saw that there is nonlinear interaction between the disturbance at $1\,\omega_r$ and the first mode, resulting in peaks at $\omega_r \pm \omega_1$. A similar type of nonlinear interaction was also observed when the system was excited with a sinusoidal signal of frequency ω_e by the AGVs — peaks appeared in the PSD at exactly $\omega_r \pm \omega_e$. In this experiment the level of excitation was 5°, which is well within the linear operating range of the AGVs. The linearity of the AGVs was verified by taking a full set of transfer functions at the same mean mass flow with 5° and 10° excitation levels. The transfer functions were in excellent agreement so we conclude that the nonlinear coupling is not due to nonlinearity

in the AGVs and must be due to another phenomenon.

Prior to the installation of the distortion screens uniform flow transfer functions were measured with uniform flow. The model predicts that the harmonics are not coupled and that the zeroth harmonic is not important for uniform flow, but the full multi-input multi-output transfer functions were measured. The uniform flow transfer functions are shown in Figure 5.6. The coupling between the different harmonics, including the zeroth, is clearly visible. Note that the peaks in the off-diagonal transfer functions are at the *same* frequency as that of the first mode. This behavior is similar to that we have seen when distortion is present, and therefore must be due to nonlinear effects. These transfer functions were measured at $\phi = 0.460$, the open loop uniform flow stall point. Uniform flow transfer functions measured at $\phi = 0.470$ showed no coupling between the harmonics. At this higher flow coefficient the resonant peak of the first mode is significantly smaller than at $\phi = 0.460$ and the coupling must therefore be a result of the larger perturbation magnitudes. This coupling was not expected and led to the determination of the magnitudes of the perturbations necessary for nonlinear effects to become important. This is discussed in the next section.

5.4.1 Nonlinear Simulations

Analysis of the actuator deflections showed that the AGVs were often driven into saturation prior to stall. To determine if this was causing the loss of stability the closed loop was simulated with the magnitudes of the actuator deflections limited to 15°, the maximum value allowed in the experiments. These simulations showed that the closed loop system should be stable at the flow coefficients where the experimental system lost stability. It was also found experimentally that a decrease in the maximum AGV deflections up to approximately 20% has little effect on the stalling flow coefficient. Therefore, the saturating

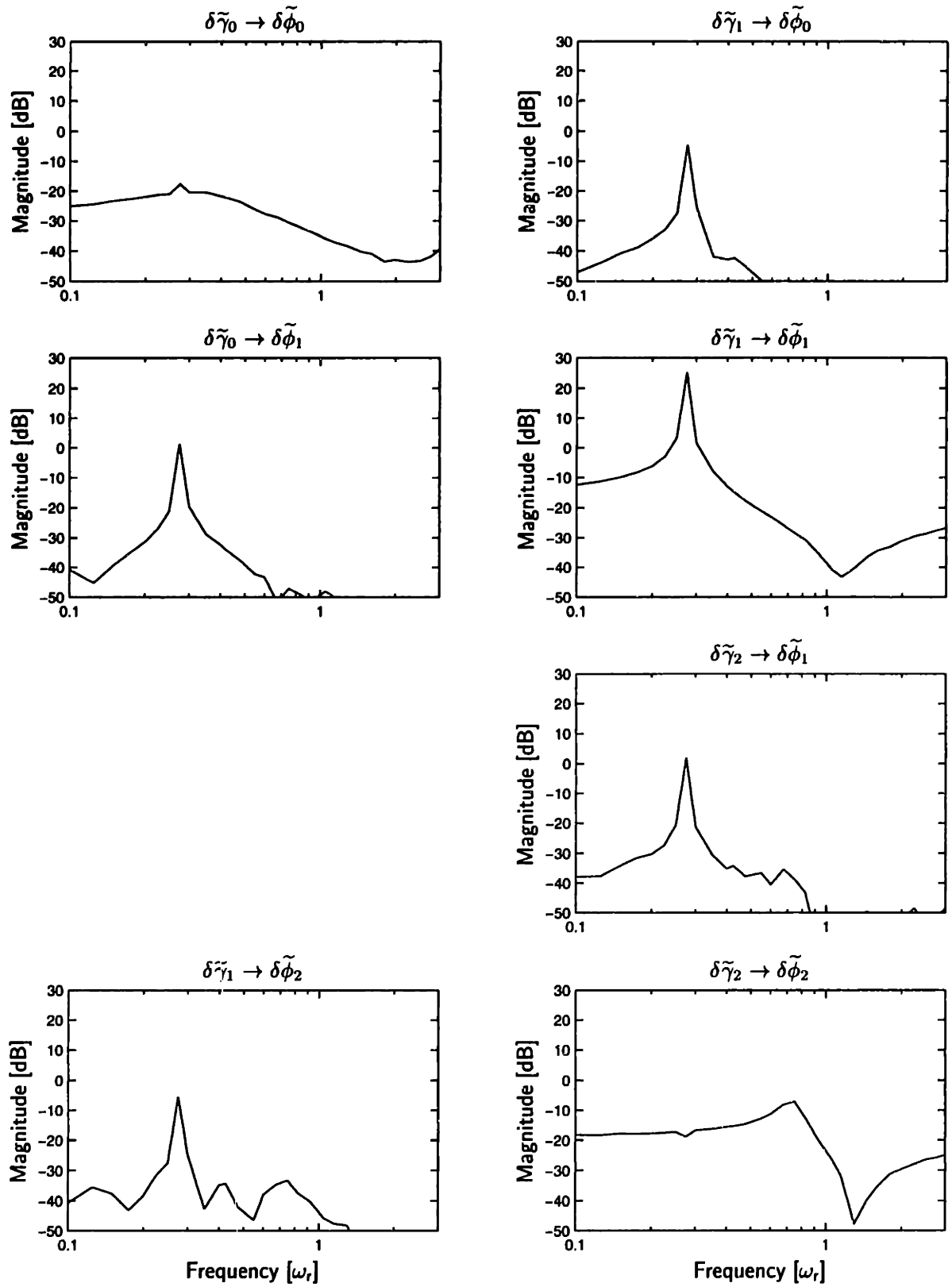

Figure 5.6: Magnitudes of transfer functions, uniform flow, $\phi = 0.460$.

AGVs is not the limiting factor.

In Chapter 4 we saw that the envelopes of the measured velocity perturbations were not symmetrically distributed about zero, suggesting nonlinear behavior. The PSDs in that chapter also showed effects characteristic of nonlinear behavior. Earlier in this chapter it was mentioned that for small levels of AGV forcing nonlinear behavior was also observed. Nonlinear coupling was also observed in the uniform flow transfer functions in Figure 5.6. These observations suggest that the magnitudes of the velocity perturbations may be large enough so that terms ignored during linearization may be significant. In this section we determine through a simple simulation if this is the case. The analysis presented here is far from complete and was performed to see if additional research is necessary in this direction. Detailed nonlinear analysis (using Lyapunov stability theory) was done by Mansoux [31] for uniform flow, but no such research has been done for distorted flow.

To estimate the effect of nonlinearity terms up to second order were kept in the Taylor series expansion of Equation (3.28). The expression for the pressure rise across the compressor is

$$\delta(p_s^{(4)} - p_t^{(3)}) = \left[\frac{\partial \psi}{\partial \phi} - \mu_r \frac{\partial}{\partial \theta}\right] \delta\phi^{(3)} + \frac{1}{2}\frac{\partial^2 \psi}{\partial \phi^2}(\delta\phi^{(3)})^2 - \mu_c \delta\dot{\phi}^{(3)}. \tag{5.10}$$

We will only analyze the homogeneous system so the AGV forcing term is not included here. All the other pressure balance equations were kept the same. Calculations were carried out for the 0.8 dynamic head distortion at a flow coefficient 1% above the open loop stalling flow coefficient.

It was found that the magnitude $|\delta\phi(\tau = 0)|$ of the initial velocity perturbation above which the system goes unstable was $|\delta\phi| = 0.029$. In Chapter 4 we saw that the magnitude of the pre-stall perturbations exceeded this value. Although this is a highly simplified analysis

it makes plausible the case that nonlinear effects may be important in determining loss of stability, but more research is necessary in this area.

5.5 Summary

In this chapter we presented the first experimental evidence that active control can be used to increase the stable operating range of a compressor operating with circumferential inlet distortion. The stable operating range was increased by 3.7% and 1.7% for the two 120° distortions of magnitude 0.8 and 1.9 dynamic head respectively by the distributed feedback controller. It was also shown experimentally that the harmonic feedback controllers optimized for uniform flow were effective in the presence of these distortions, although the corresponding stall flow coefficients were higher than that of the distributed feedback controller. By using the coupling between the harmonics it was possible to lower stalling flow coefficient. LQG controllers based completely on the model also stabilized the compression system at open loop unstable points.

The reason for loss of stability is not known, but experimental evidence and analysis of the model suggest that the pre-stall perturbations are large enough for nonlinear effects to become significant.

---

6 Summary

An analytic and experimental study were carried out on a low speed three-stage axial compressor to assess the use of active control for increasing the stable operating range of a compressor in the presence of circumferential inlet total pressure distortion. A set of movable guide vanes was used for actuation. Steady state and dynamic response behavior, under open and closed loop conditions, were examined.

Linear quadratic Gaussian controllers based completely on the model stabilized the system at open loop unstable operating points. This is the first experimental assessment of the application of modern control design methodologies to the control of rotating stall in the presence of total pressure inlet distortion. The range extension was 1.5% and 1.1% for 0.8 and 1.9 dynamic head distortions respectively.

Constant gain harmonic controllers optimized for uniform flow were also able to stabilize the compressor in the presence of distortion, extending the operating range by 2.2% and 1.1% for distortions of 0.8 and 1.9 dynamic heads 120° extent respectively. Taking into account the coupling between harmonics of the perturbations increased the stable operating range by 3% for the 0.8 dynamic head distortion.

A new control law, called distributed feedback, was introduced and was found experimentally to have superior performance in the presence of distortion. This control law has a single gain and spatial phase shift. The distributed feedback controller increased the stable operating range by 3.7% and 1.7% for 0.8 and 1.9 dynamic head 120° distortions respectively. Analysis has shown that the improved performance results from better stabilization of the second mode and better suppression of low frequency noise. The extended Hynes-

Table 6.1: Comparison between Uniform and Distorted Flow

Uniform Flow	Distorted Flow
Harmonics are decoupled. Section 3.6	Strong coupling between harmonics, including zeroth.
Mode shapes are sinusoidal and time invariant. Section 3.6	Mode shapes are nonsinusoidal, change with time as wave propagates around the annulus.
Envelope of velocity perturbations uniform around annulus. Section 4.2.1	Envelope of velocity perturbations nonuniform around annulus.
Disturbance at $1\,\omega_r$ present only in first harmonics. Section 4.2.2	Disturbance at $1\,\omega_r$ stronger and present in all harmonics.
SNR = 1.25 for the first harmonic. Section 4.2.2	SNR = 0.34, 0.63, 0.29 for zeroth, first, and second harmonics.
Stalling flow coefficient = 0.460. Sections 4.1.2 and 5.3.	Stalling flow coefficients: 0.462 (+0.4%) and 0.480 (+4.3%) for 0.8 and 1.9 dynamic head distortions respectively.
System becomes nonminimum phase at $\phi =$ 0.464(+0.9%). Section 3.7.	System becomes nonminimum phase at $\phi =$ 0.467(+1.5%) and $\phi =$ 0.486(+5.6%) for 0.8 and 1.9 dynamic head distortions.
7.8% increase in operating range with active control. Section 5.3	3.7% and 1.7% increase in operating range for 0.8 and 1.9 dynamic head distortions with active control.

Greitzer model for compressor response to inlet distortion predicts that this controller would also perform better for other distortions with different magnitudes and extents.

Transfer functions from the actuator guide vanes to the hot-wires measured at several mass flows were in good agreement with those predicted by the extensions of the Hynes-

Greitzer model. This is the first experimental evidence that quantitatively establishes the ability of the model to predict the dynamics of small perturbations in the presence of distortion. The transfer functions clearly showed the coupling between harmonics which is characteristic of the modes that occur in the presence of inlet distortion. The open loop stalling flow coefficient for the 0.8 dynamic head distortion was correctly predicted by the model, but was over estimated for the 1.9 dynamic head distortion. This discrepancy is probably due to the fact that the compressor pressure rise characteristic is not known over the complete range of the velocities present for the large distortion.

The experimental results revealed nonlinear dynamic behavior connected with stall inception. The envelope of the velocity perturbations follows the trend predicted by the model, but is not symmetrically distributed about the mean. Power density spectra revealed an interaction between the first mode and the disturbance at one rotor revolution, and a nonlinear simulation showed that, at the magnitudes of perturbations observed prior to stall, nonlinear effects may be significant.

Future Research

Several questions remain unsolved and need additional investigation. The most important, loss of stability under active control, is not understood. Spectral analysis has shown that all the controllers suppressed perturbations of the most unstable mode well, but there is a significant amount of energy in low frequency noise as well as at one rotor revolution. The noise far upstream and at the throttle exit does not follow the trends observed in the experiments, and it is not known if the low frequency noise contributes to the loss of stability. In addition, experimental data showed various forms of nonlinear behavior, and it is not known whether it is driving the system unstable. The disturbance at one rotor revolution is significantly stronger in the presence of distortion and interacted in a nonlinear

way with the first mode. The cause of this disturbance is not known, and it is also not known if it contributes to the loss of stability.

The extent and intensity of the distortions have been assumed known and time invariant but this is not a realistic assumption under all circumstances. The effectiveness of the controllers must be verified in the presence of unknown, time varying distortions. If the rate at which the distortion changes is slow compared to the dynamics of rotating stall, the distortion can be approximated as steady, and it may be possible to find controllers, optimized for the instantaneous distortion, in real time using recursive algorithms.

Schulmeyer [43] showed that restaggering inlet guide vanes by 10° decreased the nonuniformity in the flow by 50% and gave an increase in pressure rise of 5.3%. By combining restaggering inlet guide vanes with active control we should be able to achieve a larger increase in the stable operating range. If the distortion is changing slowly the restaggering can be done dynamically in real time. This combined approach is promising and warrants further investigation.

Appendix A Fourier Convolution Matrix

Let two Fourier series be given by

$$f(\theta) = f_0 + \sum_{p=1}^{n_f} (f_{cp} \cos p\theta + f_{sp} \sin p\theta) \tag{A.1}$$

$$g(\theta) = g_0 + \sum_{q=1}^{n_g} (g_{cq} \cos q\theta + g_{sq} \sin q\theta). \tag{A.2}$$

Multiplying the Fourier series $f(\theta)$ with n_f harmonics with $g(\theta)$ with n_g harmonics gives another Fourier series $p(\theta)$ with $n_f + n_g$ harmonics. Note that a Fourier series with n harmonics has $2n + 1$ Fourier coefficients.

We would like to compute the product $p(\theta) = f(\theta)g(\theta)$ and write it in the form $\widetilde{p} = F(f)\widetilde{g}$ where $F(f)$ is the $(2(n_f + n_g) + 1) \times (2n_g + 1)$ Fourier convolution matrix with elements that are functions of the coefficients of $f(\theta)$, $\widetilde{g}$ is a $2n_g + 1$ vector with elements the coefficients of $g(\theta)$ stored in the format

$$\widetilde{g} = [g_{c0}, g_{c1}, g_{s1}, g_{c2}, g_{s2}, \cdots, g_{cn_g}, g_{sn_g}]^T, \tag{A.3}$$

and $\widetilde{p}$ is a $2(n_f + n_g) + 1$ vector with elements the coefficients of the product $p(\theta)$ stored in

a format similar to that of $\widetilde{g}$. Write the product as

$$f(\theta)g(\theta) = f_0 g_0 + f_0 \sum_{q=1}^{n_g} (g_{cq} \cos q\theta + g_{sq} \sin q\theta) \tag{A.4}$$

$$+ \sum_{p=1}^{n_f} (f_{cp} \cos p\theta + f_{sp} \sin p\theta)\, g_0 \tag{A.5}$$

$$+ \sum_{p=1}^{n_f} f_{cp} \cos p\theta \sum_{q=1}^{n_g} g_{cq} \cos q\theta + \sum_{p=1}^{n_f} f_{cp} \cos p\theta \sum_{q=1}^{n_g} g_{sq} \sin q\theta \tag{A.6}$$

$$+ \sum_{p=1}^{n_f} f_{sp} \sin p\theta \sum_{q=1}^{n_g} g_{cq} \cos q\theta + \sum_{p=1}^{n_f} f_{sp} \sin p\theta \sum_{q=1}^{n_g} g_{sq} \sin q\theta \tag{A.7}$$

The coefficients of the expressions in (A.4) and (A.5) are easy to handle. The expressions in (A.6) and (A.7) have products of the form $\cos p\theta \cos q\theta$, $\cos p\theta \sin q\theta$, $\sin p\theta \cos q\theta$, and $\sin p\theta \sin q\theta$. From standard trigonometric identities these are given by

$$f_{cp} g_{cq} \cos p\theta \cos q\theta = \frac{f_{cp}}{2}[\cos(p+q)\theta + \cos(p-q)\theta] g_{cq} \tag{A.8}$$

$$\begin{aligned} f_{cp} g_{sq} \cos p\theta \sin q\theta &= \frac{f_{cp}}{2}[\sin(p+q)\theta - \sin(p-q)\theta] g_{sq} \\ &= \frac{f_{cp}}{2}[\sin(p+q)\theta - \operatorname{sign}(p-q) \sin(|p-q|)\theta] g_{sq} \end{aligned} \tag{A.9}$$

$$\begin{aligned} f_{sp} g_{cq} \sin p\theta \cos q\theta &= \frac{f_{sp}}{2}[\sin(p+q)\theta + \sin(p-q)\theta] g_{cq} \\ &= \frac{f_{sp}}{2}[\sin(p+q)\theta + \operatorname{sign}(p-q) \sin(|p-q|)\theta] g_{cq} \end{aligned} \tag{A.10}$$

$$f_{sp} g_{sq} \sin p\theta \sin q\theta = -f_{sp} 2[\cos(p+q)\theta - \cos(p-q)\theta] g_{sq} \tag{A.11}$$

where $|\cdot|$ denotes absolute value and

$$\operatorname{sign}(p-q) = \begin{cases} +1 & \text{if } p > q, \\ 0 & \text{if } p = q, \\ -1 & \text{if } p < q. \end{cases} \tag{A.12}$$

The sign and absolute value modifications are included to simplify software implementation. Therefore, for each of the four products and for each combination of p and q, we get two entries in the matrix: one corresponding to $p+q$ and one to $p-q$. This brute force method is not the most efficient way to construct the Fourier convolution matrix but works quite well for practical sized problems.

We illustrate the use of the Fourier convolution matrix with an example. Let

$$f(\theta) = 1 + 2\cos\theta + 4\sin\theta$$

$$g(\theta) = -2 + 6\cos\theta - 8\sin\theta, \tag{A.13}$$

then $p(\theta) = -12 + 2\cos\theta - 16\sin\theta + 22\cos 2\theta + 4\sin 2\theta$. Vectorizing we get

$$F(f) = \begin{pmatrix} 1 & 1 & 2 \\ 2 & 1 & 0 \\ 4 & 0 & 1 \\ 0 & 1 & -2 \\ 0 & 2 & 1 \end{pmatrix}, \tag{A.14}$$

and $\widetilde{g} = [-2, 6, -8]^T$. Multiplying the matrix $F(f)$ with the vector $\widetilde{g}$ we get

$$\widetilde{p} = [-12, 2, -16, 22, 4]^T. \tag{A.15}$$

The elements of $\widetilde{p}$ are exactly the coefficients of $p(\theta)$.

This example also illustrates the increase in the number of harmonics that we get when we multiply two Fourier series. For software implementation we need to take care of this increase in the number of harmonics. This is especially true for the least squares minimization routine that uses an iterative algorithm to solve for the steady flow. The approach adopted here was to truncate the order of the Fourier series after every multiplication to a

predetermined number of harmonics. The number of harmonics that is needed was found through simulations and is discussed in Section 3.3.3.

Appendix B AGV Dynamics

Expressions for the pressure rise across and flow perturbations through nonuniformly staggered AGVs for uniform steady flow were derived by Longley [26]. In this appendix we extend the results to the nonuniform steady flow case. In contrast to the chapters in the thesis the derivation in this appendix uses absolute values of some variables and we will nondimensionalize the expression as we proceed. In particular, the variables b_a, p_t, and x are *not* nondimensionalized; the remaining variables have their usual meaning.

Consider two vanes at circumferential locations θ and $\theta + \Delta\theta$ with deflections γ and $\gamma + \Delta\gamma$ respectively as shown in the figure below. The widths between the vanes at station 2 (inlet) and station 3 (outlet) are given by

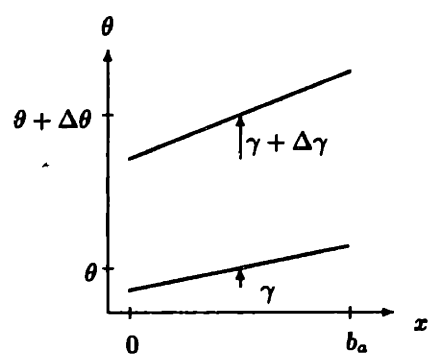

$$w^{(2)} = \bar{r}\Delta\theta - \frac{b_a}{2}[(\gamma + \Delta\gamma) - \gamma]$$

$$w^{(3)} = \bar{r}\Delta\theta + \frac{b_a}{2}[(\gamma + \Delta\gamma) - \gamma]$$

respectively. Dividing through by $\bar{r}\Delta\theta$ and taking the limit $\Delta\theta \to 0$ we get

$$\frac{w^{(2)}}{\bar{r}\Delta\theta} = 1 - \frac{b_a}{2\bar{r}}\gamma'$$
$$\frac{w^{(3)}}{\bar{r}\Delta\theta} = 1 + \frac{b_a}{2\bar{r}}\gamma'$$

where we used a prime to indicate derivative with respect to θ. Mass conservation requires that $w^{(2)}\phi^{(2)} = w^{(3)}\phi^{(3)}$, so that, to first order,

$$\phi^{(2)} = (1 + \mu_a\gamma')\phi^{(3)} \tag{B.1}$$

where we have used the definition $\mu_a = b_a/\bar{r}$. Linearizing this equation about the nonuniform steady flow ϕ_s and steady deviation γ_s we get

$$\delta\phi^{(2)} = (1 + \mu_a\gamma_s')\delta\phi^{(3)} + \mu_a\phi_s\delta\gamma'. \tag{B.2}$$

Next we find an expression for the total pressure across the AGVs. Along a streamline

$$\frac{p_t}{\rho} + \frac{\partial\varphi}{\partial t} = \text{constant} \tag{B.3}$$

$$c_x = \phi u_w$$
$$= \frac{\partial\varphi}{\partial x}. \tag{B.4}$$

Assuming a linear axial velocity distribution between stations (2) and (3) we can write

$$c_x(x) = c_x^{(2)} + \frac{x}{b_a}(c_x^{(3)} - c_x^{(2)}).$$

With this velocity relation we have from Equation (B.4)

$$\varphi(x,t) = c(t) + xc_x^{(2)} + \frac{x^2}{2b_a}(c_x^{(3)} - c_x^{(2)})$$
$$\frac{1}{u_w}\frac{\partial\varphi}{\partial t} = \frac{1}{u_w}\frac{\partial c(t)}{\partial t} + \frac{\partial\phi^{(2)}}{\partial t} + \frac{x^2}{2b_a}\frac{\partial}{\partial t}(\phi^{(3)} - \phi^{(2)}).$$

From Equation (B.3) we get

$$\frac{p_t^{(3)} - p_t^{(2)}}{\rho} = \frac{\partial \varphi^{(2)}}{\partial t} - \frac{\partial \varphi^{(3)}}{\partial t}.$$

Simplifying and nondimensionalizing this equation gives

$$\frac{p_t^{(3)} - p_t^{(2)}}{\rho u_w^2} = -\mu_a \frac{\partial}{\partial \tau}\left(\frac{1}{2}(\phi^{(3)} - \phi^{(2)})\right). \tag{B.5}$$

From Equation (B.1) we get the first order approximation

$$\frac{1}{2}(\phi^{(3)} - \phi^{(2)}) \approx (1 + \frac{1}{2}\mu_a \gamma')\phi^{(3)}.$$

Substituting this into Equation (B.5) and simplifying gives

$$\frac{p_t^{(3)} - p_t^{(2)}}{\rho u_w^2} = -\mu_a \frac{\partial}{\partial \tau}(1 + \frac{1}{2}\mu_a \gamma')\phi^{(3)}.$$

Linearizing this equation about the nonuniform steady flow gives

$$\frac{\delta p_t^{(3)} - \delta p_t^{(2)}}{\rho u_w^2} = -\mu_a(1 + \frac{1}{2}\mu_a \gamma')\delta\dot{\phi}^{(3)} - \frac{\mu_a^2}{2}\phi_s \delta\dot{\gamma}'. \tag{B.6}$$

Equations (B.2) and (B.6) are the equations needed for the linearized dynamics.

Appendix C Transfer Functions

C.1 Complex Input-Output Transfer Functions

In this appendix we derive expressions to compute the complex-input to complex-output harmonic transfer functions given the real-input to real-output harmonic transfer functions. The complex-input to complex-output transfer functions will be referred to as complex transfer functions.

For simplicity we derive the results for one harmonic plus the zeroth harmonic and use the subscripts c, s, and 0 to refer to the cosine, sine and zeroth harmonic coefficients respectively. The results hold for all harmonics $n > 0$ and the input and output harmonic numbers do not have to be the same. Consider the real-input real-output transfer function defined by

$$\begin{bmatrix} y_0(i\omega) \\ y_c(i\omega) \\ y_s(i\omega) \end{bmatrix} = \begin{bmatrix} g_{00}(i\omega) & g_{0c}(i\omega) & g_{0s}(i\omega) \\ g_{c0}(i\omega) & g_{cc}(i\omega) & g_{cs}(i\omega) \\ g_{s0}(i\omega) & g_{sc}(i\omega) & g_{ss}(i\omega) \end{bmatrix} \begin{bmatrix} u_0(i\omega) \\ u_c(i\omega) \\ u_s(i\omega) \end{bmatrix}. \tag{C.1}$$

To keep the notation uncluttered we will omit the dependency of the transfer functions on $i\omega$ in most of the expressions. Define the complex harmonic output

$$y(t) = y_c(t) + iy_s(t) \qquad y(i\omega) = y_c(i\omega) + iy_s(i\omega) \tag{C.2}$$

$$y^*(t) = y_c(t) - iy_s(t) \qquad \overset{\star}{y}(i\omega) = y_c(i\omega) - iy_s(i\omega) \tag{C.3}$$

where y^* is the complex conjugate of y. Note that $y^*(i\omega) \neq \overset{\star}{y}(i\omega)$. Similarly, for the complex

harmonic input u we have

$$u(t) = u_c(t) + iu_s(t) \qquad u(i\omega) = u_c(i\omega) + iu_s(i\omega)$$

$$u^*(t) = u_c(t) - iu_s(t) \qquad \overset{*}{u}(i\omega) = u_c(i\omega) - iu_s(i\omega).$$

As noted in Section C.1 the definitions of the complex harmonics do not correspond to the standard relation between real and complex Fourier coefficients. The two variables y^* and u^* are introduced to simplify the similarity transformation. The similarity transformation matrix and its inverse that corresponds to these definitions are

$$T = \begin{bmatrix} 1 & 0 & 0 \\ 0 & 1 & i \\ 0 & 1 & -i \end{bmatrix} \qquad T^{-1} = \frac{1}{2}\begin{bmatrix} 2 & 0 & 0 \\ 0 & 1 & 1 \\ 0 & -i & i \end{bmatrix}.$$

Applying the similarity transformation to Equation (C.1) we get the complex transfer functions

$$\begin{bmatrix} y_0(i\omega) \\ y(i\omega) \\ \overset{*}{y}(i\omega) \end{bmatrix} = \begin{bmatrix} g_{00} & \frac{1}{2}(g_{0c} - jg_{0s}) & \frac{1}{2}(g_{0c} + jg_{0s}) \\ g_{c0} + ig_{s0} & \frac{1}{2}[(g_{cc} + g_{ss}) - i(g_{cs} - g_{sc})] & \frac{1}{2}[(g_{cc} - g_{ss}) + i(g_{cs} + g_{sc})] \\ g_{c0} - ig_{s0} & \frac{1}{2}[(g_{cc} - g_{ss}) - i(g_{cs} + g_{sc})] & \frac{1}{2}[(g_{cc} + g_{ss}) + i(g_{cs} - g_{sc})] \end{bmatrix} \begin{bmatrix} u_0(i\omega) \\ u(i\omega) \\ \overset{*}{u}(i\omega) \end{bmatrix} \tag{C.4}$$

$$\triangleq \begin{bmatrix} g_{00}(i\omega) & g_{0u}(i\omega) & g_{0\overset{*}{u}}(i\omega) \\ g_{y0}(i\omega) & g_{yu}(i\omega) & g_{y\overset{*}{u}}(i\omega) \\ g_{\overset{*}{y}0}(i\omega) & g_{\overset{*}{y}u}(i\omega) & g_{\overset{*}{y}\overset{*}{u}}(i\omega) \end{bmatrix} \begin{bmatrix} u_0(i\omega) \\ u(i\omega) \\ \overset{*}{u}(i\omega) \end{bmatrix}. \tag{C.5}$$

We are especially interested in the transfer functions $g_{00}(i\omega)$, $g_{0u}(i\omega)$, $g_{y0}(i\omega)$, and $g_{yu}(i\omega)$. For positive values of ω these give the complex transfer functions between the different harmonics and a peak in the magnitude of the transfer function will indicate a wave travelling in the same direction as the rotor. Because the input and output signals are complex

these transfer functions do not satisfy the complex conjugate symmetry property and the transfer functions at negative frequencies look completely different from those at positive frequencies. Therefore, if we want to have a complete picture of the system, we need to look at both positive and negative frequencies. Fortunately we do not have to re-evaluate the transfer functions at negative frequencies (which is computationally expensive) — they can be computed from the real transfer functions by using a few simple relations that we derive next.

From Fourier transform properties we know that the Fourier transforms of real valued functions have complex conjugate symmetry, that is, if $f(t)$ is a real function with Fourier transform $f(i\omega)$ then $f^*(i\omega) = f(-i\omega)$. Applying this to the transfer function of Equation (C.1) we get

$$g^*_{cc}(i\omega) = g_{cc}(-i\omega)$$

$$g^*_{cs}(i\omega) = g_{cs}(-i\omega)$$

$$\vdots$$

Using these relations we find

$$g_{ou}(-i\omega) = \frac{1}{2}[g^*_{oc}(i\omega) - ig^*_{os}(i\omega)] \tag{C.6}$$

$$g_{yo}(-i\omega) = g^*_{co}(i\omega) + ig^*_{so}(i\omega) \tag{C.7}$$

$$g_{yu}(-i\omega) = \frac{1}{2}[(g^*_{cc}(i\omega) + g^*_{ss}(i\omega)) - i(g^*_{cs}(i\omega)) - g^*_{sc}(i\omega)]. \tag{C.8}$$

Equations (C.4), (C.5), and (C.6)–(C.8) are all we need to compute the complex transfer functions at all frequencies given the real transfer functions at positive frequencies.

Other interesting relations can be derived by applying the conjugate symmetry to the

other transfer functions in Equation (C.4). The following relations are easy to derive

$$g_{yu}(-i\omega) = g^*_{\dot{y}u}(i\omega)$$

$$g_{y\dot{u}}(-i\omega) = g^*_{yu}(i\omega).$$

C.2 Measurement of Real Transfer Functions

Various time and frequency domain methods exist for identifying multivariable systems; see for example [45]. A major consideration for measuring the compression system transfer functions was the quality of the measurements at low signal to noise ratios. Of all the available methods the nonparametric frequency domain correlation method is considered the most robust method for measuring transfer functions in noisy environments (see Rake [40] and Wellstead [47]). In addition, it is also robust against even ordered nonlinearities and methods exist to eliminate odd-ordered nonlinear effects [11]. It is interesting to note that this is one of the oldest identification methods and has been available in commercial transfer function analyzers since the Sixties [9]. We first present the method for a single-input single-output system and then we generalize it to the multivariable and closed loop cases.

Consider a single-input single-output system with transfer function $g(s)$ as shown in Figure C.1. If the input to the system is a cosine with constant amplitude u_0 and frequency ω_0 the output $y(t)$ of the system is

$$y(t) = |g(i\omega_0)| \cos(\omega_0 t + \varphi) u_0 + n(t) + \text{transients}$$

where $n(t)$ represents the noise in the measurement. If the system is stable the transients will go to zero and the system will reach steady state — we assume that this is the case.

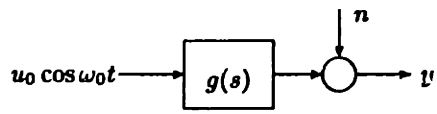

Figure C.1: Open loop transfer function measurement.

Multiplying the output by $\cos \omega_0 t$ and integrating over k periods $t_0 = 2\pi/\omega_0$ we get

$$\begin{aligned} p_r &= \frac{1}{kt_0} \int_0^{kt_0} y(t) \cos(\omega_0 t) \mathrm{d}t \\ &= |g(i\omega_0)| \cos(\varphi) u_0/2 + \frac{1}{kt_0} \int_0^{kt_0} n(t) \cos(\omega_0 t) \mathrm{d}t. \end{aligned} \tag{C.9}$$

If the noise is zero mean and independent from the input cosine or if the noise covariance is bounded by an exponential function (a weak assumption for stationary processes) the last integral goes to zero as k goes to infinity [45]. Similarly, forming the product between the output and $\sin \omega_0 t$ we get

$$\begin{aligned} p_i &= \frac{1}{kt_0} \int_0^{kt_0} y(t) \sin(\omega_0 t) \mathrm{d}t \\ &= |g(i\omega_0)| \sin(\varphi) u_0/2 + \frac{1}{kt_0} \int_0^{kt_0} n(t) \sin(\omega_0 t) \mathrm{d}t. \end{aligned} \tag{C.10}$$

From Equations (C.9) and (C.10) we can compute the magnitude and phase of the transfer function at ω_0 from

$$|g(i\omega_0)|^2 = (\frac{2}{u_0})^2 (p_r^2 + p_i^2) \tag{C.11}$$

$$\begin{aligned} \varphi &= \arg g(i\omega_0) \\ &= \arctan(p_i/p_r). \end{aligned} \tag{C.12}$$

There are various ways of viewing this procedure. One view is that of correlating out the known signal at the output of the system as shown in Figure C.2. An alternative view

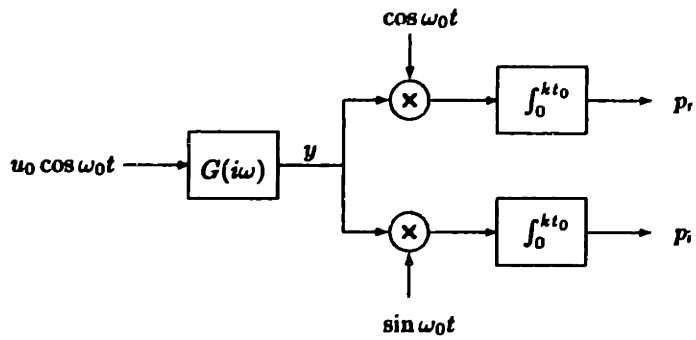

Figure C.2: Transfer function measurement: correlation.

is that of filtering the output $y(t)$ with two finite impulse response (FIR) filters [9] as shown in Figure C.3. The filter impulse responses and transfer functions are

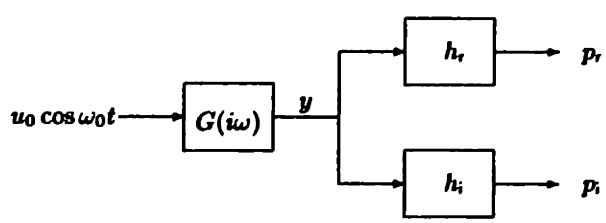

Figure C.3: Transfer function measurement: FIR filtering.

$$h_r(t) = \begin{cases} \frac{1}{kt_0}\cos(\omega_0 t) & 0 \le t \le t_0 \\ 0 & \text{otherwise} \end{cases} \quad \longleftrightarrow \quad h_r(i\omega) = \frac{-1}{\pi k}\frac{\omega}{\omega_0}\frac{\sin(\pi k\omega/\omega_0)}{1-(w/w_0)^2}e^{-i\pi k\omega/\omega_0}$$

$$h_i(t) = \begin{cases} \frac{-1}{kt_0}\sin(\omega_0 t) & 0 \le t \le t_0 \\ 0 & \text{otherwise} \end{cases} \quad \longleftrightarrow \quad h_i(i\omega) = \frac{-i}{\pi k}\frac{\sin(\pi k\omega/\omega_0)}{1-(w/w_0)^2}e^{-i\pi k\omega/\omega_0}.$$

The magnitudes of the transfer functions corresponding to the impulse responses are shown in Figure C.4 for two values of k. For the figures the magnitudes of the transfer functions have been multiplied by two to compensate for the factor two in Equation (C.11). Note further that the bandwidths are quite narrow so that only $\pm 10\%$ of the frequency axis about the normalized center frequency ω/ω_0 is shown. Only a few of the side lobes are shown and the dotted lines in the graphs indicate the envelopes of the side lobes. If we define the bandwidth $\Delta\omega/\omega_0$ of the filter as the width between the first zeros of the side lobes then $\Delta\omega/\omega_0 = 2/k$. Nondimensionalized frequencies in the range $0.1 \le \omega_0 \le 3.0$ rotor revolutions correspond to absolute frequencies in the range 4–120 Hz, so that for an integration time of 10 seconds, $40 \le k \le 1200$ and $0.05 \le \Delta\omega/\omega_0 \le 0.0017$. The standard deviation of the transfer function estimate $\widehat{G}$ is (see [40])

$$\text{STD}(\widehat{G}(i\omega_0)) = \frac{2}{u_0|G(i\omega_0)|}\sqrt{\frac{\text{PSD}_n(\omega_0)}{kt_0}} \tag{C.13}$$

where $\text{PSD}_n(\omega_0)$ is the value of the noise power density spectrum at ω_0.

The method can be generalized to the multi-input multi-output case in several ways. One way is to excite one input at a time and measure all the outputs, that is, we are measuring a single-input multi-output transfer function. By using linearity we can measure the complete transfer function by repeating the procedure for the other inputs one at a time. A significant amount of time can be saved by exciting an input with different frequencies (and appropriately selected phases) at the same time. Alternatively, we can excite the

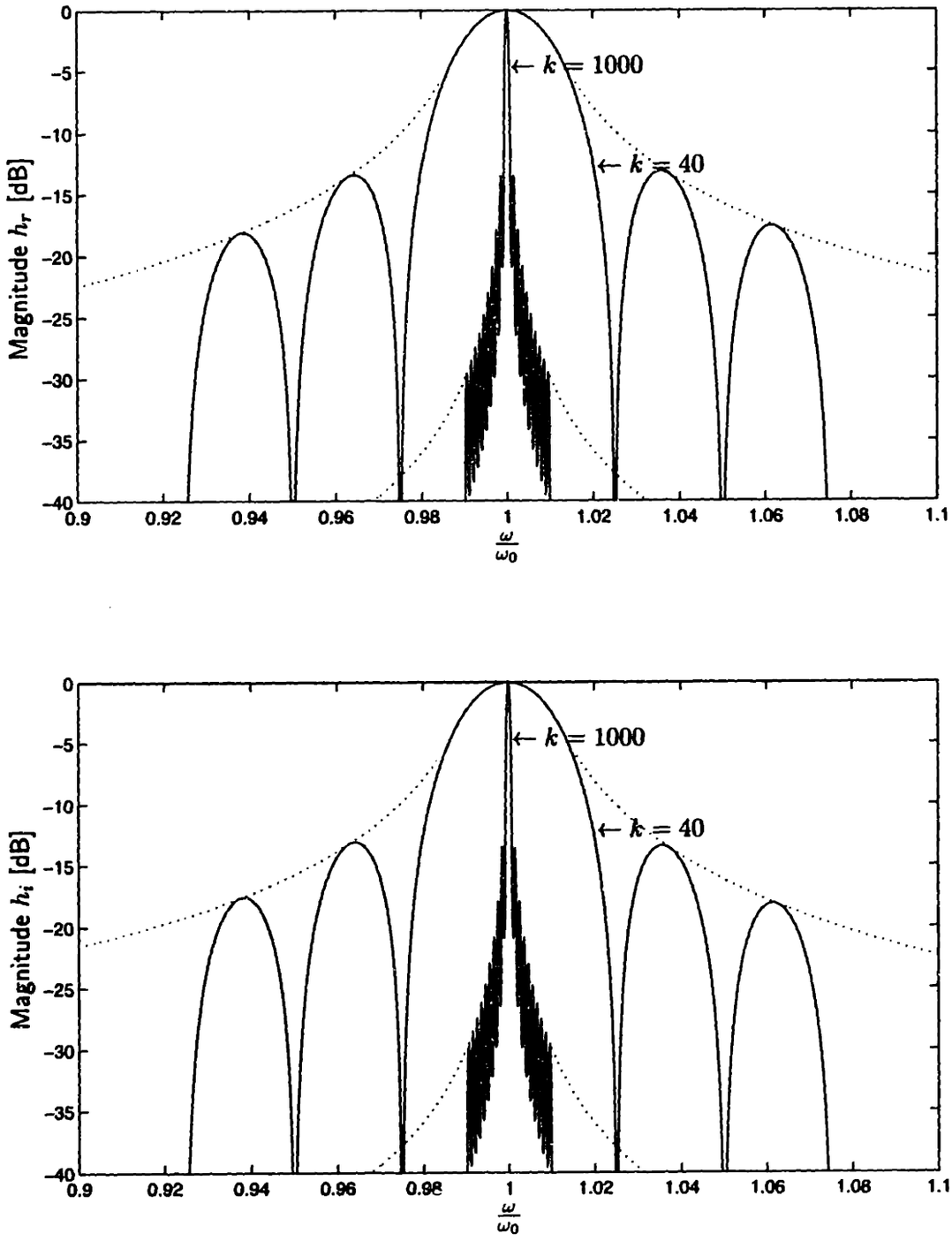

Figure C.4: FIR filter transfer functions. Top=h_r, bottom=h_i.

different inputs with different frequencies. Procedures exist for constructing these signals, called multisines, so as to minimize the maximum amplitude of the excitation signal, see [13]. A disadvantage of multisines is that the control power needed goes up with the square of the number of sines. For the current actuators it was found that with two or more frequencies at a time the AGV motor currents exceeded their maximum values and were electronically limited. This was considered undesirable as it causes distortion of the excitation signal so that only one frequency and one input was used at a time.

It is possible to generate the input signal so that the resulting wave travels in any direction. Although it is tempting to generate a wave rotating in the same direction as the rotor it was found that this would easily destabilize the system for excitation frequencies close to that of the first and second modes. Even if the compressor stayed stable the perturbations were too large to be considered linear operation so that corotating excitation signals were avoided during transfer function identification experiments.

The above method can also be extended to closed loop transfer function measurements provided that proper care is taken to prevent the method from giving biased results. The bias arises because, under closed loop operation, the noise is being fed back so that the noise at the input of the system is correlated with the noise at the output of the system. Unbiased measurements can be obtained if the system is excited with an external signal r that is uncorrelated with the noise as shown in Figure C.5. In this figure $K(s)$ represent the controller, $M(s)$ the motors and amplifiers, and $G(s)$ the compressor and anti-alias filters. We are interested in measuring $G(s)$. This is done by measuring the transfer functions from r to $\delta\gamma$ and r to $\delta\phi$ at the same time and recovering $G(s)$ from these two transfer functions.

The detailed closed loop system is shown in Figure C.6 where we indicated transfer function measurements to the velocity as well as to the plenum pressure perturbations. $A_p(s)$ and $A_\phi(s)$ are known anti-alias filters. First, assume the loop is not closed so that

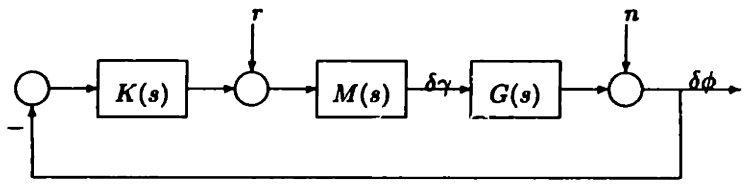

Figure C.5: Closed loop transfer function measurement.

the transfer function from r to the AGV deflections $\delta\gamma$ is

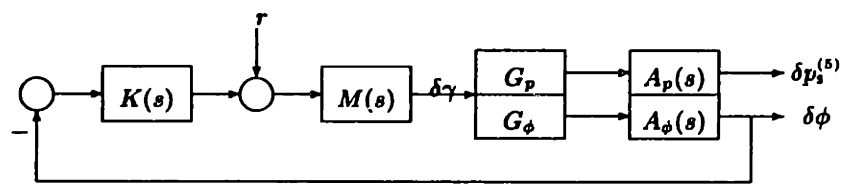

Figure C.6: Detail transfer function measurement.

$$\delta\gamma = Mr$$

$$\triangleq G_1 r. \tag{C.14}$$

The open loop transfer function from r to the velocity perturbations $\delta\phi$ is

$$\delta\phi = A_\phi G_\phi M r$$

$$= A_\phi G_\phi G_1 r \tag{C.15}$$

$$\triangleq G_2 r, \tag{C.16}$$

and the open loop transfer function to the plenum pressure perturbations is

$$p_s^{(5)} = A_p G_p M r$$

$$= A_p G_p G_1 r \tag{C.17}$$

$$\triangleq G_3 r. \tag{C.18}$$

From Equations (C.14)–(C.18) we get

$$G_\phi = A_\phi^{-1} G_2 G_1^{-1} \tag{C.19}$$

$$G_p = A_p^{-1} G_3 G_1^{-1}. \tag{C.20}$$

Under closed loop operation the transfer function from r to $\delta\gamma$ is

$$\delta\gamma = Mr - MKA_\phi G_\phi \delta\gamma$$

$$= (I + MKA_\phi G_\phi)^{-1} Mr$$

$$\triangleq G_1 r, \tag{C.21}$$

and the closed loop transfer function from r to $\delta\phi$ is

$$\delta\phi = A_\phi G_\phi \delta\gamma$$

$$= A_\phi G_\phi G_1 r \tag{C.22}$$

$$\triangleq G_2 r, \tag{C.23}$$

and the closed loop transfer function from r to $p_s^{(5)}$ is

$$p_s^{(5)} = A_p G_p \delta\gamma$$

$$= A_p G_p G_1 r \tag{C.24}$$

$$\triangleq G_3 r. \tag{C.25}$$

From Equations (C.21)–(C.25) we get

$$G_\phi = A_\phi^{-1} G_2 G_1^{-1} \tag{C.26}$$

$$G_p = A_p^{-1} G_3 G_1^{-1}. \tag{C.27}$$

We note that the transfer functions G_1, G_2, and G_3 defined in Equations (C.14)–(C.18) are different from the ones defined in Equations (C.21)–(C.25) respectively even though they have been defined with the same symbols — the former ones are open loop transfer functions while the latter ones are closed loop transfer functions. The form of the final expressions for G_ϕ and G_p are exactly the same for the open and closed loop cases so that the same program can be used to compute the required open loop transfer functions.

We note an interesting feature of this approach — it does not require the controller to be "square," that is, the number of inputs to the controller $\delta\phi$ does not have to equal the number of outputs from the controller $\delta\gamma$. However, we do require the transfer function from r to $\delta\gamma$ to be square. Measuring the transfer functions as outlined above has an additional advantage that we do not need to know the transfer functions of the individual building blocks, including the transfer function of the controller. Everything that is needed is included in the transfer function G_1 from r to $\delta\gamma$ that is measured. The transfer function G_1 can be measured accurately because the AGV deflections can be measured accurately with the shaft encoders. This method further does not require the motor-amplifier channels to be identical; even though matching was not required for the transfer function measurements the individual amplifiers were all adjusted so that their bandwidths matched to better than 3% as a mismatch between the channels will affect control.

In all the transfer function measurements the system was excited for 5 seconds before data collection was started to ensure that all transients died out and that the system has reached steady state. The integration time was set to 10 seconds for all frequencies and

excitation frequencies were always selected so that a full number of periods would fit into the integration time. The magnitude of the excitation signal was varied between 2° for frequencies close to those of the first and second modes, to 5° for frequencies far away from the first and second modes. This small level of excitation ensured linear operation of the AGVs and kept the amplifiers from saturating at frequencies up to about three times the rotor frequency. Furthermore, frequencies at one half, one, and two times the rotor frequencies were not used during transfer function measurements.

Appendix D System Identification

This appendix outlines a procedure to identify the state space matrices from a set of measured transfer functions.

For simplicity the presentation is given for single-input single-output (SISO) system, and extension to multi-input multi-output (MIMO) systems is briefly commented on. A brief description of parameterization is also given.

Let $g(s)$ be the measured transfer function. We would like to find a corresponding state space description. The procedure followed here is first to fit a transfer function of the form $b(s)/a(s)$ to the measured transfer function, and then find a state space description for it, keeping in mind that we are interested in the MIMO case.

Though we use $s = i\omega$ as frequency variable, the method is directly applicable to sampled data systems by replacing s with $z = e^{i\Omega}$.

D.1 SISO System Identification

We fit a model of the form $b(s)/a(s)$ to the measured transfer function $g(s)$ by minimizing the nonlinear least squares (NLS) criterion

$$c = \sum_{\omega} \left| \frac{b(s)}{a(s)} - g(s) \right|^2 . \tag{D.1}$$

Levy's method (see [48]) is often used to turn the NLS problem into a linear least squares problem with cost function

$$c' = \sum_{\omega} |b(s) - a(s)g(s)|^2 \tag{D.2}$$

that is easy to solve. This method often gives poor results as we are ignoring a factor $1/a(s)$ in the last equation; the correct expression for the cost function is

$$\sum_{\omega} \left| \frac{1}{a(s)} [b(s) - a(s)g(s)] \right|^2 . \tag{D.3}$$

Levy's method can be improved by iterating the procedure as follows. We start the procedure by assuming an initial estimate $a_0(s) = 1$ and solving the linear problem Equation (D.3) to obtain the first iterates $a_1(s)$ and $b_1(s)$. The new $a_1(s)$ is then used to solve for $a_2(s)$ and $b_2(s)$ in

$$\sum_{\omega} \left| \frac{1}{a_1(s)} [b_2(s) - a_2(s)g(s)] \right|^2 . \tag{D.4}$$

etc. This method, due to Sanathanan and Koerner, is often called the SK-iteration. The SK-iteration is not guaranteed to converge. Whitfield [48] has shown that even if it converges, it converges to values that are not the true minimum of the NLS problem. However, the SK-iteration is useful to obtain an initial estimate for the minimization of Equation (D.1).

A positive frequency weighting functions $w(s)$ can be included in the cost function to emphasize certain frequency ranges. In addition, it is useful to allow for known dynamics $g_k(s)$ in the measured transfer function. Known dynamics include sensor and actuator dynamics, computational delays, and estimates of poles and zeros determined from Bode plots. The final cost function thus has the form

$$c = \sum_{\omega} w(s) \left| g_k(s) \frac{b(s)}{a(s)} - g(s) \right|^2 . \tag{D.5}$$

Instead of using this cost function, a criterion due to Sidman [44] can be used. Sidman

suggests fitting the log of the transfer function

$$c_{\text{lg}} = \sum_{\omega} \left| \log \frac{b(s)}{a(s)} - \log g(s) \right|^2$$

$$= \sum_{\omega} \left| \log \frac{\left|\frac{b(s)}{a(s)}\right|}{|g(s)|} + i \left[\arg(\frac{b(s)}{a(s)}) - \arg(g(s)) \right] \right|^2 \tag{D.6}$$

that is, we are minimizing a cost function consisting of the sum of the ratio of the magnitudes and phase difference of the transfer functions. Pintelon [39] has shown that this is a consistent estimator, that it is not sensitive to plant model errors, (that is, the plant does not belong to the model set), and that it is robust to outliers in the measurements.

The log-criterion c_{lg} is not without problems. The phase is in the range $[-\pi, \pi]$ and thus "wraps around," resulting in discontinuities that complicates the optimization step. A way around this is to unwrap the phase, but this, too, has its own complications. This cost function can be extended to include frequency weighting and known dynamics as before. In addition, one can also include relative weighting between the magnitude and phase.

D.2 Parameterization

If the structure of the system is known, e.g. simple real poles/zeros, complex poles/zeros, delay elements, etc., the polynomials can be written in factored form. For example, we can parameterize the numerator polynomial as

$$b(s) = \sum_{j=0}^{n} b_j s^j \tag{D.7}$$

$$= \prod_j (s + z_j) \prod_k (s^2 + 2\zeta_k \omega_k s + \omega_k^2). \tag{D.8}$$

The factored form has better numerical properties than the polynomial form [39]. However, if the structure is not know it is better to use the polynomial representation because it is

general.

Numerical problems arise because the standard polynomials $s^1, s^2, s^3, \ldots, s^n$ become self-similar, see Adcock [1]. An example of the self-similarity of the standard polynomials is shown in Figure D.1 for orders of practical interest. The higher degree polynomials have very similar shapes. To improve the numerical properties of the standard polynomials the frequency range is usually scaled to the range [0,1], as was done in Figure D.1. The self-similarity problem can be solved by using orthogonal Chebychev polynomials instead of the standard polynomials. In Figure D.2 we show the corresponding Chebychev polynomials. The SK-iteration typically converged 2-6 times faster for the same problems when orthogonal polynomials were used instead of the standard polynomials. For discrete time systems it is not necessary to use Chebychev polynomials as the complex exponentials are orthogonal on the unit circle.

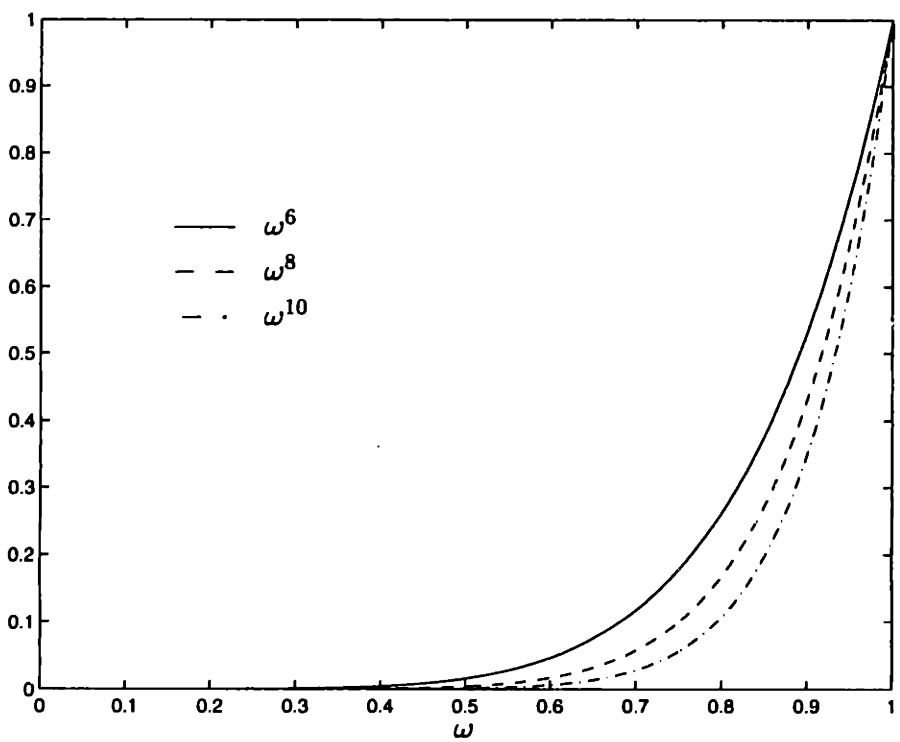

Figure D.1: Self-similarity of standard polynomials.

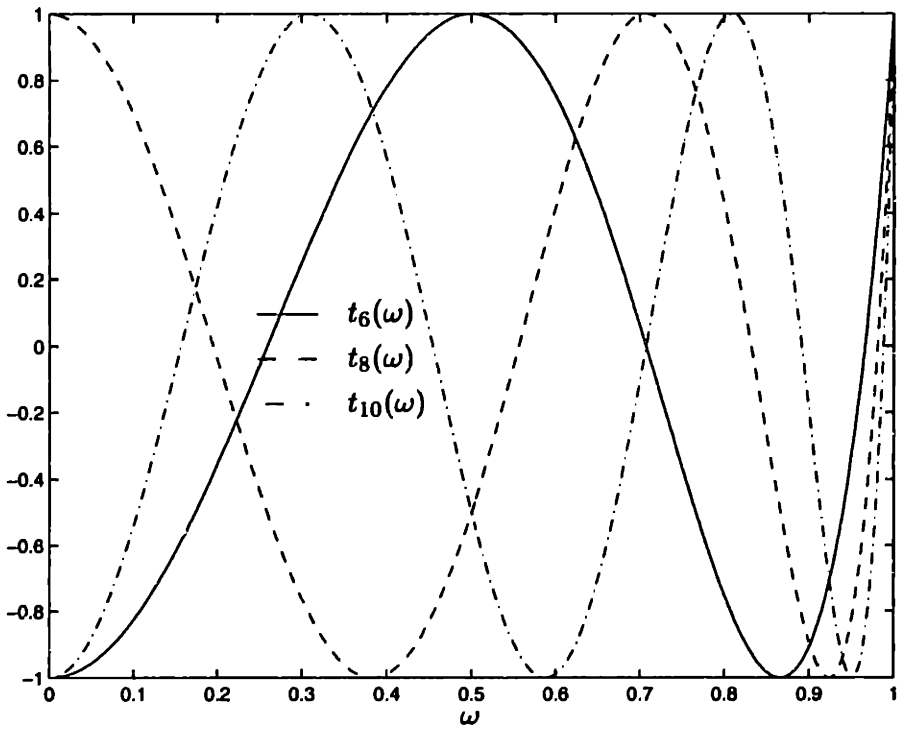

Figure D.2: Chebychev polynomials.

Once we have the numerator and denominator polynomials we must find a state space representation. This is done by computing the Markov parameters (or impulse response) from the identified numerator and denominator coefficients, constructing Hankel matrices, and using the singular value decomposition to find a minimal balanced realization. This is a well known procedure and is discussed in detail by Chen [4]. This step only works if the system is stable. For unstable systems the impulse response diverges and causes numerical problems. The procedure developed by Jacques [23] was found to work well for unstable systems, even though it is only guaranteed to work for stable systems.

D.3 MIMO System Identification

The MIMO case follows the same procedure as outlined above. All we need is find a parameterization for the MIMO transfer function. There are many ways to do this, see Chen [4]. The approach followed here is simply a direct extension of the SISO description, that is

$$G(s) = \frac{B(s)}{a(s)} \tag{D.9}$$

where $B(s)$ is a matrix of polynomials. Like the SISO case, the polynomials can also be written in factored form if desired. The Markov parameters and state space matrices are computed as before.

System identification is typically done in several iterations. A typical iteration is as follows.

1. Select a parameterization and solve the nonlinear minimization Equation (D.5) or D.6. This step can be repeated with different orders for the numerator and denominator polynomials. Poles and zeros obtained from earlier iterations may be fixed (by including them in g_k), thereby reducing the dimension of the minimization problem.

2. Compute the state space description as discussed at the end of Appendix D.2.

3. Compare transfer functions computed from the state space description with the measured transfer functions. Model reductions can be applied in this step if the dimension of the state vector is too high, else, repeat step 1 with lower orders for the polynomials.

Appendix E Parameter Identification

The parameters in the extended model can be grouped into four sets

Geometric parameters	μ_r, μ_s, μ_a, μ_i, l_1, l_4, b_G, x_m,
Pressure rise characteristic	ψ, ψ_i, $\frac{\partial \psi}{\partial \phi}$, $\frac{\partial \psi}{\partial \gamma}$,
Total pressure loss parameters	r, τ_f, $\frac{\partial l_r}{\partial \phi}$, $\frac{\partial l_s}{\partial \phi}$,
Steady state operating point	ϕ_s, l_{rs}, l_{ss}, k_t, distortion.

The axial measurement location x_m has been included in the list of geometric parameters although it is, strictly speaking, not part of the model but part of the measurement relation. However, the sensor location has a strong influence on the magnitudes of the harmonics, and therefore on the magnitudes of the transfer functions, so that it has been included here.

In Chapter 4 we have seen that the dynamics are captured well by the extended model but there were small differences in transfer function magnitudes, and pole and zero frequencies. Some parameters used in the model are first order approximations or based on prior experimental results. For example, the rotor and stator fluid inertias μ_r and μ_s take into account only fluid that are in the rotors and stators respectively, while it is reasonable to assume that at least some fluid in the gaps between the rotors and stators will also be accelerated and needs to be included in these inertias. The proportionality constant τ_f used in the total pressure loss model was determined by Haynes [20] by fitting the individual harmonic transfer functions to experimental data.

The parameters that we would like to determine are μ_r, μ_s, μ_a, x_m, r, τ_f, $\frac{\partial\psi}{\partial\phi}$, $\frac{\partial\psi}{\partial\gamma}$, k_t. The actuator fluid inertia μ_a and slope $\frac{\partial\psi}{\partial\gamma}$ have a strong influence on the dominant zero. In modelling the unsteady viscous effects it was assumed that the losses divide between the rotors and stators in proportion to the reaction r. The time constants associated with the loss dynamics were assumed to equal the corresponding flow-through times multiplied by the proportionality constant τ_f, see Equations (3.61) and (3.62). By estimating these two parameters we can verify our assumptions. Even though the slope $\frac{\partial\psi}{\partial\phi}$ is available from the characteristic, it was found that it is better to estimate it as well. The poles are very sensitive to the slope and small errors in it leads to biased results for the other parameters. The throttle constant k_t is not known and must also be estimated. Initially, the parameter b_G was also estimated and was found to agree with the geometrical value so it is not estimated. We will denote the list of parameters to be estimated by the vector

$$\boldsymbol{\xi} = [\mu_r, \mu_s, \mu_a, x_m, r, \tau_f, \frac{\partial\psi}{\partial\phi}, \frac{\partial\psi}{\partial\gamma}, k_t]^T. \tag{E.1}$$

Instead of using steady state measurements to identify the required parameters, we will determine them directly from the transfer functions. In Appendix C.1 we saw that the transfer functions can be measured with high accuracy and thus we believe that the approach proposed here will result in better estimates of the parameters.

The linearized model depends on the steady state flow $\phi_s^{(3)}(\theta)$ which we do not have, so all the quantities, e.g., the slope $\frac{\partial\psi}{\partial\phi}$ and steady state losses l_{rs} and l_{ss}, are unknown. If we restrict ourselves to the uniform flow case these quantities are known or can be computed for the specific operating point, so we will use the uniform flow transfer functions to do the parameter identification.

The same set of parameters must fit all the individual transfer functions, not just one, so instead of using the transfer function of an individual harmonic to identify the parameters,

we will use all the transfer functions simultaneously. Using all the transfer functions provide us with more independent data points and thus the standard deviations of the estimates are reduced.

A standard least squares procedure is used. The cost function c to be minimized is

$$c = \sum_{n=0}^{3} \sum_{i} \omega \left(\widehat{g}_{nn}(i\omega; \boldsymbol{\xi}) - g_{nn}(i\omega) \right)^2 \tag{E.2}$$

where $\widehat{g}_{nn}(i\omega; \boldsymbol{\xi})$ is the transfer function form $\delta\widetilde{\gamma}_n$ to $\delta\widetilde{\phi}_n$ and depends on the parameter vector $\boldsymbol{\xi}$, and $g_{nn}(i\omega)$ is the measured transfer function. Because we are using the uniform flow transfer functions only the diagonal elements of the transfer function matrix are used, the others are zero. The transfer functions $\widehat{g}_{nn}(i\omega; \boldsymbol{\xi})$ is highly nonlinear in the argument $\boldsymbol{\xi}$ and a good initial estimate is necessary to ensure successful minimization of the cost function. The nominal geometric and steady state values were found to be suitable for this purpose.

The nominal and identified parameters are listed in the table below. In this table the first row shows the elements of the initial estimate $\boldsymbol{\xi}_0$ and the second row the identified elements $\boldsymbol{\xi}$.

	μ_r	μ_s	μ_a	x_m	r	τ_f	$\frac{\partial\psi}{\partial\phi}$	$\frac{\partial\psi}{\partial\gamma}$	k_t
$\boldsymbol{\xi}_0$	0.68	0.33	0.29	−0.60	0.75	1.50	−0.04	−0.26	8.00
$\boldsymbol{\xi}$	0.58	0.68	0.15	−0.47	0.76	1.53	−0.12	−0.16	6.25

Figure E.1 shows the experimentally measured $g_{nn}(i\omega)$, nominal $g_{nn}(i\omega; \boldsymbol{\xi}_0)$, and identified $\widehat{g}_{nn}(i\omega; \boldsymbol{\xi})$ transfer functions. All the magnitudes of the nominal transfer functions (dashed lines) are larger than the measured magnitudes (dots), and the peaks (poles) of the nominal transfer function magnitudes are at slightly higher frequencies. Both these differ-

ences are absent in the identified transfer functions (solid lines) and the identified transfer functions clearly have a better fit.

The estimated rotor fluid inertia μ_r is 15% smaller than the geometrical value while the estimated stator fluid inertia μ_s is almost twice as large as the geometrical value. This suggests that the fluid in the gaps should be lumped with those in the stators. If the lengths of the gaps between the rotors and stators and between consecutive stages are added to that of the stators, we get an effective stator fluid inertia equal to 0.676. This agrees very well with the identified value 0.68.

Longley [25] used the basic steady state model (no losses) to compute μ_r and find it should be approximately twice the geometrical value. Hynes modelled losses by modifying the effective rotor fluid inertia. All these are based on *steady state* measurements. The transfer functions are a direct measurement of the dynamic behavior, the parameters of which we are trying to identify, so the estimates obtained from the transfer functions are superior.

The actuator fluid inertia μ_a is smaller than the geometrical value. A possible explanation may be the low solidity of the AGVs.

The estimated measurement location x_m is smaller than the geometrical value and puts the source of the perturbations towards the end of the first stage. This agrees with measurements by Haynes [20] who found that the different harmonics were strongest in the first stage. The geometrical value was obtained by measuring the distance between the inlet of the first rotor and the sensors.

The reaction r and constant of proportionality τ_f used in the model of the unsteady viscous effects agree well with the nominal values. Haynes [20] estimated τ_f on the same compressor and his estimate was used as the nominal value.

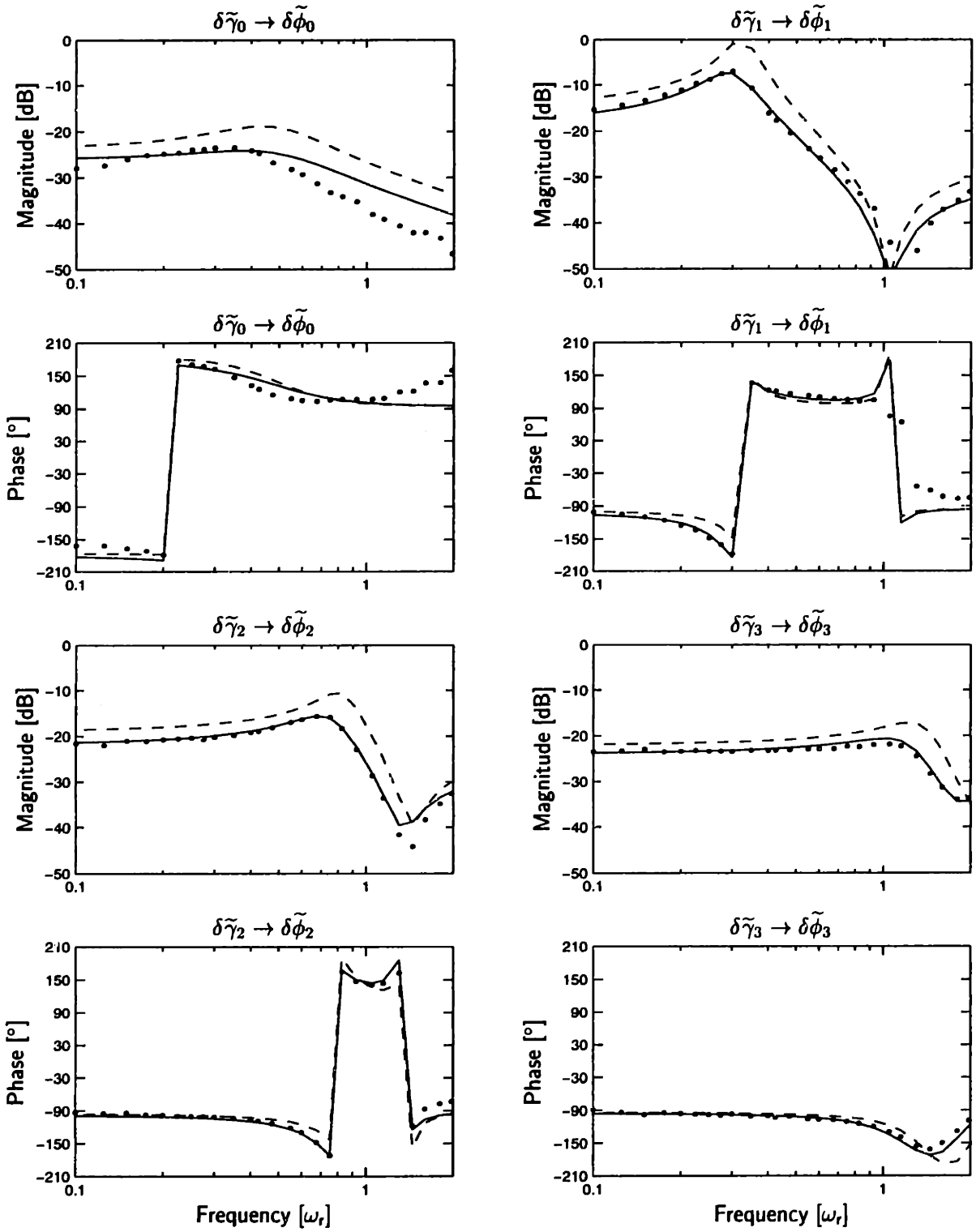

Figure E.1: Transfer functions $\phi = 0.470$, uniform flow. The horizontal axes are frequency in ω_r. Solid line=transfer function using identified parameters $\widehat{g}_{nn}(\xi)$, dashed line=nominal transfer function $g_{nn}(\xi_0)$, dots=measured transfer function.

The estimated slope $\frac{\partial \psi}{\partial \phi} = -0.12$ corresponds to $\phi = 0.473$ on the constant speed line (nominal $\phi = 0.470$) and is within measurement error. The smaller value of $\frac{\partial \psi}{\partial \gamma}$ indicates that the actuators are less effective than the model predicts and may be a result of the simplified modelling of the AGVs. In the derivation of AGV relations we have assumed a continuum of blades while there are only 12 around the annulus.

We could follow this parameter identification step with a second step during which we use the geometric parameters that we have just identified and estimate the pressure rise characteristic $\psi(\phi)$ over the full range of the distorted flow $\phi(\theta)$. However, to do so we need $\phi_s^{(3)}(\theta)$, the steady flow through the compressor, but we only have the upstream measurement $\phi_s^{(2)}(\theta)$. One solution is to identify $\phi_s^{(3)}(\theta)$ as well. Estimating both $\psi(\phi)$ and $\phi_s^{(3)}(\theta)$ led to divergence of the least squares minimization step. This is probably because all the steady state and pressure rise parameters are now free variables and the optimization problem may not be well posed any more. Therefore, determination of the characteristic over the full range of the nonuniform flow is still an open problem.

References

[1] J.L. Adcock. Curve Fitter for Pole-Zero Analysis. *Hewlett-Packard Journal*, pages 55–69, January 1987.

[2] F. Aulehla and D.M. Schmitz. New Trends in Intake/Engine Compatibility Assessment. In *AGARD-CP-400: Engine Response to Distorted Inflow Conditions*, March 1987.

[3] E.P. Bruce. Design and Evaluation of Screens to Produce Multi-cycle ±20% Amplitude Sinusoidal Velocity Profiles. In *AIAA 8th Aerodynamic Testing Conference, Paper No. 74-623*, pages 1–11, July 1974.

[4] C-T. Chen. *Linear System Theory and Design.* Holt, Rinehart and Winston, Inc., 1984.

[5] R. Chue, T.P. Hynes, E.M. Greitzer, C.S. Tan, and J.P. Longley. Calculation of Inlet Distortion Induced Compressor Flow Field Instability. *International Journal of Heat and Fluid Flow*, 10(3):211–233, September 1986.

[6] I.J. Day. Active Suppression of Rotating Stall and Surge in Axial Flow Compressors. *ASME J. of Turbomachinary*, 115:40–47, January 1993.

[7] I.J. Day. Stall Inception in Axial Flow Compressors. *ASME J. of Turbomachinary*, 115:1–9, January 1993.

[8] I.J. Day and C. Freeman. The Unstable Behavior of Low and High-Speed Compressors. *ASME J. of Turbomachinary*, 116:194–201, April 1993.

[9] C.S. Elsden and A.J. Ley. A Digital Transfer Function Analyser Based on Pulse Rate Techniques. *Automatica*, 5:51–60, 1969.

[10] A.H. Epstein, J.E. Williams, and E.M. Greitzer. Active Suppression of Aerodynamics Instabilities in Turbomachines. *J. of Propulsion*, 5(2):204–211, March-April 1989.

[11] D.C. Evans, D. Rees, and D.L. Jones. Identifying Linear Models of Systems Suffering Nonlinear Distortions, with Gas Turbine Application. *IEE Proceedings on Control Theory Applications*, 142(3):229–240, May 1995.

[12] V.H. Garnier, A.H. Epstein, and E.M. Greitzer. Rotating Waves as a Stall Inception Indication in Axial Compressors. *ASME J. of Turbomachinary*, 113:290–302, April 1991.

[13] K. Godfrey, editor. *Perturbation Signals for System Identification.* Prentice-Hall, Inc., 1993.

[14] R.J. Goldstein. Thermal Anemometers. In R.J. Goldstein, editor, *Fluid Mechanic Measurements.* Hemisphere Publishing Corporation, 1983.

[15] Y. Gong, August 1995. Private communication.

[16] E.M. Greitzer. Review — Axial Compressor Stall Phenomena. *ASME J. of Fluids Engineering*, 102:134–151, June 1980.

[17] E.M. Greitzer. The Stability of Pumping Systems — the 1980 Freeman Scholar Lecture. *ASME J. of Fluids Engineering*, 103:193–243, 1981.

[18] E.M. Greitzer, A.H. Epstein, et al. Dynamic Control of Aerodynamic Instabilities in Gas Turbine Engines. *AGARD-LS-183*, pages 8–1–8–21, May 1992.

[19] D.L. Gysling. *Dynamic Control of Rotating Stall in Axial Flow Compressors Using Aeromechanical Feedback.* PhD thesis, Department of Aeronautics and Astronautics, MIT, 1993.

[20] J.M. Haynes. Active Control of Rotating Stall in a Three-Stage Axial Compressor. Master's thesis, Department of Aeronautics and Astronautics, MIT, 1993.

[21] J.M. Haynes, G.J. Hendricks, and A.H. Epstein. Active Stabilization of Rotating Stall in a Three-Stage Axial Compressor. *ASME J. of Turbomachinary*, 116:226–239, 1994.

[22] T.P. Hynes and E.M. Greitzer. A method for assessing Effects of Circumferential Flow Distortion on Compressor Stability. *ASME J. of Turbomachinary*, 109:371–379, July 1987.

[23] R.N. Jacques. *On-line System Identification and Control Design for Flexible Structures.* PhD thesis, Department of Aeronautics and Astronautics, MIT, 1994.

[24] J.-K. Koo and D.F. James. Fluid Flow Around and Through a Screen. *J. Fluid Mechanics*, 60, part 3:513–538, 1973.

[25] J.P. Longley. *Inlet Distortion and Compressor Stability.* PhD thesis, Trinity College, Cambridge University, 1988.

[26] J.P. Longley. Unsteady Nonuniform IGV Stagger. Unpublished Notes, November 1988.

[27] J.P. Longley, 1992. Private communication.

[28] J.P. Longley. A Review of Nonsteady Flow Models for Compressor Stability. *ASME J. of Turbomachinary*, pages 202–215, April 1994.

[29] J.P. Longley and E.M. Greitzer. Inlet Distortion Effects in Aircraft Propulsion System Integration. *AGARD-LS-183*, pages 6-1–6-18, May 1992.

[30] J.M. Maciejowski. *Multivariable Feedback Systems.* Addison-Wesley Publishing Company, 1989.

[31] C. Mansoux. Distributed Nonlinear Stability Analysis of Rotating Stall. Master's thesis, Department of Aeronautics and Astronautics, MIT, May 1994.

[32] R.S. Mazzawy. Multiple Segment Parallel Compressor Model for Circumferential Flow Distortion. *ASME J. of Engineering for Power*, 99:288–296, April 1977.

[33] N.M. McDougall, N.A. Cumpsty, and T.P. Hynes. Stall Inception in Axial Compressors. *ASME J. of Turbomachinary*, 112:116–125, January 1990.

[34] F.K. Moore and E.M. Greitzer. A Theory of Post-Stall Transients in Axial Compressors: Part I — Development of the Equations. *ASME J. of Engineering for Gas Turbines and Power*, 108:68–76, 1986.

[35] S. Nagano, Y. Machida, and H. Takata. Dynamic Performance of Stalled Blade Rows. *Japan Society of Mechanical Engineers*, 1971. Presented at the Tokyo Joint International Gas Turbine Conference, Tokyo, Japan.

[36] A.V. Oppenheim and R.W. Schafer. *Digital Signal Processing.* Prentice-Hall, Inc., 1975.

[37] J.D. Paduano. *Active Control of Rotating Stall in Axial Compressors.* PhD thesis, Department of Aeronautics and Astronautics, MIT, February 1992.

[38] J.D. Paduano et al. Active Control of Rotating Stall in a Low-Speed Axial Compressors. *ASME J. of Turbomachinary*, 115:48–56, January 1993.

[39] R. Pintelon, P. Guillaume, Y. Rolain, J. Schoukens, and H. Van Hamme. Parametric Identification of Transfer Functions in the Frequency Domain — A Survey. *IEEE Transactions on Automatic Control*, 39(11):2245–2260, November 1994.

[40] H. Rake. Step Response and Frequency Response Methods. *Automatica*, 16:519–526, 1980.

[41] C. Reid. The Response of Axial Flow Compressors to Intake Flow Distortion. *ASME paper 69-GT-29*, 1969.

[42] SAE-16 Committee. Gas Turbine Engine Inlet Distortion Guidelines, 1978. Aerospace Recommended Practice 1420.

[43] A. Schulmeyer. Enhanced Compressor Distortion Tolerance using Asymmetric Inlet Guide Vane Stagger. Master's thesis, Department of Aeronautics and Astronautics, MIT, 1989.

[44] M.D. Sidman, F.E. DeAngelis, and G.C. Verghese. Parametric System Identification on Logarithmic Frequency Response Data. *IEEE Transactions on Automatic Control*, 36(9):1065–1070, September 1991.

[45] T. Söderstrom and P. Stoica. *System Identification*. Prentice Hall International Ltd., 1989.

[46] M. Tryfonidis, O. Etchevers, J. D. Paduano, A.E. Epstein, and G. J. Hendricks. Pre-Stall Behavior of Several High-Speed Compressors. In *ASME Gas Turbine and Aeroengine Congress and Exposition, The Hague, The Netherlands*, June 1994.

[47] P.E. Wellstead. Non-Parametric Methods of System Identification. *Automatica*, 17:55–69, 1981.

[48] A.H. Whitfield. Asymptotic Behavior of Transfer Function Synthesis Methods. *International Journal of Control*, 45(3):1083–1092, 1987.

[49] D.D. Williams. Engine Compatibility. Technical report, Rolls-Royce PLC, May 1991.

[50] D.D. Williams and L.E. Surber. Intake/Engine Compatibility. In J. Seddon and E.L. Goldsmith, editors, *Practical Intake Aerodynamic Design*, pages 21–71. Blackwell Scientific Publications, 1993.